

See discussions, stats, and author profiles for this publication at:  
<https://www.researchgate.net/publication/251450121>

# Engineering Quantum Confined Silicon Nanostructures: Ab-Initio Study of the Structural, Electronic and Optical Properties

ARTICLE *in* ADVANCES IN QUANTUM CHEMISTRY · DECEMBER 2009

Impact Factor: 1.19 · DOI: 10.1016/S0065-3276(09)00710-2

---

CITATIONS

7

READS

21

## 2 AUTHORS:



Elena Degoli

Università degli Studi di Moden...

63 PUBLICATIONS 1,294 CITATIONS

SEE PROFILE



Stefano Ossicini

Università degli Studi di Moden...

212 PUBLICATIONS 4,386 CITATIONS

SEE PROFILE

# CHAPTER 6

## Engineering Quantum Confined Silicon Nanostructures: Ab-Initio Study of the Structural, Electronic and Optical Properties

Elena Degoli<sup>a</sup> and Stefano Ossicini<sup>a</sup>

---

Contents		
1.	Introduction	203
2.	Theoretical Methods	207
2.1.	The density functional theory	208
2.2.	The Many-Body perturbation theory	212
3.	Zero-dimensional Systems	216
3.1.	Free-standing silicon nanocrystals	216
3.2.	Silicon nanocrystals embedded in a SiO <sub>2</sub> matrix	232
3.3.	Doped silicon nanocrystals	235
4.	One-dimensional Systems	248
4.1.	Silicon and germanium nanowires	248
4.2.	Doped silicon nanowires	253
5.	Two-dimensional Systems	256
5.1.	Si and Ge nanofilms	256
5.2.	Si/CaF <sub>2</sub> multi-quantum-wells	260
5.3.	Si/SiO <sub>2</sub> superlattices	267
6.	Conclusions	271
	Acknowledgments	274
	References	274

---

### 1. INTRODUCTION

Understanding and controlling the properties of materials is crucial for improving the information technology on which our modern world is built.

<sup>a</sup> CNR-INFM-S<sup>3</sup> and Dipartimento di Scienze e Metodi dell'Ingegneria - Università di Modena e Reggio Emilia - via Amendola 2 Pad. Morselli, I-42100 Reggio Emilia, Italy

The ever increasing demands from distributed information systems are stimulating research and technology development. Theory has a central role because a microscopic understanding represents a fundamental step towards the innovation, design and fabrication of new materials and devices. The ability to describe structural, electronic and optical properties of new materials with accurate first-principle methods is hence of fundamental importance.

In particular silicon microelectronics devices have revolutionized our lives in the second half of the last century. Integration and economy of scale are the two key ingredients for the Si technological success. Si has a band gap of 1.12 eV, which is ideal for room temperature operation, and has an oxide that allows the processing flexibility to place, at this time, more than  $10^8$  transistors on a single chip. The extreme integration levels reached by the Si microelectronics industry have permitted high speed performance and unprecedented interconnection levels. The present interconnection degree is sufficient to cause interconnect propagation delays, overheating and information latency between single devices. To overcome this bottleneck, photonic materials, in which light can be generated, guided, modulated, amplified and detected, need to be integrated with standard electronic circuits to combine the information processing capabilities of electronic data transfer and the speed of light. In particular, chip to chip or even intra-chip optical communications all require the development of efficient optical functions and their integration with state-of-art electronic functions [1].

Si is the desired material, because Si-based optoelectronics would open the door to faster data transfer and higher integration densities at low cost. Si microphotonics has boomed during recent years. Almost all the various photonic devices have been demonstrated [1,2], but the main limitation of Si photonics remains the lack of any practical Si-based light source. Bulk Si is an indirect band-gap material which emits in the infrared region; radiative lifetimes of excited carriers in Si are very long, causing a predominant de-excitation of carriers via fast non-radiative recombinations. Moreover, Si has significant free carrier absorption and Auger recombination rates which impede population inversion and, hence, optical gain if strongly pumped. Therefore the role of Si as a light source has been ignored up to now.

Several attempts have been employed to engineer luminescing transitions in an otherwise indirect material [1]. After the initial impulse given by the pioneering work of Canham on photoluminescence (PL) from porous Si [3], nanostructured silicon has received extensive attention (for reviews see Refs. [4–15]). This activity is mainly centered on the possibility of getting relevant optoelectronic properties from nanocrystalline Si. The huge efforts made towards matter manipulation at the nanometer scale have been motivated by the fact that desirable properties can be generated just by changing the system dimension and shape. The idea is to confine carriers into small Si-based systems (1–5 nm in size) so that quantum confinement

effects start to play a crucial role by changing the physical properties of bulk Si [1,10].

Quantum confinement can act in three spatial directions, thus one has zero-dimensional, one-dimensional, and two-dimensional confined systems.

For zero-dimensional systems, as in the case of Si nanocrystals (Si-NCs) the band-gap increases with decreasing size. Visible luminescence external efficiency in excess of 23% has been obtained in nanostructured Si [1,10,16].

Investigation of phenomena such as the Stokes shift (difference between absorption and emission energies), the PL emission energy vs nanocrystals size, etc. can give a fundamental contribution to the understanding of how the optical response of such systems can be tuned. An interesting amount of work has been done regarding excited Si-NCs [4–15], but a clear comprehension of some aspects is still lacking. The question of surface effects, in particular oxidation, has been addressed in recent years. Both theoretical calculations and experimental observations have been applied to investigate the possible active role of the interface on the optoelectronic properties of Si-NCs. Different models have been proposed: Baierle et al. [17] have considered the role of the surface geometry distortion of small hydrogenated Si clusters in the excited state. Wolkin et al. [18] have observed that oxidation introduces defects in the Si-NC band-gap which pin the transition energy. They claimed the formation of a Si=O double bond as the pinning state. The same conclusion has been recently reached by other authors [19–22], whereas Vasiliev et al. [23] have pointed out that similar results can also be obtained for O connecting two Si atoms (single bonds) at the Si-NC surface.

The optical gain observed in Si-NC embedded in SiO<sub>2</sub> formed by different techniques [24–27] has given a further impulse to these studies. Interface radiative states have been suggested to play a key role in the mechanism of population inversion at the origin of the gain [24,25,28]. However many researchers are still convinced of the pure quantum confinement model and they are focusing their efforts mainly on the self trapped excitonic effects [29,30] in order to explain the differences between their results and the experimental outcomes.

Nevertheless Si-NC remain indirect band-gap materials where structures related to momentum-conserving phonons were clearly observed [1,8,31]. This drawback can be circumvented by introducing into the Si-NCs an isoelectronic impurity [1,10] or by simultaneous *n*- and *p*-type impurity doping [32]. In a series of intriguing papers Fujii and collaborators [32–34] have demonstrated that it is possible to control the PL properties of Si-NCs by simultaneous doping with B and P impurities. They have shown not only that the PL intensity of co-doped Si-NCs is always higher than that of either P- or B doped Si-NCs, but that it is even higher than that of the undoped Si-NCs. In addition, under resonant excitation conditions the co-doped samples did not exhibit structures related to momentum-conserving

phonons, suggesting that in this case the quasidirect optical transitions are predominant.

Among the different Si nanostructures, Si nanowires (Si-NWs) have recently attracted a lot of interest. Being one-dimensional structures, they seem potentially as useful as carbon nanotubes and probably more, due to the possibility of tailoring their chemistry and using them to create nanosized lasers. Si-NWs of different controllable sizes and growth directions have been synthesized in recent years through several routes [1,35–39]. Thin Si-NWs down to about 1 nm diameter have been obtained with grown orientation along the [100], [110], [111] and [112] directions and with a very rich surface chemistry. The clear device potential of these Si-NWs has been demonstrated by a wide range of applications [40–43].

Regarding the two-dimensional systems, the optoelectronic properties of Si nanoslabs embedded in calcium fluoride and in silicon dioxide have been experimentally studied [44–52], confirming the role of quantum confinement, even if the discussion is still alive.

In this paper we present a comprehensive first-principles study of the structural, electronic and optical properties of undoped and doped Si nanosystems. The aim is to investigate, in a systematic way, their structural, electronic and stability properties as a function of dimensionality and size, as well as pointing out the main changes induced by the nanostructure excitation. A comparison between the results obtained using different Density Functional Theory based methods will be presented. We will report results concerning two-dimensional, one-dimensional and zero-dimensional systems. In particular the absorption and emission spectra and the effects induced by the creation of an electron–hole pair are calculated and discussed in detail, including many-body effects.

The paper is organized as follows. A complete description of the theoretical methods used is given in Section 2 considering, in the different subsections, the Density Functional Theory (DFT) (Section 2.1), the  $\Delta$  self-consistent ( $\Delta$ -SCF) approach (Section 2.1.1), and the Many-Body perturbation theory (Section 2.2) through the GW (Section 2.2.1) and the Bethe–Salpeter (Section 2.2.2) methods.

The study of the physical systems is presented in Sections 3–5. We start from the systems where the quantum confinement acts in all the three spatial dimension, thus considering zero-dimensional systems. Starting from the analysis of hydrogenated Si-NCs (Section 3.1.1) we then consider the effect of oxidation (Section 3.1.2), and finally of an embedding matrix (Section 3.2). The particular case of how doping changes the structural, electronic and optical properties of the nanocrystals is discussed in Section 3.3. Here we study three different regimes: single-doped, co-doped and multi-doped Si nanocrystals (see Sections 3.3.1–3.3.3). Moreover the problem of screening in nanostructures has also been considered in Section 3.3.4.

Next we consider one-dimensional quantum confined systems in Section 4. Here we present the electronic and optical properties of Si and Ge nanowires (see Section 4.1) grown in different directions and with different diameters, considering also the presence of doping impurities (see Section 4.2).

Indeed we study the two-dimensional systems in Section 5. In this section we will analyze the structural, electronic and, in particular, the optical properties of Si and Ge based nanofilms (Section 5.1), of Si superlattices and multiple quantum wells where  $\text{CaF}_2$  and  $\text{SiO}_2$  are the barrier mediums (Sections 5.2 and 5.3). The quantum confinement effect and the role of symmetry will be considered, changing the slab thickness and orientation, and also the role of interface O vacancies will be discussed.

Conclusions are presented in Section 6.

## 2. THEORETICAL METHODS

Electronic and optical properties of complex systems are now accessible thanks to the impressive development of theoretical approaches and of computer power. Surfaces, nanostructures, and even biological systems can now be studied within ab-initio methods [53,54]. In principle within the Born-Oppenheimer approximation to decouple the ionic and electronic dynamics, the equation that governs the physics of all those systems is the many-body equation:

$$\left( \sum_i -\frac{1}{2} \nabla^2 \mathbf{r}_i + V_{\text{ext}} + \frac{1}{2} \sum_{i \neq j} \frac{1}{|\mathbf{r}_i - \mathbf{r}_j|} \right) \Psi(r_1, r_2, \dots, r_N) = E \Psi(r_1, r_2, \dots, r_N) \quad (1)$$

with  $V_{\text{ext}}$  being the ionic potential. Unfortunately a direct solution of Equation (1) is a formidable task, not only for realistic systems but even for  $N \geq 2$ . It is hence necessary to resort to approximations, or to different approaches. The static (Section 2.1) DFT avoids dealing directly with the many-body equation by mapping the interacting system into a fictitious non-interacting system (which is then described by single particle equations); the Green's function approach (Section 2.2.1), instead, maps the many-body electronic problem to a system of quasi-particles, which describe the excitations in terms of a particle of finite lifetime, that represent the extra electron (and/or the extra hole added to the system) plus its screened interaction with the electrons of the system. In next sections, we review the theoretical approaches used to calculate ground state properties, band structures, and optical spectra.

## 2.1. The density functional theory

Density functional theory (DFT) treats the case of an external, time independent potential, and is based on the Hohenberg and Kohn theorem [55], which proves that all the ground state properties of an interacting electronic system, including, in principle, the many-body wave function, could be expressed as unique functionals of the electronic density alone. In particular this assertion is valid also for the total energy  $E$  of the system. For the total energy functional  $E[n]$ , the variational principle ensures that for a given density  $n(r)$ ,  $E[n(\mathbf{r})] \geq E_{GS}$  where  $E_{GS}$  is the ground state energy of the system. The energy functional finds its minimum at the ground state density  $n_{GS}$ , for which  $E[n_{GS}] = E_{GS}$ . This theorem leads, in principle, to a straightforward method for computing ground state properties, but the explicit form of the functional in terms of the density is not known and such an explicit functional may not exist. Once given an approximation for the functional dependence of  $E$ , the ground state density can be obtained by a minimization procedure of the energy functional. Kohn and Sham [56], introduced an ad hoc separation of the terms contributing to the total energy  $E$ : the electron-electron interaction and the kinetic energy  $T$  of the interacting N-electron system. The advantages of this separation are: (1) it provides a single particle scheme to obtain the ground state density and total energy, and (2) to have an expression in which the approximations to the unknown part would be, in many cases, not as relevant as before. In the KS scheme the total energy functional of the interacting system is written as:

$$E[n] = T_0[n] + E_H[n] + \int d\mathbf{r} n(\mathbf{r}) v_{\text{ext}}(\mathbf{r}) + e_{xc}[n], \quad (2)$$

where  $T_0$  is the kinetic energy of a non-interacting system with density  $n$ ,  $E_H$  is the Hartree contribution to the total energy, and  $e_{xc}$  is the remaining part of the total energy which contains exchange-correlation contributions plus the difference between the kinetic energy of the interacting N-electron system  $T$  and the kinetic energy  $T_0$  of the non-interacting system. The main idea underlying this approach is to map the study of the (complicated) interacting system into the study of a (simpler) non interacting fictitious system whose Hamiltonian is written as:

$$\left[ -\frac{1}{2} \nabla^2 + v_{\text{ext}} + v_H + V_{xc} \right] = \varepsilon_i \phi_i(\mathbf{r}) \quad (3)$$

and which has, by construction, the same ground state density of the interacting system:

$$n(r) = \sum_i f_i |\phi_i(\mathbf{r})|^2 \quad (4)$$

with  $f_i$  being the occupation number of the state  $i$ . In Equation (3)  $V_{xc} = \delta E_{xc}[n]/\delta n$  is the exchange and correlation potential of the interacting system. It is now possible, given an approximation for  $E_{xc}[n]$ , to solve the Kohn–Sham Equations (3) and (4) self consistently and calculate the density of the interacting (real) system via Equation (2). Once the density is known, it is possible to calculate the energy of the ground state of the interacting system and hence, by proper minimization, to find its ground state geometry. The simplest and most common approximation to  $E_{xc}$  is the Local Density Approximation (LDA) given by [57]:

$$E_{xc}^{\text{LDA}} = \int d\mathbf{r} n(\mathbf{r}) \varepsilon_{xc}^{\text{heg}}(n), \quad (5)$$

where  $\varepsilon_{xc}^{\text{heg}}(n)$  is the exchange–correlation energy per electron of a homogeneous electron gas of density  $n$ . It is worth noting that the Kohn–Sham equations, representing a fictitious auxiliary system, have in principle no physical meaning. Nevertheless, their eigenvalues are often interpreted as one electron excitation energies corresponding to the excitation spectra of the system upon removal or addition of an electron, and DFT is in this way used to calculate band structures. The qualitative agreement with experiments is often remarkable, but not quantitative: the electronic gaps of semiconductors are, as a matter of fact, always systematically underestimated within DFT.

### 2.1.1. The $\Delta$ -self-consistent approach: Absorption, emission and Stokes shift

What happens when an e–h pair is excited in the system is that the charge density distribution changes, thus perturbing the forces acting on the atoms. The ions follow the excitation relaxing to a new equilibrium geometry, provided that the time taken by this process is shorter than the e–h pair recombination time. Therefore, the excitation and de-excitation processes involve two atomic configurations, that we can call ground-state (GS) and excited-state (EXC) geometries. This gives rise to four possible electronic/atomic configurations with their corresponding total energies, as follows:

1. ground state as the starting point, whose total energy is  $E_1$ ,
2. one e–h pair induced by the excitation, described by the excited-state level occupation but in the ground-state geometry, whose total energy is  $E_2$ ,

3. cluster relaxation in the presence of the e-h pair, toward the excited-state minimum energy geometry, whose total energy is  $E_3$ ,
4. e-h pair recombination, ground-state occupation, excited-state geometry, total energy  $E_4$ .

After the recombination the system can eventually relax toward the starting, ground-state geometry. As we will see the excitation can induce significant changes on the electronic and structural properties of the system and, mostly, there is a strong interplay between the electronic level occupation and the cluster geometry. For systems with a spatial confinement, i.e., with free-exciton radii larger than, or, of the order of their spatial extent, the lowest pair-excitation energies  $\epsilon_{ex}$  can be rigorously expressed in terms of DFT-LDA total energies. Usually one defines  $\epsilon_{ex} = E(N+1) + E(N-1) - 2E(N)$  using the ground-state energies  $E$  of the  $N+1$ ,  $N-1$ , and  $N$  electron system. However, in this definition the effect of the attractive screened Coulomb interaction of the excited electron and hole pair is missing. In order to account for the excitonic effect, we use the  $\Delta$ -SCF approach, which is based on the study of two different electronic configurations for the system:

- initial state: Ground State

$$\vec{\gamma}_{\text{gs}} = \begin{cases} \gamma_i = 1 & i = 1, \dots, N \\ \gamma_i = 0 & i > N \end{cases}$$

- final state: Neutral Excited State

$$\vec{\gamma}_{\text{exc}} = \begin{cases} \gamma_i = 1 & i = 1, \dots, (h-1), (h+1), \dots, N \quad \text{and} \quad i = e \ (e > N) \\ \gamma_i = 0 & i = h \quad \text{and} \quad i > N, i \neq e \end{cases}$$

In the last configuration a particle-hole pair is considered in the system promoting an electron from the valence band ( $i = h$ ) to a conduction band ( $i = e$ ). For this reason the method is also called constrained DFT. The excitation energy of the many-electron system is the difference in total energy between two self-consistent calculations with the occupations described above, i.e.:

$$E_{\text{exc}} = E_{\vec{\gamma}_{\text{exc}}} - E_{\vec{\gamma}_{\text{gs}}} \tag{6}$$

and should give the optical gap (since the initial and final states are both neutral). In our particular calculation the total energy  $E_{\vec{\gamma}_{\text{exc}}}$  is calculated with the constraint that the HOMO (Highest Occupied Molecular Orbital) of the ground-state system contains a hole  $h$ , placing the corresponding electron  $e$  into the LUMO (Lowest Unoccupied Molecular Orbital) of the ground-state system. When the atomic geometry of the nanocrystal is

optimized in the ground-state configuration, the corresponding calculated pair-excitation energies  $\epsilon_{ex}^A = E_2 - E_1$  define the optical absorption (A) edges. We also relax the nanostructure with an excited electron–hole pair. At the resulting geometry, the lowest emission (E) energy  $\epsilon_{ex}^E = E_3 - E_4$  is calculated. The difference of the two energies ( $\epsilon_{ex}^A - \epsilon_{ex}^E$ ) defines the Stokes or Frank-Condon shift, which is due to the lattice relaxation induced by the electronic excitation. Through this method one can extract the absorption and emission energies that are different with respect to the HOMO–LUMO gaps obtained for both the ground and excited state configurations; the latter are actually affected by the well known problem of the underestimation of the gap by all DFT calculations.  $\Delta$ -SCF can yield good results when it is possible to simulate the excitations occupying just one-particle orbital; this immediately excludes the possibility of describing those excitations that are not easily described in terms of isolated single particle transitions. Furthermore, this method works in finite systems, but not in infinite ones. This is because the main contribution in  $\Delta$ -SCF is the Hartree relaxation that for an extended system is negligible, leaving the system energy dominated by other contributions. Through the  $\Delta$ -SCF method it is not possible to obtain the lineshape of the optical spectra that allow a direct comparison with experimental data, anyway, using the ground and excited state optimized geometry calculated within this scheme we can calculate the absorption and emission spectra, evaluating the imaginary part of the nanostructure dielectric function ( $\epsilon_2(\omega)$ ) through first-principle calculations also beyond the one-particle approach. The emission spectrum is calculated, in a first approximation, as the time reversal of the absorption [58]. Strictly speaking,  $\epsilon_2(\omega)$  corresponds to an absorption spectrum in a new structural geometry, the EXC geometry, with the electronic configuration of the GS. For the first time, we also consider the electron–hole interaction in the emission geometry. This different approach, where the many-body effects are combined with the study of the structural bond distortion at the Si-NC surface in the EXC, accounts both for the absorption and PL spectra. Starting from the calculated self-consistent electronic properties, the imaginary part of the dielectric function can be computed in the optical limit:

$$\epsilon_2^\alpha(\omega) = \frac{4\pi^2 e^2}{m^2 \omega^2} \sum_{v,c} \frac{2}{V} \sum_k |\langle \psi_{c,k} | p_\alpha | \psi_{v,k} \rangle|^2 \times \delta[E_c(k) - E_v(k) - \hbar\omega], \quad (7)$$

where  $\alpha = (x, y, z)$ ,  $E_v$  and  $E_c$  denote the energies of the valence  $\psi_{v,k}$  and conduction  $\psi_{c,k}$  band states at a point  $k$ , and  $V$  is the supercell volume. From the calculated  $\epsilon_2$  the real part  $\epsilon_1$  is obtained by Kramers-Kronig transformation, after having attached a tail to  $\epsilon_2$  for energies greater than

15 eV following Ref. [59]. The optical-absorption coefficient

$$\alpha(\omega) = \frac{\omega}{nc} \epsilon_2(\omega) \quad (8)$$

is directly related to  $\epsilon_2$ , thus  $\epsilon_2$  contains the necessary information about the absorption properties of the material.

## 2.2. The Many-Body perturbation theory

### 2.2.1. The GW approach

Underestimation of the electronic gaps in DFT calculations finds its origin not in a deficiency of the theory, but in the incorrect use we make of the Kohn–Sham equations. In fact, even if the Kohn–Sham equations have the form of single-particle Schrödinger-like equations, their eigenvalues are not the excited state energies. DFT is an exact theory for ground state properties, but there is no strict theoretical justification to use it to obtain excitation energies. It is important to note that, in the determination of the electronic band structure, we are dealing with energy differences between the system with  $N$  electrons and the system with  $N - 1$  (direct photoemission spectroscopy) or  $N + 1$  (inverse photoemission spectroscopy) electrons. It is hence natural to change over to the Green's function formalism [60]. The one-electron Green's function is defined as the probability amplitude that an electron or a hole, created at time  $t_1$  and point  $r_1$  will be detected at time  $t_2$  and point  $r_2$ , that is, the probability amplitude of the electron (hole) propagation from  $r_1$  to  $r_2$  in the time interval  $(t_2 - t_1)$ . Because of this interpretation, the Green's function is also called the one-electron propagator. After a Fourier transform into the frequency domain, the Green's function  $G$  can be formally written as

$$G(\mathbf{r}_1, \mathbf{r}_2, \omega) = \sum_s \frac{\Psi_{0s}(\mathbf{r}_1)\Psi_{s0}^+(\mathbf{r}_2)}{\omega - \varepsilon_s - \mu + i\delta} + \sum_{s'} \frac{\Psi_{0s'}^+(\mathbf{r}_2)\Psi_{s'0}(\mathbf{r}_1)}{\omega + \varepsilon_{s'} - \mu - i\delta}, \quad (9)$$

where  $s$  and  $s'$  run over the  $N + 1$  and  $N - 1$  electrons excited states,  $\Psi_{0s}(\mathbf{r})$  ( $\Psi_{0s'}(\mathbf{r})$ ) is the expectation value of the creation operator of an electron at position  $\mathbf{r}$  between the  $N$  particle ground state and the  $N + 1$  ( $N - 1$ ) particle excited state labelled by  $s$  ( $s'$ ), and  $\varepsilon_s$  ( $\varepsilon_{s'}$ ) is the energy of the  $N + 1$  ( $N - 1$ ) excited states; the infinitesimally small imaginary term  $i\delta$  is needed for the convergence of the Fourier transform over the time variable. In expression (8) all the main ingredients of photoemission experiments appear, i.e. the photon energy  $\omega$  and the energy differences between the  $N$  electron system and the  $N \pm 1$  electron excited system. This explains why Green's functions are the main tools for band structure calculations: the excitation energies of a system are obtained by the determination of the poles of  $G$ . The Green's

function cannot be calculated exactly for realistic systems. It obeys a Dyson equation of the form

$$G(1, 2) = G_0(1, 2) + \int d(34)G_0(1, 3)\Sigma(3, 4)G(4, 2), \quad (10)$$

where  $G_0$  is the non-interacting Green's function and  $\Sigma$  is the self-energy, a non-hermitian, non-local and energy dependent operator. In this framework, by introducing the equation of motion for  $G$ , we can obtain the so called quasiparticle equation:

$$\left[ -\frac{\nabla^2}{2} + V_{\text{ext}}(\mathbf{r}_1) + V_H(\mathbf{r}_1) \right] \phi_s(\mathbf{r}_1, \omega) + \int d\mathbf{r}_2 \Sigma(\mathbf{r}_1, \mathbf{r}_2, \omega) \phi_s(\mathbf{r}_2, \omega) = \varepsilon_s(\omega)(\mathbf{r}_1, \omega). \quad (11)$$

The energies  $\varepsilon$  are the poles of the Green's function, so that the solution of Equation (11) directly gives the electronic band structure of the system. It is worth noticing that this equation reduces to the Hartree equations when  $\Sigma = 0$ , to the Hartree-Fock ones when  $\Sigma = iGV$ , and to the Kohn-Sham equations when, instead of  $\Sigma$ , a local, hermitian and energy independent operator is taken:  $\Sigma \rightarrow V_{xc}^{\text{KS}}(r)$ . This observation gives an *a posteriori* justification of the use of the Kohn-Sham equations to calculate the excitation energies; the qualitative agreement between DFT and experimental band structure comes from the fact that, somehow, the Kohn-Sham equations already carry a lot of physics, containing, at least approximately, exchange and correlation effects. In other words,  $V_{xc}^{\text{KS}}(r)$  is often a quite good approximation for the *true* self-energy  $\Sigma$ . In the same way in which in DFT we have to use an approximation for  $V_{xc}^{\text{KS}}$ , we now have to face the problem of finding a suitable expression for  $\Sigma$ . But at odds with the DFT case, within the Many-Body theory we have a closed set of equations, the Hedin Equations [61], which together with Equation (10) define implicitly the self-energy  $\Sigma$ :

$$\begin{aligned} \Sigma(12) &= i \int G(13)\Gamma(324)W(41)d(34); \\ W(12) &= v(12) + \int v(13)P(34)W(42)d(34); \\ P(12) &= -i \int G(13)G(41)\Gamma(342)d(34); \\ \Gamma(123) &= \delta(12)\delta(13) + \int \frac{\delta\Sigma(12)}{\delta G(45)}G(46)G(75)\Gamma(673)d(4567), \end{aligned} \quad (12)$$

where  $\Gamma$  is called vertex function,  $P$  is the polarization operator and  $W$  is the dynamically screened potential,  $W = \varepsilon^{-1}v$ .

In principle, the Hedin equations could be solved self-consistently, with an iterative procedure; in practice full self-consistency is never achieved for realistic systems. As a first step we can neglect the vertex corrections by assuming  $\Gamma(123) = \delta(12)\delta(13)$ ; in this way the self-energy operator takes the form  $\Sigma = iGW$ , which is the famous GW approximation [62,63]. At present computing quasiparticle energies within the GW approximation represents the most refined method for band structure calculation. The GW method can be applied to the calculation of the band structures of solids and surfaces, and to the determination of the energy levels of molecules and of atoms. In order to describe optical spectra, we have to take into account excited states of a completely different nature with respect to the ones involved in photoemission spectroscopy. In the latter, the final state of the system is charged, since one electron has been removed or added to it; in the former, instead, the system exchanging energy with the probe, is left in what is called a neutral excited state (see Figure 1c). Excitons are examples of neutral excited states that are commonly detected by optical spectroscopy; in a very schematic way excitons can be thought as bounded electron-hole states. The physical quantity which is directly connected to this spectrum is the macroscopic dielectric function  $\varepsilon_M$  that, following the derivation of Adler and Wiser [64], is given, in terms of the microscopic dielectric function,  $\varepsilon_{G,G'}(q, \omega)$  by:

$$\varepsilon_M(\omega) = \lim_{q \rightarrow 0} \frac{1}{(\varepsilon(q, \omega))_{G=0, G'=0}^{-1}}. \quad (13)$$

The absorption spectrum is proportional to the imaginary part of the macroscopic dielectric function. Adopting the same level of approximation that we have introduced to obtain GW quasiparticle energies, i.e. neglecting the vertex correction by putting  $\Gamma = \delta\delta$ , we get the so called random phase approximation (RPA) for the dielectric matrix. Within this approximation, neglecting local field effects, the response to a longitudinal field, for  $q \rightarrow 0$ , is:

$$\varepsilon_M(\omega) = 1 - \lim_{q \rightarrow 0} v(q) \sum_{vc} \frac{|\langle v | e^{-iqr} | c \rangle|^2}{\omega - (\varepsilon_c - \varepsilon_v) - i\eta}, \quad (14)$$

where  $|v\rangle(|c\rangle)$  represent the valence (conduction) single particle state and  $\varepsilon_v(\varepsilon_c)$  is its corresponding energy. From Equation (14) we see that the sum of all possible independent transitions gives rise to the spectra, its structures are located at quasiparticle energy differences and the line shape is determined by the matrix elements of  $e^{iqr}$  between a valence state and a conduction state independently for each transition. In fact, in a non interacting quasiparticle scheme, the neutral excited state can be seen to be a sum of independent

excitations of one electron from the valence to the conduction band. The spectrum may also be strongly dependent on local field effects, which must be included for highly anisotropic systems such as surfaces, nanowires and clusters. Even including local field effects the optical spectra of solids obtained within RPA are often not even in qualitative agreement with experiments. Due to some fortuitous cancellation of errors, DFT-RPA can sometimes yield very good agreement with experiment, but it should be stressed, however, that such good quantitative agreement is not generally found.

### 2.2.2. The Bethe–Salpeter equation

The vertex corrections cannot be completely neglected if we want to obtain optical spectra in agreement with experiments. Neglecting vertex corrections means to neglect the interaction between the hole and the electron that are formed within the polarization processes of the system. In fact putting  $\Gamma = \delta\delta$  in the Hedin equation for  $P$ , leads to an expression for it, namely  $P = -iGG$ , in which the hole and the electron propagators are independent of one another. In the description of absorption experiments, in which the excited electron remains in the sample, it is evident that the effects of the electron–hole interaction, i.e. the excitonic effects, cannot be neglected. The effects of the electron–hole interaction in the spectra can be included in MBPT through an effective two-body Hamiltonian, the so called excitonic Hamiltonian, which is the projection of the Bethe–Salpeter equation for the four-point modified polarizability  ${}^4\bar{P}$

$${}^4\bar{P} = {}^4P_{IQP} + {}^4P_{IQP}K{}^4\bar{P} \quad (15)$$

in the transition space, i.e. into a basis made of couples of single quasiparticle states, usually labelled by band and wave vector indices. The kernel  $K$  of this integral equation contains an electron–hole exchange  $\bar{v}$  and an electron–hole attraction  $-W$  term. The excitonic Hamiltonian is not necessarily hermitian, however, in calculations just its hermitian part is usually taken into account, which is:

$$H_{(vck)(v'c'k')}^{2p,\text{exc}} = (E_{ck} - E_{vk'})\delta_{vv'}\delta_{cc'}\delta_{kk'} + 2v_{vck}^{v'c'k'} - W_{vck}^{v'c'k'}. \quad (16)$$

Here  $E_{ck}$ ,  $(E_{vk'})$  are the quasiparticle energies, calculated within the GW approximation, of the states  $(ck)$  and  $(vk')$ . In terms of the eigenvalues and eigenvectors of the excitonic Hamiltonian, namely:

$$H_{(n_1n_2)(n_3n_4)}^{2p,\text{exc}} A_{\lambda}^{(n_3n_4)} = E_{\lambda}^{\text{exc}} A_{\lambda}^{(n_1n_2)} \quad (17)$$

the macroscopic dielectric function is:

$$\varepsilon_M(\omega) = 1 - \lim_{q \rightarrow 0} v(q) \sum_{\lambda} \frac{\left| \sum_{(n_1 n_2)} \langle n_1 | e^{-iqr} | n_2 \rangle A_{\lambda}^{(n_1 n_2)} \right|^2}{E_{\lambda}^{\text{exc}} - \omega - i\eta}, \quad (18)$$

where each label  $n_i$  represents a couple of band and wave vector indices. Comparing this formula with the RPA dielectric function Equation (14), we can see that in this case the dielectric function has poles at the eigenvalues of the excitonic Hamiltonian which are no longer differences of occupied and unoccupied quasiparticle state energies. This fact usually moves the position of the structures in the spectra to lower energies. Moreover, as we can see from Equation (17), each eigenstate of the excitonic Hamiltonian (17) is made by a sum of independent quasiparticle transitions; each transition contributes to it with a weight equal to  $A_{\lambda}^{n_1 n_2}$ . This mixing of independent transitions is present in the numerator of the dielectric function Equation (18) and its effect is to strongly modify the lineshape of the spectra. From Equation (18), we can see that to obtain the macroscopic dielectric function we need to diagonalize the excitonic Hamiltonian and to know the quasiparticle wave functions (in order to compute the dipole matrix elements present in the numerator). Usually in most ab-initio calculation, it is assumed that Kohn-Sham wave functions are a very good approximation to the quasiparticle ones, the calculation of  $W$  is limited to a static RPA screening, and the quasiparticle energies are computed within the GW approximation of the self energy. To summarize, in order to compute the excitonic spectra we need a well converged structure calculation, Kohn-Sham wave functions, quasiparticle energies within GW and the (statically) screened Coulomb interaction present in the excitonic Hamiltonian.

### 3. ZERO-DIMENSIONAL SYSTEMS

#### 3.1. Free-standing silicon nanocrystals

In a Si zero-dimensional system the strong quantum confinement can increase the optical infrared gap of bulk Si and consequently shift the optical transition energies towards the visible range [65,66]. This is the reason for which silicon nanocrystals (Si-NCs) with a passivated surface are used as the natural trial model for theoretical simulations on Si based light emitting materials, such as porous Si or Si nanocrystals dispersed in a matrix. In this section we present a comprehensive analysis of the structural, electronic and optical properties of Si-NCs as a function of size, symmetry and surface passivation. We will also point out the main changes induced

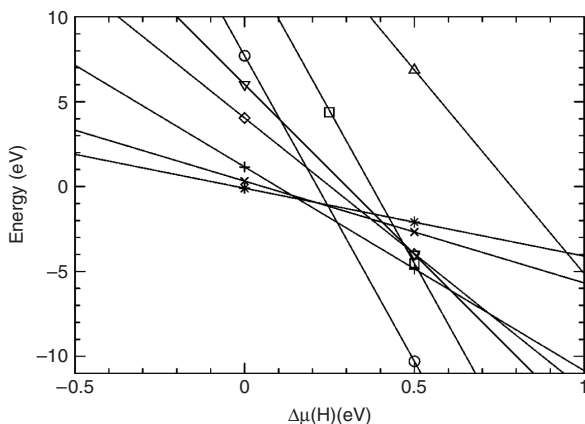


**Figure 1** Calculated phase diagram of the hydrogen exposed  $\text{Si}_1$  (stars),  $\text{Si}_2$  (crosses  $\times$ ),  $\text{Si}_5$  (crosses +),  $\text{Si}_{10}$  (diamonds),  $\text{Si}_{14}$  (down triangles),  $\text{Si}_{29}$  ( $\text{Si}_{29}\text{H}_{24}$  up triangles and  $\text{Si}_{29}\text{H}_{36}$  squares) and  $\text{Si}_{35}$  (circles) clusters. The chemical potential of H,  $\mu_{\text{H}}$ , is given with respect to molecular H.

by the nanocrystal excitation through a  $\Delta$ -SCF (see Section 2.1.1) or a Many-Body perturbation theory approach (see Section 2.2).

### 3.1.1. Hydrogenated silicon nanocrystals

The starting point of our study is represented by Si-NCs whose surface is fully passivated by hydrogen atoms (H-Si-NC). The study of H-Si-NCs has been done within DFT, using a pseudopotential, plane-wave approach. All the calculations have been performed with the ABINIT code [67]. Norm-conserving, non-local Hamann-type pseudopotentials have been used. The Kohn-Sham wave functions have been expanded within a plane-wave basis set, choosing an energy cutoff of 32 Ry. The gradient-corrected Perdew-Burke-Ernzerhof (GGA-PBE) exchange-correlation functional has been used for both structural and electronic states calculations. The calculations performed are not spin-polarized. Each H-Si-NC has been embedded within a large cubic supercell, containing enough vacuum to make nanocrystal-nanocrystal interactions negligible [68]. The calculations for each cluster have been performed both in the ground and excited states as described in Section 2.1.1. The starting configuration for each cluster has been fixed with all Si atoms occupying the same position as in the bulk crystal, and passivating the surface with H atoms placed along the bulk crystal directions, at a distance determined by studying the  $\text{SiH}_4$  molecule. It is worth pointing out that the starting H-Si-NC has  $T_d$  symmetry, which is kept during relaxation in the ground state configuration. Nevertheless for excited state configurations such symmetry is generally lost, due to the occupation of excited energy levels. We have first investigated the stability of Si nanoclusters exposed to an H atmosphere looking at their formation

energies as a function of the size. The interest in this kind of calculation consists in understanding which clusters are more likely to form under different growth conditions. The stability of each cluster can be evaluated by calculating the formation enthalpy ( $F$ ) through the formula:

$$F(Si_N H_M) = E_{\text{TOT}}(Si_N H_M) - N\mu_{\text{Si}} - M\mu_{\text{H}}, \quad (19)$$

where  $E_{\text{TOT}}$  is the ground-state total energy of a given  $Si_N H_M$  cluster, and  $\mu_{\text{Si}}$  and  $\mu_{\text{H}}$  the chemical potentials for Si and H, respectively. The chemical potential for Si ( $\mu_{\text{Si}}$ ) is fixed at the bulk value, while the chemical potential for H changes to simulate different growth conditions. Figure 1 shows the phase diagram of the clusters with respect to different conditions in the H atmosphere. All the possible values for  $\mu_{\text{H}}$  we have considered have been referred to the calculated molecular H chemical potential. Thus,  $\Delta\mu_{\text{H}} = 0$  corresponds to the situation where the clusters are exposed to molecular H at  $T = 0$  K, negative values of  $\Delta\mu_{\text{H}}$  correspond to a H-poor atmosphere in the growth chamber, positive values of  $\Delta\mu_{\text{H}}$  mean that also atomic H is available (H-rich conditions that exists when Si nanoclusters are formed by reducing  $SiCl_4$  with metal hydrides [69] or by HF etching of bulk Si [70]). All the considered clusters are passivated by H atoms placed along the bulk Si crystal directions except for the  $Si_{29}H_{24}$  structure, which is obtained from  $Si_{29}H_{36}$  by simply removing 12 hydrogens. This induces a surface reconstruction with the formation of Si–Si dimers. As expected, the  $Si_{29}H_{24}$  structure, when compared with  $Si_{29}H_{36}$ , is stabler in H-poor growth conditions (not visible in Figure 1), and less stable in an H-rich atmosphere. The exposure to molecular H or to an H-poor atmosphere gives higher stability to smaller clusters, while in H-rich growth conditions larger clusters are stabler. On increasing the H concentration (that is, moving from left to right in Figure 1) the stablest cluster changes from  $Si_1H_4$  to  $Si_5H_{12}$  and, finally, to  $Si_{35}H_{36}$ .

After the stability analysis we have investigated the structural distortions caused by the relaxation of these structures in different electronic configurations. To qualitatively appreciate the structural changes, we have plotted in Figure 2 the relaxed structures of some of the considered clusters, both in ground- and excited-state configurations. The analysis of the structural properties reveals that the average Si–Si bond approaches the bulk bond length as the cluster dimension increases. In particular, moving from the center of the cluster toward the surface, a contraction of the outer Si shells is observed. The presence of a electron–hole pair in the clusters causes a strong deformation of the structures with respect to their ground-state configuration, and this is more evident for smaller systems and at the surface of the H-Si-NCs. This is what we expect, since for large clusters the charge density perturbation is distributed throughout the whole structure, and the effect it locally induces becomes less evident (small adjustments of

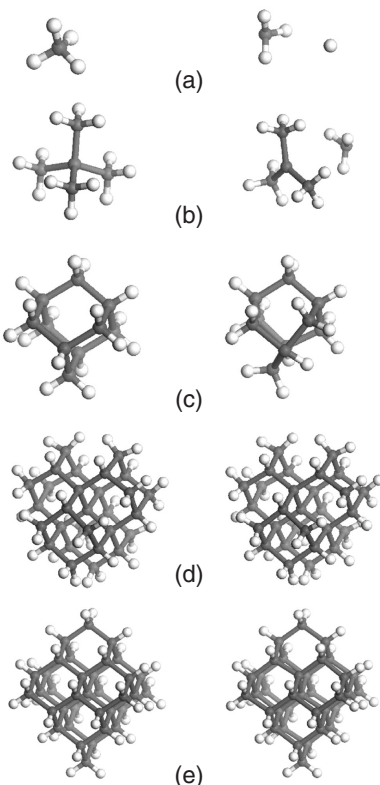


**Figure 2** Structural models for the (a)  $\text{Si}_1\text{H}_4$ , (b)  $\text{Si}_5\text{H}_{12}$ , (c)  $\text{Si}_{10}\text{H}_{16}$ , (d)  $\text{Si}_{29}\text{H}_{36}$  and (e)  $\text{Si}_{35}\text{H}_{36}$  clusters at relaxed geometry in the ground- (left panels) and excited-state (right panels) configuration.

bonds and angles occur with respect to the ground state). Baierle et al. [17] and Allan et al. [29] stressed the importance of bond distortion at the Si-NC surface in the excited state in creating an intrinsic localized state responsible for the PL emission. The structural analysis is immediately reflected in the electronic structure. In Table 1 we report the calculated energy gaps for the  $\text{Si}_1\text{H}_4$ ,  $\text{Si}_5\text{H}_{12}$ ,  $\text{Si}_{10}\text{H}_{16}$ ,  $\text{Si}_{29}\text{H}_{36}$  and  $\text{Si}_{35}\text{H}_{36}$  clusters in both the ground- and excited-state configurations.

One can note the expected decrease of the energy gap on increasing the cluster dimension and also that the excitation of the electron-hole pair causes a reduction of the energy gap, more significant as the cluster gets smaller. For small excited clusters the HOMO and LUMO become strongly localized in correspondence of the distortion, giving rise to defect-like states which reduce the gap. The distortion induced by the nanocluster excitation gives a possible explanation of the observed Stokes shift in these systems. The radiation absorption of the cluster in its ground state configuration induces a

**Table 1** Calculated values for the ground (GS) and excited (EXC) state HOMO–LUMO energy gaps and for the absorption and emission energies calculated within the  $\Delta$ -SCF approach for the considered H–Si–NC. All values are in eV

	Absorption	GS HOMO–LUMO gap	Emission	EXC HOMO–LUMO gap
Si <sub>1</sub> H <sub>4</sub>	8.76	7.93	0.38	1.84
Si <sub>5</sub> H <sub>12</sub>	6.09	5.75	0.42	0.46
Si <sub>10</sub> H <sub>16</sub>	4.81	4.71	0.41	0.55
Si <sub>29</sub> H <sub>36</sub>	3.65	3.58	2.29	2.44
Si <sub>35</sub> H <sub>36</sub>	3.56	3.50	2.64	2.74

**Table 2** Stokes Shift values for hydrogenated Si clusters: present work versus theoretical data present in literature. All values are in eV

H–Si Clusters	Diameter (nm)	Theory				
		This work	Ref. [75]	Ref. [76]	Ref. [79]	Ref. [80]
Si <sub>1</sub> H <sub>4</sub>	0.0	8.38				
Si <sub>5</sub> H <sub>12</sub>	0.45	5.67				
Si <sub>10</sub> H <sub>16</sub>	0.55	4.40	LDA QMC			
Si <sub>29</sub> H <sub>36</sub>	0.9	1.35	0.69	1.0	2.92	0.22
Si <sub>35</sub> H <sub>36</sub>	1.1	0.92	0.57	0.8		1.67
Si <sub>66</sub> H <sub>64</sub>	1.3		0.50			
Si <sub>87</sub> H <sub>76</sub>	1.5		0.22		0.32	
Si <sub>29</sub> H <sub>24</sub>	0.8	0.84	0.34	0.4		1.17

transition between the HOMO and LUMO levels, which for all these clusters is optically allowed. Such a transition is followed by a cluster relaxation in the excited state configuration, giving rise to distorted geometries (as previously shown) and to new LUMO and HOMO, whose energy difference is smaller than that in the ground-state geometry. It is between these two last states that emission occurs, thus explaining the Stokes shift. It is also worth pointing out how such a shift changes as a function of the dimension. The distortion being smaller for larger clusters, it is expected that the Stokes shift decreases on increasing the dimension. This is shown in Tables 1 and 2: in the first the HOMO–LUMO gap for both the ground and excited states together with the  $\Delta$ -SCF (see Section 2.1.1) absorption and emission energies are reported, while in the latter the derived Stokes shift compared with other theoretical data available in literature is shown.

A number of papers present in literature consider the HOMO–LUMO gaps of the ground and excited state as the proper absorption and emission energies; this leads to the wrong results, mostly for smaller clusters. In fact, from Table 1 it is clearly seen that the smaller the H–Si–NC, the greater is the difference between the absorption and HOMO–LUMO ground-state

(GS) gap and between emission and HOMO–LUMO excited-state (EXC) gap (Delerue et al. [71] have pointed out that for clusters with diameter larger than 1.2 nm there is a cancellation between the self-energy correction and Coulomb terms; thus the lowest excitonic energy is “correctly” predicted by the single-particle band gap. In our calculations, on going from smaller to larger clusters the difference between the HOMO–LUMO gap in the ground state and the absorption gap becomes smaller). In conclusion, trying to deduce the Stokes shift simply from the HOMO–LUMO gaps leads to errors, especially for small clusters. In particular, the GS HOMO–LUMO gap tends to be smaller than the absorption energy, while the EXC HOMO–LUMO gap tends to be larger than the emission energy.

When comparing our results for the ground state with other DFT calculations we note that there is, in general, a good agreement between them. Actually, for Si<sub>1</sub>H<sub>4</sub>, Grossman et al. [72] have found 7.8 eV for the HOMO–LUMO gap while Onida and Andreoni [73] have obtained 8.1 eV; these values have to be compared with our calculated 7.93 eV result. At the same time for the Si<sub>29</sub>H<sub>36</sub> cluster, our 3.65 eV calculated absorption gap is in nice agreement with the 3.6 eV [74] obtained with the same method both by Puzder et al. [75] and Franceschetti et al. [76]. It is worth mentioning that our results for the absorption gaps of the Si<sub>1</sub>H<sub>4</sub> (8.76 eV) and Si<sub>5</sub>H<sub>12</sub> (6.09 eV) clusters agree quite well with the experimental results of Itoh et al. [77]. They have found excitation energies of 8.8 eV and 6.5 eV respectively. GW calculations find an absorption gap of 9.0 eV for Si<sub>1</sub>H<sub>4</sub> [78], while LDA results by Hirao et al. [79] show a HOMO–LUMO gap of 4.62 eV and 3.32 eV for Si<sub>10</sub>H<sub>16</sub> and Si<sub>29</sub>H<sub>36</sub>, respectively. All these data are in very good agreement with ours. Regarding the Stokes shift, very little data exist in literature as Table 2 shows [75,76,79,80], and, in particular for really small H–Si–NCs (from Si<sub>1</sub>H<sub>4</sub> to Si<sub>10</sub>H<sub>16</sub>), no data exists at all. The dependence of the Stokes shift on the H–Si–NC size qualitatively agrees with the calculations of Puzder et al. [75] and Franceschetti et al. [76]. Nevertheless, it is seen that the data for the Si<sub>29</sub>H<sub>36</sub> cluster show a large spread, which can be attributed to the different approaches used. Experimentally, very few measurements exist on hydrogenated Si clusters and what emerges is a decreasing of the Stokes shift value with increasing cluster dimension [81,82]. Concerning the optical properties of the hydrogenated clusters and the comparison between different ab-initio methods, Figure 3 shows the absorption spectra of the Si<sub>5</sub>H<sub>12</sub> cluster calculated using different DFT-based methods [67]. In particular we have performed an LDA calculation (RPA-LDA, neglecting Local Fields), we have calculated the self-energy corrections within the GW method (RPA-GW), then the excitonic effects have been included, both performing a time dependent local density approximation (TDLDA) calculation and a fully excitonic calculation through the Bethe–Salpeter equation (BSE). As usual we note an underestimation of the optical gap in the RPA-LDA scheme with respect to the experimental value (6.5 eV) [77].

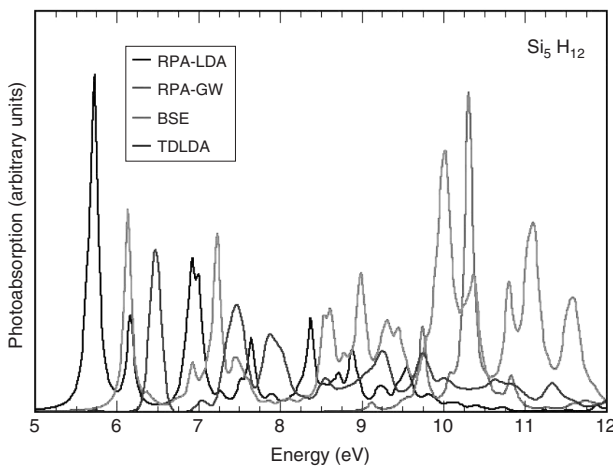


**Figure 3** Absorption spectra of the Si<sub>5</sub>H<sub>12</sub> cluster calculated using different DFT based methods: LDA-RPA black (black), GW-RPA red (dark gray), BSE violet (light gray), TDLDA blue (light black).

Concerning the RPA-GW method, the main result is a huge opening of the optical gap. The effects of the electron–hole interaction on the optical properties (BSE result) is also quite large, the excitonic binding energy is of the order of 3 eV, resulting in a sort of compensation with respect to the GW opening. Interestingly the BSE and TDLDA results are similar regarding the absorption onset and in agreement with the experimental result.

### 3.1.2. Oxidized silicon nanocrystals

Recent experimental data have shown strong evidence that the surface changes of Si-NCs exposed to O produce a substantial impact on their optoelectronics properties, thus oxidation at the surface has to be taken into account. In this section we will analyze the structural, electronic and optical properties of oxidized Si-NCs, discussing the effects of the different Si/O bond geometries and of size, and considering the specific case of multiple O passivation with silanone-like Si=O bonds [20–22]. Different theoretical approaches have been used, each of them based on the DFT in a plane-wave pseudopotential scheme. In some cases calculations both in ground and excited state electronic and/or structural configurations have been performed, through the  $\Delta$ -SCF method (see Section 2.1.1) [68,75,76, 83] or going beyond the DFT using the Many-Body perturbation theory (see Section 2.2). The first set of results concerns the ground state study of isolated oxidized nanocrystals in the DFT limit. As a first approach, two different codes have been used: FHI98MD [84] and CASTEP [85–87]. In the first case the electron–ion interaction has been described via norm-conserving pseudopotentials [88,89]; in the second case via ultrasoft

**Table 3** List of the studied clusters, classified by the type of surface passivation (rows) and by the core size (columns). Full-H stands for a passivation by H atoms only; Si–O–Si by H atoms plus O in the bridge geometry; Si=O by H atoms plus O in the double-bond geometry; and Si–O–Si + Si=O by H atoms plus O both in the bridge- and double-bond geometry

Bond/size	0.5 nm	0.7 nm	1.0 nm
full-H	Si <sub>10</sub> H <sub>16</sub>	Si <sub>14</sub> H <sub>20</sub> Si <sub>12</sub> H <sub>16</sub>	Si <sub>35</sub> H <sub>36</sub>
Si–O–Si	Si <sub>9</sub> H <sub>14</sub> >O	Si <sub>14</sub> H <sub>20</sub> >O <sub>2</sub> Si <sub>13</sub> H <sub>18</sub> >O Si <sub>12</sub> H <sub>16</sub> >O <sub>2</sub>	Si <sub>34</sub> H <sub>34</sub> >O
Si=O	Si <sub>10</sub> H <sub>14</sub> =O Si <sub>10</sub> H <sub>12</sub> =O <sub>2</sub> Si <sub>10</sub> H <sub>10</sub> =O <sub>3</sub> Si <sub>10</sub> H <sub>8</sub> =O <sub>4</sub> Si <sub>10</sub> H <sub>6</sub> =O <sub>5</sub> Si <sub>10</sub> H <sub>4</sub> =O <sub>6</sub>	Si <sub>14</sub> H <sub>18</sub> =O Si <sub>14</sub> H <sub>16</sub> =O <sub>2</sub> Si <sub>14</sub> H <sub>14</sub> =O <sub>3</sub> Si <sub>14</sub> H <sub>12</sub> =O <sub>4</sub> Si <sub>14</sub> H <sub>8</sub> =O <sub>6</sub> Si <sub>13</sub> H <sub>18</sub> =O Si <sub>12</sub> H <sub>16</sub> =O <sub>2</sub>	Si <sub>35</sub> H <sub>34</sub> =O Si <sub>35</sub> H <sub>32</sub> =O <sub>2</sub> Si <sub>35</sub> H <sub>30</sub> =O <sub>3</sub> Si <sub>35</sub> H <sub>28</sub> =O <sub>4</sub> Si <sub>35</sub> H <sub>24</sub> =O <sub>6</sub>
Si–O–Si+Si=O		Si <sub>13</sub> H <sub>16</sub> >O=O	

pseudopotentials [90]. Different cutoffs for the wave-function kinetic energy have thus been adopted: 680 eV in FHI98MD and 380 eV in CASTEP. The structural relaxation has been achieved using either code, while the optoelectronic properties at relaxed geometry have been determined with CASTEP. Five classes of clusters have been considered: one with a mean core diameter of 1.0 nm (Si<sub>35</sub>-core based), three with a mean core diameter of 0.7 nm (Si<sub>14</sub>-, Si<sub>13</sub>-, and Si<sub>12</sub>-core based), and one with a mean core diameter of 0.5 nm (Si<sub>10</sub>-core based). Two types of Si/O bond geometry have been extensively studied: the Si–O–Si bridge-bond and the silanone-like (Si=O) bond. The oxidized clusters have been built up substituting H and/or Si atoms of the initial H-capped structures (see previous subsection) with O atoms. In particular the Si=O bonds have been obtained by replacing, with one O atom, pairs of H atoms bonded to the same Si atom. At each O introduction we have studied the different possible configurations of the surface, i.e., different relative locations for the Si=O bonds, playing with the symmetry of the systems and with the possible O-double-bond sites available for each cluster. All the systems, classified by the type of Si/O bond and Si-core size, are listed in Table 3. All the clusters have been relaxed by total-energy minimization. The relaxation produces structural changes with respect to the initial geometry which strongly depend on the type of surface passivation. A full-H saturation, as expected, leaves the initial bulk-like structure of the Si core unchanged. When Si=O bonds are added at the surface, the modification of the Si core is very limited. In the relaxed geometry the Si=O bond orientation is always perpendicular to the surface,

**Table 4** Energy gap values for the Si-NC with mean diameter of 0.7 nm at relaxed geometry

Si-NC structures	Energy gap (eV)
Si <sub>14</sub> H <sub>20</sub>	4.1
Si <sub>14</sub> H <sub>20</sub> >O <sub>2</sub>	4.0
Si <sub>14</sub> H <sub>18</sub> =O	2.4
Si <sub>14</sub> H <sub>16</sub> =O <sub>2</sub>	2.3
Si <sub>14</sub> H <sub>14</sub> =O <sub>3</sub>	2.2
Si <sub>14</sub> H <sub>12</sub> =O <sub>4</sub>	2.1
Si <sub>14</sub> H <sub>8</sub> =O <sub>6</sub>	2.1
Si <sub>13</sub> H <sub>18</sub> >O	3.7
Si <sub>13</sub> H <sub>18</sub> =O	2.4
Si <sub>13</sub> H <sub>16</sub> >O=O	2.2
Si <sub>12</sub> H <sub>16</sub>	3.8
Si <sub>12</sub> H <sub>16</sub> >O <sub>2</sub>	3.6
Si <sub>12</sub> H <sub>16</sub> =O <sub>2</sub>	2.3

i.e., in the same plane of the two nearest Si–Si bonds, along the bisecting line. This final geometry, which does not depend on the number of Si=O bonds present at the surface, seems to be supported by an X-ray absorption fine-structure study on the interface between Si and SiO<sub>2</sub> [91], which reveals a strong Si/O bonding oriented preferentially closer to the surface normal. On the other hand, the introduction of the O atoms in the bridge configuration produces an appreciable modification of the Si core in the vicinity of the bond position, especially when the O are placed in between the first nearest-neighbor Si atoms (Si<sub>14</sub>H<sub>20</sub>>O<sub>2</sub>). The angle and bond-length variations go towards a final geometry for the Si–O–Si close to the quartz one.

Considering the large number of studied cases, for more clarity, we will first focus on clusters with the same Si-core size (core diameter of 0.7 nm) and finally discuss the role played by size.

Concerning the electronic properties we see from Table 4 that the energy band gap ( $E_g$ ) changes as a function of the Si/O bond type at the cluster surface. In comparison with the result for Si<sub>14</sub>H<sub>20</sub> we see, for the Si–O–Si bridge cases, a very small reduction in Si<sub>14</sub>H<sub>20</sub>>O<sub>2</sub> and a more evident one in Si<sub>12</sub>H<sub>16</sub>>O<sub>2</sub>. Only for Si<sub>14</sub>H<sub>16</sub>=O<sub>2</sub> a huge reduction of the energy gap happen. In this Si-NC, as just shown, the structural variations are very small; thus the reduction is practically due only to the presence of new Si=O-related states which strongly modify the band edges. This view is confirmed by the analysis of the distribution of HOMO and LUMO states (see Figure 4). It is clear from this figure how, only in the Si=O case, both HOMO and LUMO are localized around the O of the Si=O bonds; while, for the two Si–O–Si bridge cases, only part of the LUMO is around it, HOMO, in fact, maintains the character of the H-covered structure located along peculiar Si–Si bonds of the

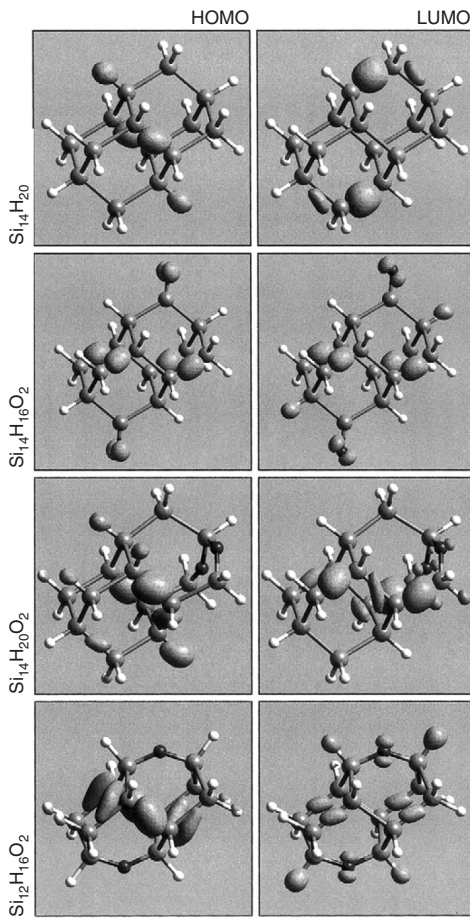


**Figure 4** Isosurfaces of the square modulus of the HOMO and LUMO for  $\text{Si}_{14}\text{H}_{20}$ ,  $\text{Si}_{14}\text{H}_{16}=\text{O}_2$ ,  $\text{Si}_{14}\text{H}_{20}>\text{O}_2$ ,  $\text{Si}_{12}\text{H}_{16}>\text{O}_2$  at the optimized geometry. The isosurfaces are plotted at 50% of their maximum amplitude.

Si skeleton. The electronic properties are instead less affected by the addition of Si–O–Si bridges; this is due to the HOMO state that, as already said, maintains its hydrogenated like character. The  $E_g$  is reduced, but not as in the Si=O bond cases. Also when the addition of O atoms implies the substitution of some atoms of the Si core, miming the attack of O towards the inner structure, the reduction is still of the order of a few tenths of eV. The addition of both types of bonds on the same structure ( $\text{Si}_{13}\text{H}_{16}>\text{O}=\text{O}$ ) produces a final  $E_g$  value strongly red-shifted, very close to the corresponding results for the double-bond case ( $\text{Si}_{13}\text{H}_{18}=\text{O}$ ). This means that the electronic, and consequently the optical, behavior of the clusters is mainly characterized by the double bonded O.

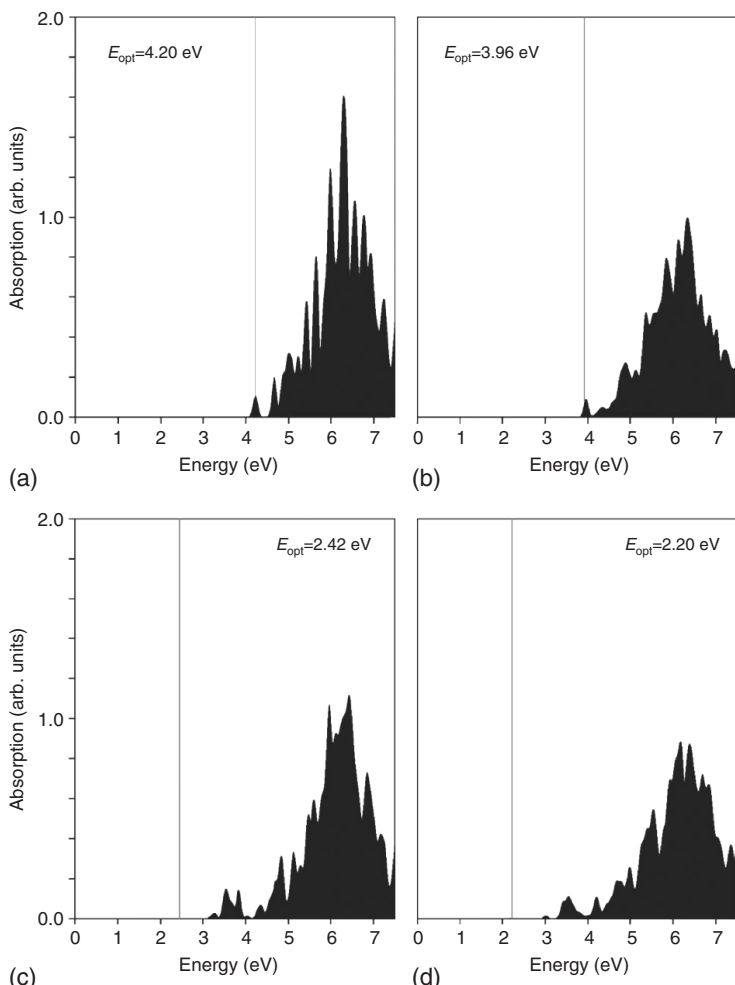


**Figure 5** Calculated absorption spectra for four different Si clusters: (a)  $\text{Si}_{14}\text{H}_{20}$ , (b)  $\text{Si}_{14}\text{H}_{20}>\text{O}_2$ , (c)  $\text{Si}_{14}\text{H}_{18}=\text{O}$ , (d)  $\text{Si}_{13}\text{H}_{16}>\text{O}=\text{O}$  (an artificial Gaussian smearing of 0.05 eV has been applied).

The results of the optical properties reflect the electronic ones. In Figure 5 we show, as an example, the absorption spectra of some of the clusters. In the presence of the  $\text{Si}=\text{O}$  bond, the first transitions in an absorption process involve the  $\text{Si}-\text{O}$  interface states only, while for the  $\text{Si}-\text{O}-\text{Si}$  bridge bonds the first transitions are still influenced by the crystalline Si structure. This results in a strong red-shift of the absorption onset when the double bonded O is present (compare Figures 5(a) and 5(c), whereas O in the bridge geometry slightly modifies the absorption behavior (Figure 5(b)). With the simultaneous presence of O in the double and bridge bond configuration

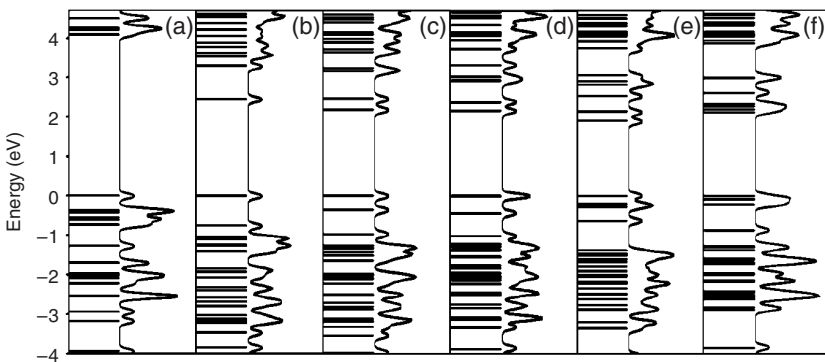


**Figure 6** Energy levels at  $\Gamma$  and TDOS for  $\text{Si}_{14}\text{H}_n\text{-O}_m$  clusters. (a)  $m = 0$ , (b)  $m = 1$ , (c)  $m = 2$ , (d)  $m = 3$ , (e)  $m = 4$ , and (f)  $m = 6$ .

(Figure 5(d)) the absorption onset is set exactly at the energy of the transition between HOMO and LUMO (which are Si=O related states), showing that the first optical transitions in this case are mainly due to the Si=O presence. In general it emerges that for all the oxidized clusters the absorption onsets correspond exactly to the HOMO-LUMO allowed transition.

In order to ideally simulate the air exposure of the crystallites, as for example in porous Si samples, the number of O atoms in the Si=O geometry has been progressively increased at the cluster surface. There is no linear  $E_g$  dependence on Si=O numbers; the more Si=O bonds are drawn at the surface the more new O-related states approach the band edges and accumulate there. The  $E_g$  arrives at a sort of saturation limit; only one Si=O bond is enough to abruptly reduce the  $E_g$  (in the  $\text{Si}_{14}$ -core-based case the  $E_g$  is reduced by 1.5 eV with the introduction of the first O) and this reduction necessarily has a chemical character. This red-shift weakly increases, increasing the number of Si=O bonds at the surface. This behavior is clearly shown in Figure 6, where, as an example, the energy levels and total density of states (TDOS) for the  $\text{Si}_{14}\text{H}_n\text{-O}_m$  clusters are reported. For one Si=O bond we see one new localized state at the top of the valence band and one at the bottom of the conduction band, within the gap relative to the fully hydrogenated case. For two Si=O bonds we clearly distinguish two states at both band edges; for three, four, and six they become three, four, and six. Thus, increasing the number of Si=O bonds at the surface causes a directly proportional number of localized states, which pile up at the band edges. When the Si=O bonds are placed in equivalent relative positions a level degeneracy is induced on the states within the gap.

Another way of seeing the  $E_g$  behavior as a function of the Si=O bond number is to plot the relative red-shift with respect to the full-H  $E_g$ , as done in Figure 7. The zeros corresponds to the full-H case. A saturation tendency is clearly displayed in all the three cases; this model with multiple Si=O

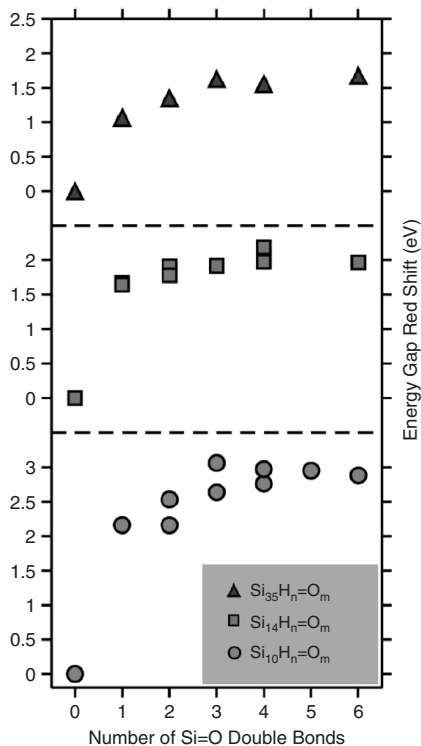


**Figure 7** Energy-gap red-shift for three different classes of clusters as a function of the number of  $\text{Si}=\text{O}$  bonds at the surface. Circles:  $\text{Si}_{10}\text{H}_n\text{O}_m$ ; squares:  $\text{Si}_{14}\text{H}_n\text{O}_m$  and triangles:  $\text{Si}_{35}\text{H}_n\text{O}_m$ . The red-shift is calculated as the difference between a specific surface configuration and the corresponding fully hydrogenated one (thus the zero in the plot for each class stands for the nonoxidized case  $m = 0$ ).

bonds at the surface reproduces, amazingly well, the experimental outcomes on the optical behavior of intentionally oxidized crystallites in porous Si samples [18]. Actually, in their experiment, Wolkin et al. [18] measure the PL behavior of freshly etched porous Si samples made of crystallites of various sizes. These spectra show a large PL red-shift when the samples are exposed to open air. A great amount of the reduction is achieved in the few first seconds of exposure [18] when the oxidation has just begun and it is supposed that only a few O atoms have attacked the surface. This means that our hydrogenated clusters with some Si-H bonds replaced by Si/O bonds can be a reasonable model for this type of samples at the beginning of the exposure [22].

Now, to go beyond the ground state properties of our oxidized Si-NC we focus on a smaller group of structures. In the  $\Delta$ -SCF scheme, two classes of systems have been studied, based on the  $\text{Si}_{10}$  and the  $\text{Si}_{29}$  core based nanoclusters [92]. Through a formation energy calculation, the bridge

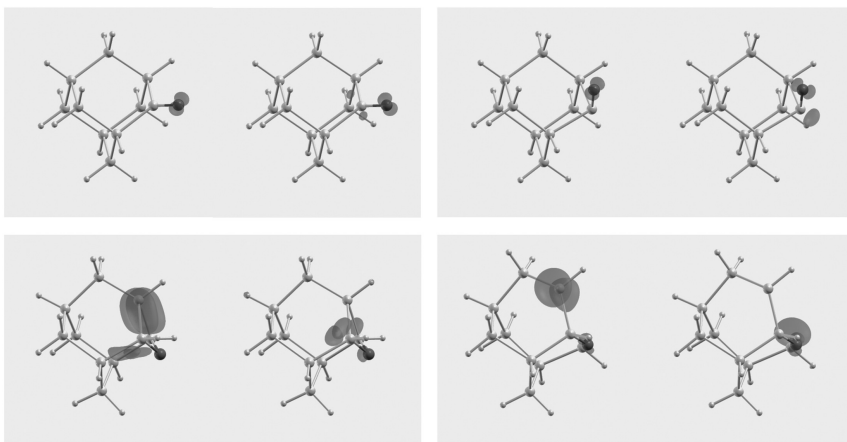


**Figure 8** Calculated HOMO (first and third column) and LUMO (second and fourth column) charge density for  $\text{Si}_{10}\text{H}_{14}\text{O}$ -double (top panel),  $\text{Si}_{10}\text{H}_{14}\text{O}$ -bridge (bottom panel) for the ground (first and second column) and excited (third and fourth column) states; the structures shown are the relaxed ones.

bonded configuration has been demonstrated to lead to the stablest isomer configuration by Gatti and Onida [93,94]. The geometries for the  $\text{Si}_{10}\text{H}_{14}>\text{O}$  (bridge bond) and the  $\text{Si}_{10}\text{H}_{14}=\text{O}$  (double bond) are shown in Figure 8, both for the ground and excited state electronic configuration. Full relaxation with respect to the atomic positions is performed within the DFT limit for all systems, both in the ground and excited configurations, using a norm conserving LDA pseudopotential with an energy cutoff of 60 Ry [95]. The ionic relaxation has produced structural changes with respect to the initial geometry which strongly depend on the type of surface termination. In the case of  $\text{Si}_{10}\text{H}_{14}=\text{O}$ , the changes are mainly localized near the O atom, in particular the angle between the double bonded O and its linked Si atom is modified (see Figure 8). In the bridge structure, instead, the deformation is localized around the Si–O–Si bond producing a considerable strain in the Si–Si dimer distances [94]. Similar results are obtained for the larger  $\text{Si}_{29}$  based clusters. The only difference is that now the distortion induced by the promotion of an electron is smaller, as expected, since for larger clusters the charge density perturbation is distributed throughout the structure, and the locally induced effect becomes less evident. These structural changes are reflected in the electronic and optical properties.

In Figure 8 we also show the HOMO and LUMO charge density for the systems studied. It is evident that in all cases these states are mainly localized in the distorted region of the cluster.

In Table 5 absorption and emission gaps are reported: the red-shift of the emission gap with respect to the absorption is less evident for the case of the cluster with the double-bonded O (see the Stokes shift values); the same

**Table 5** Stokes shift, i.e. difference between absorption and emission energy gaps calculated as total energy differences within the  $\Delta$ -SCF approach. All values are in eV

	Stokes shift	Absorption	Emission
Si <sub>10</sub> H <sub>14</sub> =O	1.70	2.79	1.09
Si <sub>10</sub> H <sub>14</sub> >O	3.90	4.03	0.13
Si <sub>29</sub> H <sub>34</sub> =O	1.65	2.82	1.17
Si <sub>29</sub> H <sub>34</sub> >O	0.28	3.29	3.01

**Table 6** Absorption and emission gaps calculated as HOMO–LUMO differences within DFT–LDA and GW approaches and as the lowest excitation energy when excitonic and local field effects (BS-LF) are included. In the last column the Stokes shift calculated in the BS-LF approximation is reported. In parenthesis the lowest dark transitions (when present) are also given. All values are in eV

	Absorption			Emission			Stokes Shift
	LDA	GW	BS-LF	LDA	GW	BS-LF	
Si <sub>10</sub> H <sub>14</sub> =O	3.3 (2.5)	7.3 (6.5)	3.7 (2.7)	0.8	4.6	1.0	2.7
Si <sub>10</sub> H <sub>14</sub> >O	3.4	7.6	4.0	0.1	3.5	1.5	2.5
Si <sub>29</sub> H <sub>34</sub> =O	2.5	6.0	3.7 (3.1)	0.9	4.1	1.2	2.5
Si <sub>29</sub> H <sub>34</sub> >O	2.3	4.8	2.3	0.4	3.0	2.2 (0.3)	0.1

can be observed for the double-bonded Si<sub>29</sub>H<sub>34</sub>O. The O double-bonded case hence seems almost size independent: actually, the presence of this kind of bond creates localized states within the gap that are not affected by quantum confinement as previously predicted by Luppi and Ossicini [22].

Our aim is to allow a direct comparison between experimental data and theoretical results, thus we have calculated not only the transition energies within the  $\Delta$ -SCF approach but also, directly, the absorption and emission optical spectra. Actually, for both the calculated GS and EXC optimized geometry, we have evaluated the optical response  $\text{Im}(\varepsilon_{nc}(\omega))$  (the imaginary part of the nanocrystal dielectric function) through first-principles calculations also beyond the one-particle approach. We have considered the self-energy corrections by means of the GW method and the excitonic effects through the solution of the Bethe–Salpeter (BS) equation. The effect of the local fields (LF) is also included, to take into account the inhomogeneity of the systems. In Table 6, the calculated gaps (as energy differences between LUMO and HOMO) at different levels of approximation are reported for both the Si<sub>10</sub> and Si<sub>29</sub> based nanocrystals. The main result, common to absorption and emission, is the opening of the LDA band-gap with the GW corrections by amounts weakly dependent on the surface termination, but much larger than the corresponding 0.6 eV of the Si bulk case. Looking at the BS-LF calculations, we note a sort of compensation (more evident in the GS than in the EXC) of the self-energy and excitonic contributions:

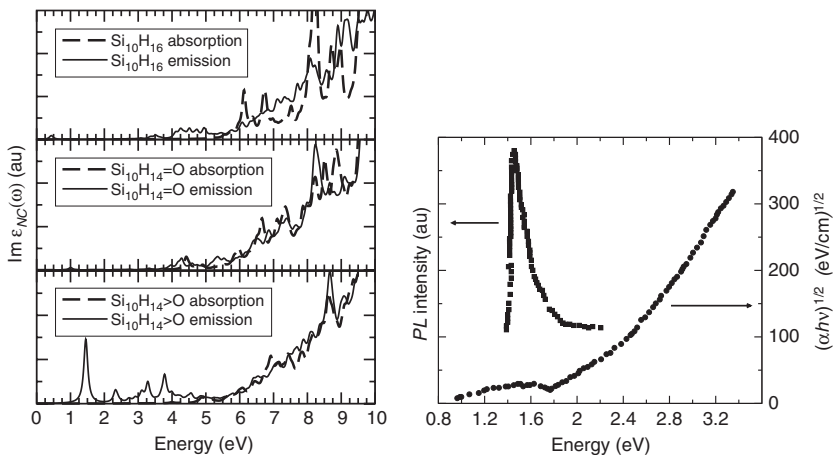


**Figure 9** Emission (solid line) and absorption (dashed line) spectra: imaginary part of the dielectric function for the three considered Si-NCs. On the left:  $\text{Si}_{10}\text{H}_{16}$  (top panel),  $\text{Si}_{10}\text{H}_{14}=\text{O}$  (central panel) and  $\text{Si}_{10}\text{H}_{14}>\text{O}$  (bottom panel). On the right: experimental results for emission (curve on the left) and absorption (on the right) by [96].

the BS-LF values remain similar to the LDA ones. The only exception are the BS-LF calculations for the excited state geometries of the clusters with Si–O–Si bridge bonds at the surface. Concerning the differences between the values of the Stokes shifts calculated through the  $\Delta$ -SCF approach in Table 5 or through the MBPT in Table 6; these are essentially due to the ability or not of the two methods to distinguish dark transitions. In the MBPT the oscillator strengths of each transition are known, while the  $\Delta$ -SCF approach only gives the possibility of finding the energy of the first excitation: if this transition is dark (and the  $\Delta$ -SCF approach does not give this information) the associated energy is not the real optical gap. A clearer insight on the MBPT results is offered by Figure 9 (left panel), where the calculated absorption and emission spectra for all the oxidized  $\text{Si}_{10}$  based clusters are depicted and compared with the fully hydrogenated cluster. Self-energy, local-field and excitonic effects (BS-LF) are fully taken into account.

Concerning the absorption spectra (Figure 9, dashed lines), all three cases show a similar smooth increase in the absorption features. The situation is different for the emission related spectra (Figure 9, solid lines). Here, whereas the situation remain similar for the fully hydrogenated  $\text{Si}_{10}\text{H}_{16}$  (top panel) cluster and for the  $\text{Si}_{10}\text{H}_{14}=\text{O}$  (central panel) cluster, in the case of a Si–O–Si bridge bond (Figure 9 (bottom panel)) an important excitonic peak, separated from the rest of the spectrum, is evident at 1.5 eV. Actually bound excitons are also present in the fully hydrogenated (at 0.4 eV) and in the  $\text{Si}_{10}\text{H}_{14}=\text{O}$  (at 1.0 eV) clusters, nevertheless, the related transitions are almost dark and the emission intensity is very low. Only in the case of

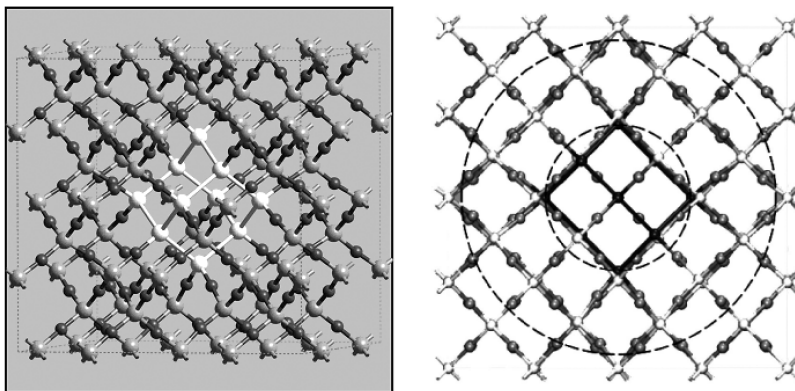


**Figure 10** Stick and ball pictures of the final optimized structure of Si<sub>10</sub> in SiO<sub>2</sub>. The dark gray spheres represent O atoms, light gray Si atoms and white the Si atoms of the nanocrystal.

the Si–O–Si bridge bond does a clear PL peak appear thanks to the strong oscillator strength of the related transition. The right panel of Figure 9 shows the experimental absorption and emission spectra measured by Ma et al. [96] for Si-nanodots embedded in a SiO<sub>2</sub> matrix. A strong PL peak appears around 1.5 eV. Comparison of the experimental spectra with our results suggest that the presence of a Si–O–Si bridge bond at the surface of Si-NCs and the relative deformation localized around the Si–O–Si bond can explain the nature of luminescence in Si nanocrystallites: only in this case the presence of an excitonic peak in the emission related spectra, red-shifted with respect to the absorption onset, provides an explanation for both the observed Stokes shift and the visible PL in Si-NCs. Similar results have been obtained in the case of Si<sub>29</sub>-based clusters. Only in the case of O in the bridge position there is a cage distortion at the interface that allows the presence of significant emission features in the optical region.

### 3.2. Silicon nanocrystals embedded in a SiO<sub>2</sub> matrix

In this section our goal is to build a simple model to study the properties of Si nanocrystals embedded in a SiO<sub>2</sub> matrix from a theoretical point of view [20]. We wanted, at the same time, two fundamental qualities: a Si skeleton with a crystalline behavior for simulating the Si-NC and the simplest Si–SiO<sub>2</sub> interface, with the minimum number of dangling bonds or defects. For these reasons we have started with a cubic cell ( $l = 1.432$  nm) of SiO<sub>2</sub> beta-cristobalite (BC), which is well known as having one of the simplest Si/SiO<sub>2</sub> interfaces because of its diamond-like structure [97]. We get, repeating twice along each cartesian axis, the unit cell of SiO<sub>2</sub> BC. Then we obtained a small cluster by simply deleting some O atoms of the SiO<sub>2</sub> matrix and linking together the Si atoms left with dangling bonds, as shown in Figure 10.

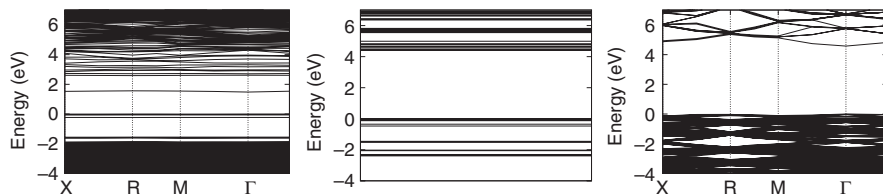


**Figure 11** Band structure along high symmetry points of the BZ for the Si<sub>10</sub> cluster in SiO<sub>2</sub> (left panel) compared with the band structure of beta-cristobalite bulk (right panel) and the energy levels at the  $\Gamma$  point for the isolated Si<sub>10</sub>H<sub>16</sub> cluster (central panel).

In this way we have built an initial supercell of 64 Si and 116 O atoms with 10 Si bonded together to form a small crystalline skeleton ( $T_d$  interstitial symmetry) with a very highly strained bond length with respect to the bulk case: 3.1 Å. We have performed a molecular dynamics simulation through a Car-Parrinello approach to fully relax the system. Electronic and optical calculations have been performed with a 30 Ry energy cutoff. Figure 10 shows the final relaxed supercell structure after the geometry optimization for the Si-NC (Si<sub>10</sub>) in SiO<sub>2</sub>. Looking at the cluster behavior we find that the skeleton is still crystalline-like (diamond) with a Si-Si bond length of 2.67 Å; this means a strain of 14% with respect to the bulk case. This rearrangement causes a complex deformation of the SiO<sub>2</sub> matrix around the cluster, both in bond lengths and angles. Nevertheless the deformation does not affect the whole SiO<sub>2</sub> matrix. Actually it is still possible to find a good BC crystalline structure, in terms of angles and bond length, at a distance from the cluster atoms of 0.8–0.9 nm. This means that the cluster is surrounded by a cap-shell of stressed SiO<sub>2</sub> BC, with a thickness of about 1 nm, which progressively goes towards a pure crystalline BC. We have in summary a three-region picture: (i) a strained Si-NC, (ii) a cap shell, with a thickness of 0.8–0.9 nm, of distorted SiO<sub>2</sub>, and (iii) an unstressed crystalline SiO<sub>2</sub>. These three regions are highlighted in Figure 10 (right panel). Despite the simplicity of the model this picture is in close agreement with what has emerged from energy-filtered transmission electron microscopy (EFTMEM) and x-ray measurements on Si nanocrystals in SiO<sub>2</sub> samples produced by PECVD [98,99], and fairly well with recent theoretical results [100,101].

This view is also supported by the analysis of the electronic properties reported in Figure 11. The calculated  $E_g$  for the cluster in the matrix is 1.48 eV, which must be compared with the value of 4.58 eV for the  $E_g$  of BC SiO<sub>2</sub> (bulk) [102].

The strong reduction is caused by the presence, at the valence and conduction band edges, of confined, flat, states completely related to the Si<sub>10</sub>-SiO<sub>2</sub> interface. Actually neither the isolated, H-passivated cluster (see Figure 11, central panel), nor the pure SiO<sub>2</sub> matrix (see Figure 11, right panel) show these states, whereas deep inside the valence and conduction

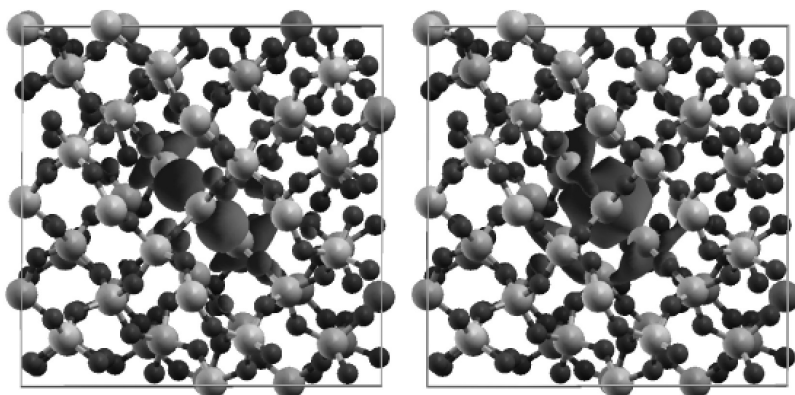


**Figure 12** Isosurfaces at fixed value (10% of max. amplitude) of the square modulus of the highest occupied (HOMO) and lowest unoccupied (LUMO) Kohn–Sham orbitals for the  $\text{Si}_{10}$  cluster in the  $\text{SiO}_2$  matrix.

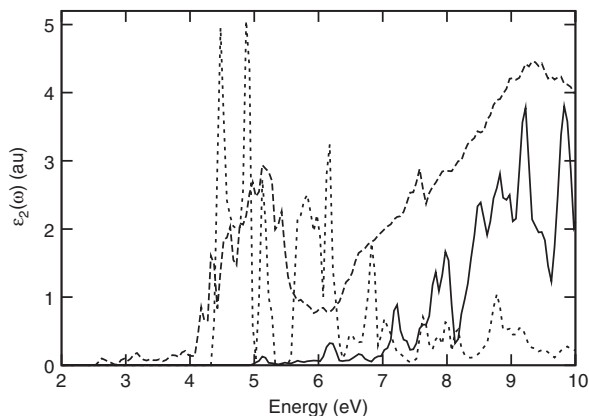


**Figure 13** Imaginary part of the dielectric function for the  $\text{Si}_{10}$  cluster in BC matrix (dashed line) compared with that of an isolated, hydrogenated  $\text{Si}_{10}$  cluster (dotted line) and of the beta-cristobalite bulk (solid line).

bands the more  $k$ -dispersed states related to the  $\text{SiO}_2$  matrix are still present. In Figure 12 the HOMO and LUMO isosurfaces at the fixed value of 10% are reported; we clearly see that the distribution is totally confined in the Si–NC region with some weight on the interface O atoms. These cluster-related states cause strong absorption features in the optical region, as witnessed from Figure 13 where absorption spectra of the isolated  $\text{Si}_{10}$  cluster, of the pure matrix and of the composed system are reported. These features are entirely new, they do not exist for the isolated cluster or for the pure matrix, and so have to be due to the nature of the interface region. The origin of the

PL observed in the red optical region for Si-NC immersed in a SiO<sub>2</sub> matrix can then be found in the properties of this interface. Our result, concerning the role of both Si-NC and the interface Si-O region with respect to the absorption process, is in close agreement with X-ray absorption fine structure measurements [98] that indicate the presence of an intermediate region between the Si-NC and the SiO<sub>2</sub> matrix, about 1 nm thick, that participates in the light emission process.

### 3.3. Doped silicon nanocrystals

In recent years we have performed several theoretical studies that also consider the single and simultaneous doping of Si-NCs with n- and p-type impurities [103–111].

Here we resume our results for single doping, and we report on a comprehensive investigation of the structural, electronic and optical properties of B and P simultaneously doped Si-nanocrystals using ab-initio Density Functional Theory. Our results are obtained in a plane-wave pseudopotential DFT scheme, using the ESPRESSO package [95]. Full relaxation with respect to the atomic positions is performed for all systems. All the DFT calculations are performed within the generalized gradient approximation using Vanderbilt ultrasoft pseudopotentials [112] for both the determination of the structural and electronic properties, and a norm conserving pseudopotential within the LDA at the relaxed geometry to evaluate the optical properties. All the considered Si nanostructures are embedded in large supercells in order to prevent interactions between the periodic replicas. A careful analysis has been performed in order to test the convergence of the structural and electronic properties with respect to both the supercell side and plane-wave basis set cut-off.

#### 3.3.1. Single-doped silicon nanocrystals

Here we consider the effects of the size and shape of Si-NCs on the incorporation of group-III (B and Al), group-IV (C and Ge), and group-V (N and P) impurities. Single-doping has been investigated both in spherical-like and faceted-like Si-NCs [103,113]. The spherical-like Si-NCs are built taking all the bulk Si atoms contained within a sphere of a given radius and terminating the surface dangling bonds with H; whereas faceted Si-NCs result from a shell-by-shell construction procedure which starts from a central atom and adds shells of atoms successively. The spherical-like Si NCs are the Si<sub>29</sub>H<sub>36</sub>, Si<sub>87</sub>H<sub>76</sub>, Si<sub>147</sub>H<sub>100</sub>, and Si<sub>293</sub>H<sub>172</sub> clusters and the faceted Si NCs are the Si<sub>5</sub>H<sub>12</sub>, Si<sub>17</sub>H<sub>36</sub>, Si<sub>41</sub>H<sub>60</sub>, and Si<sub>147</sub>H<sub>148</sub> clusters. The average diameter of doped and undoped Si NCs after relaxation is about 2.3 nm for the largest crystal considered. The substitutional impurity site is one of the Si atoms at the center of the Si-NCs. As for impurities in bulk Si, Jahn-Teller distortions occur in the neighborhood of the impurity sites and the bond lengths show a dependence with respect to the size and shape of the Si-NCs.

After ionic relaxation the Si- $X$  bond lengths ( $X = \text{B}, \text{Al}, \text{C}, \text{Ge}, \text{N}$ , and  $\text{P}$ ) tend to be longer for faceted than for spherical-like Si-NCs. A small variation of the impurity levels with respect to the shape of the Si NCs is observed. Boron and aluminum give rise to shallow acceptor levels, whereas phosphorus gives rise to a shallow donor level and nitrogen to a deep donor level. The energetic positions of the impurity levels become deeper as the size of the Si-NC decreases and tend towards the position of the corresponding impurity levels of Si bulk as the size of the Si-NCs increases. For all the impurities considered the lowest-energy transitions occur at lower energies than the ones in the corresponding undoped Si NCs.

Starting from the  $\text{Si}_n\text{H}_m$  nanocluster [68], the formation energy (FE) for the neutral  $X$  impurity can be defined as the energy needed to insert the  $X$  atom, with chemical potential  $\mu_X$ , into the cluster after removing a Si atom (transferred to the chemical reservoir, assumed to be bulk Si)

$$E_f = E(\text{Si}_{n-1}X\text{H}_m) - E(\text{Si}_n\text{H}_m) + \mu_{\text{Si}} - \mu_X, \quad (20)$$

where  $E$  is the total energy of the system,  $\mu_{\text{Si}}$  the total energy per atom of bulk Si, and  $\mu_X$  the total energy per atom of the impurity. The results show that for smaller Si-NCs a larger energy is needed for the formation of the impurity. There is a slight tendency in formation energy that suggests that the incorporation of the impurities is more favored in spherical than in faceted Si NCs. This tendency is not valid for the neutral Ge and P impurities, which present a formation energy nearly independent of the shape, or by the Al impurity, for which the incorporation is slightly favored for faceted Si NCs. We have also calculated how the FE changes as a function of the impurity position within the Si-NC [103] (see Figure 14). For the B neutral impurity in the large  $\text{Si}_{146}\text{BH}_{100}$  cluster we have moved the impurity from the cluster center toward the surface along different paths still considering substitutional sites. It results that, as far as the internal core is concerned, variations no higher than 0.06 eV are found. On the contrary, an energy drop between 0.25 and 0.35 eV is found as the B impurity is moved to the Si layer just below the surface. This is explained by considering that such positions are the only ones which allow a significant atomic relaxation around the impurity, because in the other cases the surrounding Si cage is quite stable. Thus, as the B atom is moved toward the surface the FE decreases, making the subsurface positions more stable. The situation is different for the P atom.

### 3.3.2. Co-doped silicon nanocrystals

As already said in the introduction, simultaneous doping with  $n$ - and  $p$ -type impurities represents a way to overcome the low radiative recombination efficiency in our systems, so, starting from the already described hydrogenated Si-NCs, and following the work of Fujii et al. [32–34], we have

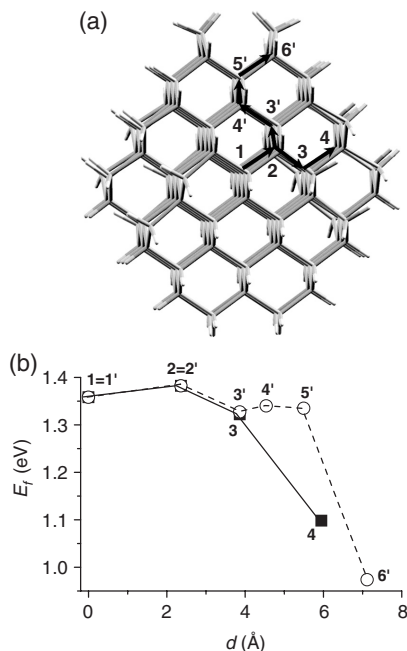


**Figure 14** Formation energies for neutral impurities as a function of the impurity position within the cluster (b). The impurity is moved along two different paths toward the surface, as shown in (a). The lines are a guide for the eyes.

doped the Si clusters by locating the B and P impurities in substitutional positions just below the nanocrystal surface. It is worth mentioning that this arrangement represents the most stable configuration, as confirmed in the previous section and by theoretical and experimental works [103,114,115]. Full relaxation with respect to the atomic positions has been allowed and electronic properties have been computed through DFT calculations.

Here we will present, as an example, all the results relative to the Si<sub>33</sub>BPH<sub>36</sub> nanocrystal, whose relaxed structure is presented in Figure 15. The choice of the small Si<sub>33</sub>BPH<sub>36</sub> cluster (diameter around 1 nm) is due to the fact that the GW-BSE calculation [116], necessary to obtain the many-body optical spectra, is very computationally demanding.

First of all, it is interesting to look at the changes in the structural properties induced by the presence of the impurities, comparing the B and P codoped cases with the single-doped ones.

Table 7 gives the optimized bond lengths around the impurities for the Si<sub>35</sub>H<sub>36</sub> nanocrystal. Comparing these bond lengths with those of the corresponding Si atoms in the pure Si-NC it is clear that some significant relaxation occurs around the impurities. The amount of the relaxation around the impurity is directly related to the impurity valence, actually a

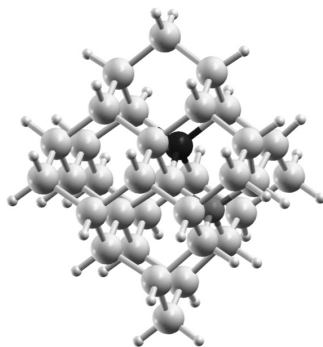


**Figure 15** Relaxed structure of the  $\text{Si}_{33}\text{BPH}_{36}$  co-doped nanocrystal (diameter = 1.10 nm). Gray balls represent Si atoms, while the light gray balls are the H used to saturate the dangling bonds. B (dark gray) and P (black) impurities have been located at subsurface positions in substitutional sites on opposite sides of the nanocrystals. The relaxed impurity distance is  $\text{DBP} = 3.64 \text{ \AA}$ .

**Table 7** Bond lengths around the impurity site for the un-doped  $\text{Si}_{35}\text{H}_{36}$  cluster and the single- and co-doped ones. P and B impurities have been substitutionally located at sub-surface positions (see Figure 15).  $\text{Si}_s$  and  $\text{Si}_i$  refer to surface and inner Si atoms around this site respectively

Bond	$\text{Si}_{35}\text{H}_{36}$ (\AA)	Bond	$\text{Si}_{34}\text{PH}_{36}$ (\AA)	$\text{Si}_{34}\text{BH}_{36}$ (\AA)	$\text{Si}_{33}\text{BPH}_{36}$ (\AA)
Si–Si <sub>s</sub>	2.300	P–Si <sub>s</sub>	2.366		2.035
Si–Si <sub>s</sub>	2.300	P–Si <sub>s</sub>	2.365		2.026
Si–Si <sub>s</sub>	2.300	P–Si <sub>s</sub>	2.364		2.026
Si–Si <sub>i</sub>	2.361	P–Si <sub>i</sub>	2.310		2.007
Si–Si <sub>s</sub>	2.300	B–Si <sub>s</sub>		2.093	2.303
Si–Si <sub>s</sub>	2.300	B–Si <sub>s</sub>		2.022	2.302
Si–Si <sub>s</sub>	2.300	B–Si <sub>s</sub>		2.022	2.297
Si–Si <sub>i</sub>	2.361	B–Si <sub>i</sub>		2.008	2.334

more significant distortion is found for the trivalent atom (B) than for the pentavalent one (P). In addition, it is interesting to note that in the co-doped case the differences among the four impurity-Si bond lengths are always smaller with respect to the single-doped case. Thus, if carriers in the Si-NCs are perfectly compensated by simultaneous *n*- and *p*-type impurity doping, an almost  $T_d$  configuration is recovered in which the four impurity-Si bonds are practically the same.

This tendency towards a  $T_d$  configuration in the comparison between single- and co-doped Si-NCs is found for all the considered nanocrystals, showing that these outcomes are independent of the size of the Si-NCs.

The structural deformation occurring in the single and co-doped nanocrystals has a profound influence on the stability of the systems studied.

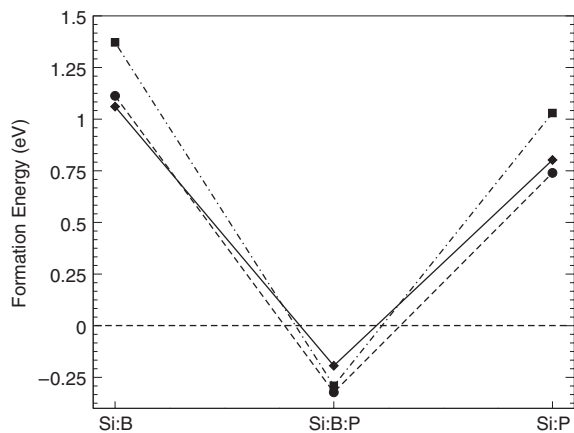


**Figure 16** Formation energy for single-doped and co-doped Si-NCs. In the co-doped nanocrystals, the impurities are placed as second neighbors in the first subsurface shell. Squares are related to  $\text{Si}_{35}\text{H}_{36}$ , diamonds to  $\text{Si}_{87}\text{H}_{76}$ , and circles to  $\text{Si}_{147}\text{H}_{100}$  based nanocrystals. The lines are a guide for the eyes.

Here we investigate the stability of the nanocrystals through the calculation of the formation energy. As stated in the previous section, starting from the  $\text{Si}_n\text{H}_m$ -NCs [68], the formation energy of the neutral B or/and P impurities can be defined as the energy needed to insert one B and/or one P atom within the cluster after removing one/two Si atoms (transferred to the chemical reservoir, assumed to be bulk Si). Thus generalizing the equation of the previous section we have:

$$E_f = E(\text{Si}_{n-l-k}\text{B}_k\text{P}_l\text{H}_m) - E(\text{Si}_n\text{H}_m) + (k+l)\mu_{\text{Si}} - k\mu_{\text{B}} - l\mu_{\text{P}}, \quad (21)$$

where  $E$  is the total energy of the system,  $\mu_{\text{Si}}$  the total energy per atom of bulk Si and  $\mu_{\text{B(P)}}$  the total energy per atom of the impurity.  $k$  and  $l$  can be 0 or 1, thus one has un-doped, single B- or P-doped Si-NCs or B and P co-doped Si-NCs.

In Figure 16 we report the calculated formation energies related to  $\text{Si}_{35}\text{H}_{36}$  (diameter  $d = 1.10$  nm),  $\text{Si}_{87}\text{H}_{76}$  ( $d = 1.50$  nm) and  $\text{Si}_{147}\text{H}_{100}$  ( $d = 1.79$  nm) nanocrystals. In the figure, we compare the formation energy required to have B or P single-doped nanocrystals with that calculated for the case of B and P co-doped nanocrystals. In particular, in this figure, we study the case in which the B and P impurities have been placed as second neighbors in the nanocrystals (considering only sub-surface positions, this case corresponds to the nearest possible distance between the two impurities). After geometry optimization the distances between B and P impurities are  $D_{\text{BP}} = 3.56$  Å,  $D_{\text{BP}} = 3.64$  Å and  $D_{\text{BP}} = 3.68$  Å for the  $\text{Si}_{35}\text{H}_{36}$ ,  $\text{Si}_{87}\text{H}_{76}$  and  $\text{Si}_{147}\text{H}_{100}$  nanocrystals, respectively.

From Figure 16 it is clear that simultaneous B and P doping strongly reduces (by about 1 eV) the formation energy with respect to both B or P single-doped cases and that this reduction is similar for Si-NCs of different size. While B or P single doping is very costly (in particular, the formation energy increases with decreasing nanocrystal size, in agreement with previous calculations [103,117]) B and P co-doping is much easier and there is almost no dependence on the nanocrystal size. The important point here is that Si-NCs can be more easily simultaneously doped than single-doped; this is due to both the charge compensation and the minor structural deformation.

Concerning the electronic properties, in the single-doped cases we have already shown that the presence of donor or acceptor states can considerably lower the energy gap  $E_G$  of the un-doped Si-NCs [103,104]. Actually, for single-doped Si-NCs, the HOMO level now contains only one electron and is strongly localized either on the B or P impurity. For example, in the case of the  $\text{Si}_{86}\text{BH}_{76}$  single-doped nanocrystal the defect level is located just 0.28 eV above the valence band, thus the energy gap is reduced from 2.59 eV (the value for the un-doped nc) to 2.31 eV, whereas for the  $\text{Si}_{86}\text{PH}_{76}$  single-doped nanocrystal the defect level is located just 0.28 eV below the conduction band, and the energy gap is thus now only 0.28 eV [104]. It is interesting to note that the experimental substitutional donor binding energy for P in Si bulk is about 33 meV, while the experimental acceptor energy for B in Si is 45 meV [118], showing how, in the case of nanocrystals, the quantum confinement effect tends to “transform” shallow impurities into “deep” centers.

Now, what is important is that the electronic properties of B- and P- co-doped Si-NCs are qualitatively and quantitatively different from those of either B- or P- single-doped Si-NCs. The presence of both a  $n$  and a  $p$  impurity leads to a HOMO level that contains two electrons and to a HOMO-LUMO gap that is strongly lowered with respect to that of the corresponding un-doped nanocrystals.

The calculated energy levels for the  $\text{Si}_{35}\text{H}_{36}$  related systems at the  $\Gamma$  point, calculated at the optimized geometries, are shown in Figure 17, where only the levels corresponding to the HOMO, LUMO, HOMO-1 and LUMO+1 states are depicted. Calculated square modulus contour plots related to HOMO and LUMO states show their localization within the Si-NC, in particular the HOMO state is localized on the B impurity while the LUMO is localized on the P one. The presence of these donor and acceptor states lowers the energy gap from 3.51 eV, for the pure cluster, to 2.86 eV, for the doped one. In principle, starting with a bigger cluster, for which the energy gap is smaller than in this case, it is possible through co-doping also to tune the gap below the bulk Si value, as experimentally observed by Fuji and coworkers [33]. In order to give a complete description, within the many-body framework, of the co-doped Si-NC response to an optical excitation, we consider both the self-energy corrections, by means of the GW method to obtain the quasiparticle energies, and the excitonic effects, through the

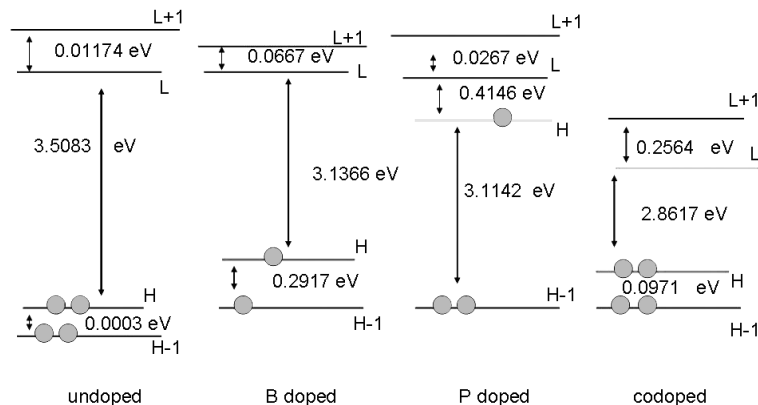


**Figure 17** Calculated energy levels at the  $\Gamma$  point for the  $\text{Si}_{35}\text{H}_{36}\text{-nc}$  family. From left to right: un-doped  $\text{Si}_{35}\text{H}_{36}\text{-nc}$ , single-doped  $\text{Si}_{34}\text{BH}_{36}\text{-nc}$ , single-doped  $\text{Si}_{34}\text{PH}_{36}\text{-nc}$ , co-doped  $\text{Si}_{33}\text{BPH}_{36}\text{-nc}$ . Alignment has been performed by locating, at the same energy, the fully occupied levels with the same type of localization.

solution of the Bethe-Salpeter equation. The effect of local fields is also included, to take into account the inhomogeneity of the systems.

To carry out emission spectra calculations, we have used the excited state geometry and the ground state electronic configuration, as already described in Section 2.1.1. Thus, here, the electron-hole interaction is also considered in the emission geometry. Figure 18 (right panel) shows the calculated absorption and emission spectra fully including the many-body effects. The electron-hole interaction yields significant variations with respect to the single-particle spectra (shown in the left panel), with an important transfer of the oscillator strength to the low energy side. Moreover, in the emission spectrum, the rich structure of states characterized, in the low energy side, by the presence of excitons with largely different oscillator strengths, determines excitonic gaps well below the onset of optical absorption. Thus the calculated emission spectrum results are red-shifted to lower energy with respect to the absorption ones. This energy difference between emission and absorption, the Stokes shift, can be traced back to the relaxation of the Si-NCs after the excitation process. The new and important features that appear in the emission many-body spectra are related to the presence of both B and P impurities, as shown by Figure 19, which gives the real-space probability distribution  $|\psi_{\text{exc}}(r_e, r_h)|^2$  for the bound exciton as a function of the electron position  $r_e$  when the hole is fixed in a given  $r_h$  position. In this case the hole is fixed on the boron atom and we see that the bound exciton is mainly localized around the phosphorus atom. From Table 8, it can be seen that the single-particle DFT results strongly underestimate the absorption and emission edge with respect to the GW+BSE calculation, in which the excitonic effect are taken exactly into account. This means that, in this case, the cancellation between

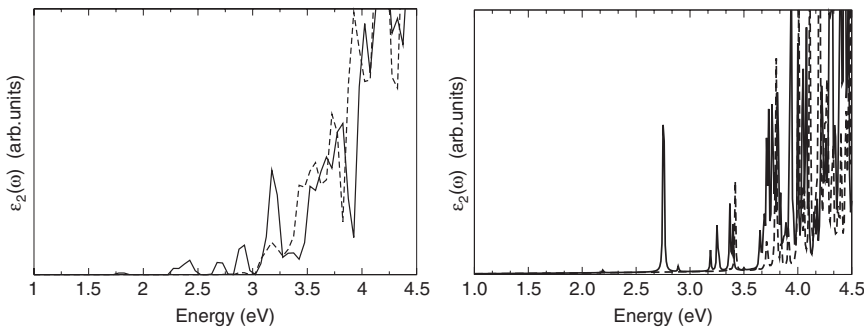


**Figure 18** Left panel: Single-particle imaginary part of the dielectric function for the co-doped  $\text{Si}_{33}\text{BPH}_{36}$  nanocrystal in the ground (dashed line) and excited (solid line) geometries. Right panel: absorption (dashed line) and emission (solid line) many-body spectra of  $\text{Si}_{33}\text{BPH}_{36}$ .

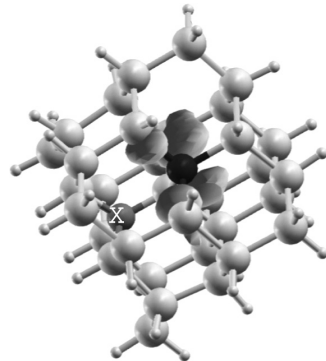


**Figure 19** Excitonic wave function of  $\text{Si}_{33}\text{BPH}_{36}$  (atom colors as in Figure 15). The gray isosurface represents the probability distribution of the electron, with the hole fixed (cross) on the B impurity.

GW gap opening (which gives the electronic gap) and BSE gap shrinking (which gives the excitonic gap) is only partial. The difference between the GW electronic gap and the GW+BSE optical excitonic gap gives the exciton binding energy  $E_b$ . We note the presence of exciton binding energies of 2.2 eV, which are very large if compared with bulk Si ( $\sim 15$  meV) or with carbon nanotubes [119,120] where  $E_b \sim 1$  eV, but similar to those calculated for undoped Si-NC [92] of similar size and for Si and Ge small nanowires [121,122].

It is interesting to note that the HOMO–LUMO transition in the emission spectrum at 2.20 eV is almost dark while an important excitonic peak is evident at about 2.75 eV (see Figure 18), red-shifted with respect to the first absorption peak.

**Table 8** Absorption and Emission gaps calculated as the HOMO–LUMO difference through a DFT and a GW+BSE approach

Si <sub>33</sub> BPH <sub>36</sub>	DFT	GW	GW + BSE
Abs. (eV)	2.80	5.52	3.35
Ems. (eV)	1.71	4.37	2.20

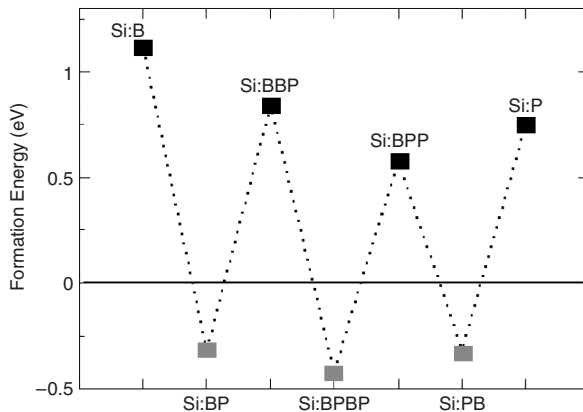


**Figure 20** Formation energies for single, co-doped and multi-doped Si<sub>147</sub>H<sub>100</sub> based nanocrystals. The lines are a guide for the eyes.

### 3.3.3. Multi-doped silicon nanocrystals

Here we present how the formation energy and the electronic properties of the Si-NCs are influenced by the insertion of a large number of impurities. We call this insertion of several impurities multi-doping. In Figure 20 we show how the FE of a large Si<sub>147</sub>H<sub>100</sub>-NC varies as a function of the number of impurities. We note that the presence of an odd number of dopants (1 or 3) already brings the FE to higher values. In contrast, the presence of an even, compensated number of B and P impurities strongly lowers the FE, which drop down to a negative value, indicating that as in the case of simple co-doping, multi-doping is much easier to realize when one has the same number of donor and acceptor dopant atoms. In fact the Si<sub>145</sub>BPH<sub>100</sub>-NC, Si<sub>143</sub>BBPPH<sub>100</sub>-NC and Si<sub>141</sub>BBBPPPH<sub>100</sub>-NC (not shown in the figure) show an FE of -0.32 eV, -0.42 eV and -0.97 eV respectively.

Next we investigate how the electronic levels are influenced by adding one or two more impurities to the already co-doped Si<sub>145</sub>BPH<sub>100</sub>-NC. We consider the Si<sub>145</sub>BPH<sub>100</sub>-NC, where the starting B and P pair is located in a particular site, which is the more stable configuration. Therefore we first add one single impurity in order to obtain either the Si<sub>144</sub>BBPH<sub>100</sub>-NC (with an excess of B: 2 B atoms and 1 P) or the Si<sub>144</sub>BPPH<sub>100</sub>-NC (with an excess of

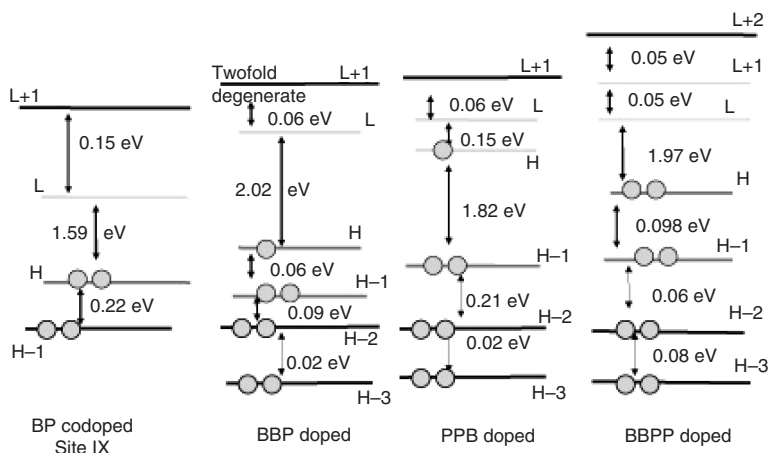


**Figure 21** Calculated energy levels at the  $\Gamma$  point for the  $\text{Si}_{145}\text{BPH}_{100}$ -NC, the  $\text{Si}_{144}\text{BBP}_{100}$ -NC, the  $\text{Si}_{144}\text{BPPH}_{100}$ -NC and the  $\text{Si}_{143}\text{BBPPH}_{100}$ -NC. Alignment has been performed by locating, at the same energy, the fully occupied levels with the same type of localization.

P: 1 B and 2 P) and finally, adding simultaneously two B and two P atoms, we obtain the  $\text{Si}_{143}\text{BBPPH}_{100}$ -NC.

Looking at the electronic structure in Figure 21, the two Si-NCs with 3 impurities, presents a similar behavior to those corresponding to B or P single-doped Si-NC ( $\text{Si}_{146}\text{BH}_{100}$  or  $\text{Si}_{146}\text{PH}_{100}$ ). Every new dopant inserted gives rise to a new impurity level, which is half occupied. Looking at the figure we see that the HOMO-LUMO energy differences for the nanoclusters with an odd number of impurity atoms are very similar: 2.02 eV for the  $\text{Si}_{144}\text{BBP}_{100}$ -NC with respect to 2.08 eV for the B single doped case ( $\text{Si}_{146}\text{BH}_{100}$ ), and 0.15 eV for the  $\text{Si}_{144}\text{BPPH}_{100}$ -NC with respect to 0.13 eV for the P single doped case ( $\text{Si}_{146}\text{PH}_{100}$ ) respectively. In addition, when the impurities are compensated, as in the case of  $\text{Si}_{143}\text{BBPPH}_{100}$ -NC, the system becomes a semiconductor, in which the HOMO again contains two electrons, and the value of the energy gap (1.97 eV) is intermediate with respect to the two corresponding extrema  $E_G$  of the co-doped  $\text{Si}_{145}\text{BPH}_{100}$  with impurities located at different distances (2.03 eV for impurities closer to each other and 1.59 eV for impurities at the opposite side of the Si-NC).

The single-particle absorption spectra reflects the results for the electronic properties. As far as all the compensated co-doped Si-NCs are concerned we observe a shift of the absorption onset toward lower energy on increasing the distance between the impurities. It is worth pointing out that when impurities are at large distance the transition intensities near the band edges become weaker due to small oscillator strengths. On the other hand when the impurities are close to each other, the transitions near the band edge are

more intense, due to the strong localization of HOMO and LUMO on the impurity sites.

### 3.3.4. Screening in silicon nanostructures

The presence in the cluster of a positively charged impurity has also been considered, analyzing, by first principles, the screening due to the Si-NCs [123,124]. A reduction of screening in Si nanostructures with respect to bulk Si has been already observed [52] and predicted [125]. This reduction is a fundamental process at the basis of the enhancement of both the electron–hole interaction and the impurity activation energies in nanosized objects, and is due to the fact that close to the surface there is a dielectric dead layer, with a finite-range reduction of the dielectric constant due to the dielectric mismatch at the nanocrystal-environment interface.

Starting from the optimized configuration of hydrogenated nanocrystals (described in Section 3.1.1), the self-consistent electronic response to an impurity atom has been studied. The screening has been studied introducing a substitutional phosphorous ion ( $P^+$ ) at the nanocrystal center. The electron density induced by the impurity, into a nanocrystal with  $n$  Si and  $m$  H atoms, is calculated as [123,124]

$$n_{\text{ind}} = n[Si_{n-1}PH_m^+] - n[Si_nH_m], \quad (22)$$

where  $n$  is the real-space ground state electron density. We have calculated the spherical average of the induced density for several nanocrystals, as a function of size, and present our results in Figure 22(a). We have also calculated their integrals, namely the integrated induced densities, reported in Figure 22(b). Arrows indicate the nanocrystal radii. A close examination of Figure 22 shows an electron density depletion (i.e., a positive charge accumulation) localized at the nanocrystal surface, in such a way as to fully compensate the electron density accumulation (negative charge) around the impurity. The surface charge accumulation is exactly centered around the nanocrystal radii, as we could have supposed at the beginning. However, an interesting fact is that, as revealed in the figure, the charge is much spread around the radii, and we estimate 0.2–0.3 nm of a surface polarization layer. This depletion region is at the origin of the dielectric constant reduction with respect to the bulk system, recently reported in literature [125]. Figure 22(a) and (b) show that the real space electron response rapidly reaches the bulk limit and the curves for different sizes match each other a few Å apart from the surface. We thus argue, that far from the surface we have a bulk-like response driven by the Si static dielectric constant, while at the surface there is a dielectric dead layer, with the dielectric constant smoothly reducing to the external value of one. Moreover the surface polarization layer width is almost size-independent; the behavior around the surface of the different curves in Figure 22(b), with the reduction of the integrated electron density,

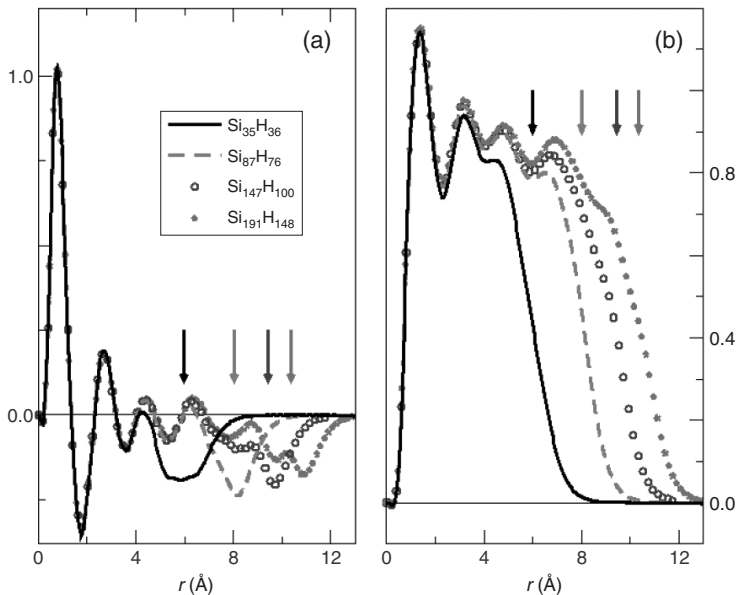


**Figure 22** Spherical averaged induced density (panel (a)) and integrated induced density (panel (b)) calculated for  $P^+$  impurities in Si nanocrystals with increasing size. The arrows point to the nanocrystal radii.

is almost the same for all the nanocrystals. The oscillating behavior in the intermediate region between the impurity location and the surface is a consequence of the polarization of the Si–Si bonds within the nanocrystal. This is a local field effect also visible in bulk Si, but it gives a minor contribution to the static dielectric constant.

As it is known from the literature, the integrated induced density of the local field oscillating behavior, tends to a constant value  $Q$  resulting from the incomplete screening of Si [126].  $Q$  is calculated from the static dielectric constant  $\epsilon_s$ :

$$Q = 1 - \frac{1}{\epsilon_s} \quad (23)$$

It is almost impossible to derive the exact value of  $Q$  from Figure 22(b), because of the large oscillations discussed above. However, since the induced charge rapidly converges in the region far from the surface, we can reasonably assume that the reduction of  $Q$  (and thus of the screening) is limited to the region of space around the surface.

From this analysis, it is worth underlining that the surface plays the leading role in the screening. It is meaningless to neglect the surface in a calculation involving either an impurity or an excitonic screening. In spherical

nanocrystals all the details of the electronic response, both due to the bulk-like local field contributions and a non negligible dielectric dead layer width, are fully covered by the macroscopic, primary surface polarization charge contribution. For such a reason, we have applied the Thomas–Fermi model for semiconductors proposed by Resta [126] in 1977 to the screening in nanocrystals (the substantial difference between a bulk structure and a nanocrystal consists in the nanocrystal surface). The Thomas–Fermi model, actually, only considers the charge accumulation around the impurity and at the surface, and then gives an excellent agreement with very accurate first-principles calculations. Details of the model are the following; let us consider a positive point charge +1 (atomic units are used) located at the center of a spherical nanocrystal. Because of the incomplete screening, the total induced charge near the impurity amounts to  $-Q$ . This charge is fully compensated by an amount of charge  $+Q$  located at the nanocrystal surface. Thus, outside the screening sphere, the potential is that of a point charge  $(1 - Q)$  located at the nanocrystal center plus the contribution from the surface charge. From simple electrostatics it can be shown that the potential energy for an electron is

$$V_c(r) = \begin{cases} -\left(\frac{1-Q}{r}\right) - \left(\frac{Q}{R}\right) & R_s < r \leq R \\ -\frac{1}{r} & r \geq R. \end{cases} \quad (24)$$

where  $R$  is the nanocrystal radius. The screened potential inside  $R_s$  can be computed within the Thomas–Fermi theory. According to this [126], the potential energy  $V(r)$  solves, for  $r < R_s$ , the linearized equation

$$\nabla^2 V(r) = q^2[V(r) - \mu]. \quad (25)$$

Here,  $q$  is the inverse of a screening length related to the valence electron density which contributes to the screening and  $\mu$  is a Lagrange multiplier controlling the total number of particles. The boundary conditions to be used with Equation (23) are that  $V(r)$  must match  $V_c(r)$  at  $R_s$  and that  $rV(r) \rightarrow -1$  as  $r \rightarrow 0$ . Once we have solved the Thomas–Fermi equation, we have calculated the screened function, defined as the bare impurity potential divided to the screened one, namely  $V_b/V$ .

We report here the final expression for the screening function:

$$\bar{\epsilon}(r) = \begin{cases} \left\{ \frac{1-Q}{qR_s} [\sinh[q(R_s - r)] + qr] + \frac{Qr}{R} \right\}^{-1} & 0 \leq r \leq R_s \\ \left[ 1 - Q + \frac{Qr}{R} \right]^{-1} & R_s \leq r \leq R \\ 1 & r \geq R. \end{cases} \quad (26)$$

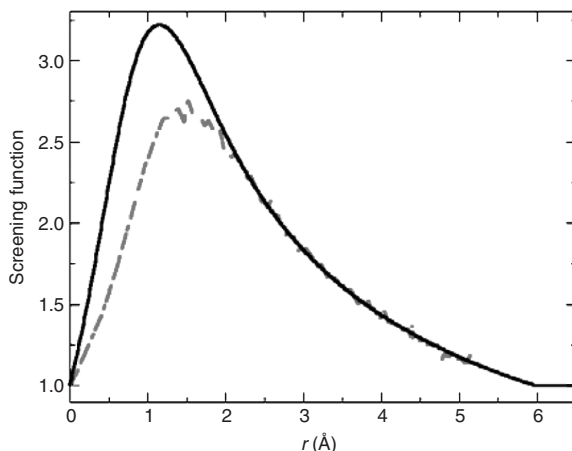


**Figure 23** Screening function calculated for the  $\text{Si}_{35}\text{H}_{36}$  nanocrystal, using the Thomas–Fermi model (solid line), compared to a previous first principles calculation [127] (dashed line).

The parameters here used are the ones first given by Resta;  $q = 1.10$  au,  $R_s = 4.28$  au, and  $Q = 0.912$ . It is very important to remark that the expression given here for the screening function is analytical and universal and can be applied to every spherical semiconductor nanocrystal. We show in Figure 23 the screening function calculated for  $\text{Si}_{35}\text{H}_{36}$  using the present model, compared to a previous first principles calculation, based on the density functional linear response theory [127]. The novelty of the present model is that the screening function has the correct limit of one, both at the impurity location and at the nanocrystal surface. The agreement is very nice, especially in the region of space around the surface, where the screening is governed by the classical contribution. Once again, we underline the great importance of surface polarization charge, as that alone can give a good agreement with state-of-art calculations.

## 4. ONE-DIMENSIONAL SYSTEMS

### 4.1. Silicon and germanium nanowires

In recent years much effort has been spent on the development of experimental techniques to grow well defined nanoscale materials, due to their possible applications in nanometric electronic devices. Indeed the creation of nanowire field effect transistors [128–132], nano-sensors [133,134], atomic scale light emitting diodes and lasers [135,136], has been made possible by the development of new techniques, which allow one to control the growth processes of nanotubes, nanowires and quantum dots. Of particular importance, among the different atomic scale systems experimentally studied, are

nanowires. Being quasi-one-dimensional structures, they exhibit quantum confinement effects such that carriers are free to move only along the axis of the wire. Further, the possibility to modify their optical response as a function of their size has become one of the most challenging aspect of recent semiconductor research. Because of their natural compatibility with Si based technologies, Si nanowires (Si-NWs) have been extensively studied and several experiments have already characterized some of their structural and electronic properties [38,129,133,137–139]. Recently it has been possible to fabricate, for example, single-crystal Si-NWs with diameters as small as 1 nm and lengths of a few tens of micrometers [37,133,140,141]. PL [3,142,143] data revealed a substantial blue-shift with decreasing size of nanowires. Further scanning-tunnelling spectroscopy data [37,143] also showed a significant increase in the electronic energy gap for very thin semiconductor nanowires, explicitly demonstrating quantum-size effects. Germanium nanowires (Ge-NWs), which can be synthesized using a variety of techniques [38,137,144], are particularly interesting due to their high carrier mobility: in fact, Ge-NWs based-devices such as field effect transistors [145], solar cells and nanomagnets [146], have been characterized or envisaged [147]. Recently it has also been shown that Ge-NWs could be used in optoelectronic components fabricated within Si based technology [148]. Despite such clear device potential, relatively few ab-initio calculations of optical properties beyond the one-particle approach have so far been performed [121,122,149,150] in order to clarify the experimental evidence and investigate the potential applications of such nanoscale materials. In fact the theoretical panorama is essentially based either on ab-initio calculations [151–158] which neglect the electron–hole Coulomb interaction effects (which instead is expected to play an important role due to the reduced dimensionality of such systems) or on Effective Mass Approximation (EMA) calculations [159] and semi-empirical approaches [160,161].

In this section we will describe the electronic properties of H passivated, free standing Si and Ge nanowires oriented along the [100], [111] and [110] directions, with diameters ranging from about 0.4 to 1.2 nm. The effective width is defined as the wire cross-section linear parameter, following the definition of Ref. [154]. Nevertheless it must be underlined that this definition of the wire size is somewhat ambiguous, indeed in literature larger diameters are reported for wires with the same number of atoms in the unit cell than the ones studied here. This is due to the fact that different definitions of the wire radius exist [161] and that in some cases the average distance among the external H atoms is taken into account.

In particular we will show the dependence of the electronic gap on both wire size and orientation. Further, in some of the studied wires, self-energy corrections, by means of the GW method, and also electron–hole interaction, by solving the Bethe–Salpeter equation, will be included in order to have an appropriate description of the excited states.

**Table 9** DFT–LDA electronic gaps in Ge-NWs and Si-NWs are reported respectively in the third and fifth column, quasi-particle gaps are reported for Ge-NWs in the fourth column. All values are in eV

Wire size (nm)	Wire orient.	Ge $E_g^{\text{DFT}}$	Ge $E_g^{\text{GW}}$	Si $E_g^{\text{DFT}}$
0.4	[100]	3.9	6.1	3.8
	[111]	3.5	5.4	3.5
	[110]	2.1	4.5	2.7
0.8	[100]	2.6	4.0	2.5
	[111]	2.1		2.2
	[110]	1.3		1.2
1.2	[100]	1.9	3.3	1.8
	[111]	1.6		1.2
	[110]	0.9		1.3

Concerning the electronic minimum gap (which is direct or quasi-direct in all the studied wires, see Ref. [121,122,149,154] for details) at the DFT level (see Table 9) we find that it decreases monotonically with the wire diameter. The calculated values are larger than the electronic bulk indirect gap, thus reflecting the quantum confinement effect. This effect, which has been recently confirmed in STM experiments [37,143], is related to the fact that carriers are confined in two directions, being free to move only along the axis of the quantum wires. Clearly we expect that, increasing the diameter of the wire, such an effect becomes less relevant and the electronic gap will eventually approach the bulk value.

Another aspect that is interesting to note concerns the dependence of the DFT gap on the orientation of the wire, indeed, for each wire size the following relation holds:  $E_g[100] > E_g[111] > E_g[110]$ . As has been pointed out in Ref. [121], this is related to the different geometrical structure of the wires in the [100], [111] and [110] directions. Indeed the [100], [111] wires appear as a collection of small clusters connected along the axis, while the [110] wires resemble a linear chain. So we expect that quantum confinement effects are much bigger in the [100], [111] wires, due to their quasi zero-dimensionality, with respect to the [110] wires. Further, the orientation anisotropy reduces with the wire width and it is expected to disappear for very large wires, where the band gap approaches that of the bulk material.

Most of the results presented in Table 9 do not take into account self-energy corrections, which are necessary in order to describe, in a proper way, the one-particle excited states. In the fourth column of Table 9 we report the GW corrected band-gaps, for the smallest Ge-NWs in the [111],[110] directions, and for all the [100] Ge-NW. A complete discussion on this part can be found elsewhere [121]. We can see (Table 9, fifth column) that the effect of the GW correction is an opening of the DFT–LDA gap, by an amount which

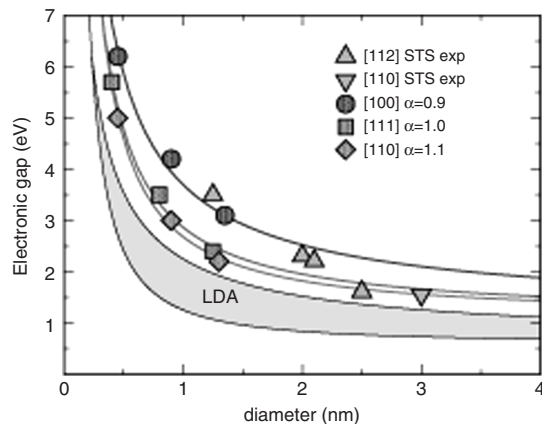


**Figure 24** Scaling of the electronic gap ( $G_W$ ) in [100] (circles), [111] (squares) and [110] (diamonds) oriented Si-NWs as a function of wire size. The results of the STS measurements performed on Si-NWs along the [112] and [110] directions are also presented (see Ref. [37]).

is much bigger than the corresponding correction in the bulk. Furthermore it has to be noted that such corrections are also size and orientation dependent.

Concerning Si-NW, Figure 24 shows the comparison of the calculated quasi-particle electronic gaps with the experimental data obtained by Ma et al. through STM, for different Si-NWs (grown along the [112] and [110] directions), with diameters ranging from 1.3 to 7 nm [37]. We see that all the experimental gaps fall within our [100] and [110] fitting curves, which represent the two limiting cases in terms of quantum confinement effects [122], showing a good agreement with our theoretical results. This confirms that, in order to compare experimental and theoretical results for the electronic band gap, it is mandatory to include the self-energy effects in the calculations. In Figure 25, for all the different Si-NWs, we report our calculated excitonic gap (corresponding to the lowest-energy allowed transition, calculated taking into account the electron–hole interaction) together with the experimental optical data of Zhang and Bayliss [162] and Wolkin et al. [18] for Si nanostructures passivated by H. All the experimental data fall within our theoretical results, moreover we note that the data of Zhang and Bayliss [162], referring to porous Si wires prepared by electrochemical anodization of (100) Si wafers, are in very good agreement with our results relating to [100] oriented Si-NWs. This shows that for the optical spectra it is necessary to take fully into account both the self-energy correction and electron–hole interaction. To underline the importance of the many-body effects on the optical response of the studied nanowires, we report in Figure 26 the theoretical optical absorption spectra of the Ge and Si wires (grown along the [100] direction and with diameter of about 0.8 nm), for light polarized along the

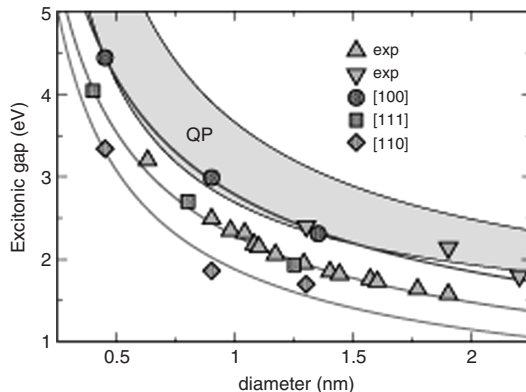


**Figure 25** Calculated (full circles) lowest allowed excitonic gaps for the different Si-NWs and their comparison with the experiments. Down triangles correspond to the data of Zhang and Bayliss [162], whereas up triangles correspond to the data of Wolkin et al. [18].

wire axis. In the top panels, the spectra calculated at the RPA one-particle level, but including self-energy corrections, are shown; while, in the bottom panels, the corresponding spectra obtained including the excitonic effects, are reported. Comparing the top and bottom panels, it is clear that strongly bound excitons, of more than 1 eV, are present. Moreover we aim to underline an important difference between Si and Ge wires: in fact, already at the GW level (top panels) a large oscillator strength near the onset of optical absorption is found only in the case of Ge and not in the case of Si. With the inclusion of the excitonic effects (bottom panels), we see that an important transfer of the oscillator strength below the electronic gap appears and a strong optical peak comes out in the visible range for the 0.8 nm Ge-NW, but not for the 0.8 nm Si-NW (see Figure 26). A similar finding has been obtained by comparing the optical spectra of Si and Ge nanodots [163]. This has been explained as due to the fact that in Si-NW the minimum gap remains indirect in character, as far as the optical matrix elements are considered [122,149], while in the case of Ge-NWs the first conduction band retains a clear  $\Gamma$  character. We underline that this excitonic peak is expected to move to lower energies with increasing wire diameter, thus fully covering the visible range.

A last important effect of quantum confinement is that related to the exciton localization in confined structures. In the case of a wire, the presence of bulges and kinks results in a stronger intensity, larger binding energy and reduced spatial size for the exciton: the size  $L$  of the electron-hole probability distribution depends on the orientation growth in the relation:  $L[100] < L[111] < L[110]$  (see Figure 27). In particular, we find the strongest overlap of the electron-hole wave function (see bottom part of Figure 27) and an excitonic binding energy close to 2 eV in the [100] Ge-NW (of width 0.4 nm). This value is particularly significant when compared with typical

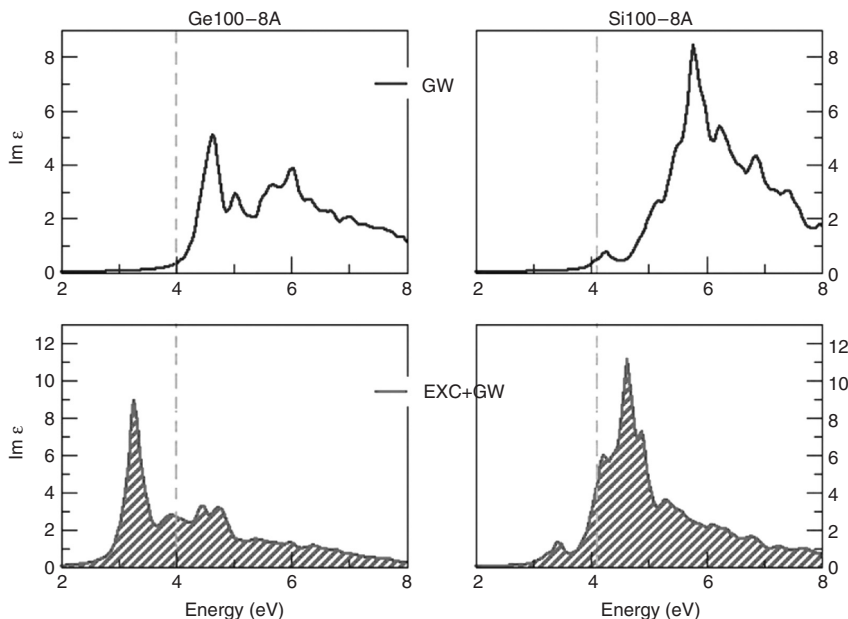


**Figure 26** Imaginary part of the dielectric function of [100] oriented Ge-NWs (left panels) and Si-NWs (right panel) with diameters of 0.8 nm. The first row shows optical spectra at the GW level, the second row shows the spectra obtained including excitonic effects. The dashed line represents the GW optical gap.

binding energies of  $\sim 1$  eV obtained for semiconducting carbon nanotubes of comparable effective width [119,120], where the overlap is limited to the two-dimensional nanotube wall. Furthermore, we find significant cancellation of self-energy and electron–hole interaction effects in the wires which, resembling a string of small clusters, have a quasi zero-dimensional character.

#### 4.2. Doped silicon nanowires

Few investigations have been dedicated to the influence on the electronic and transport properties of doping [164,165]. In particular, due to their application in electronic devices, the main efforts have been devoted to the study of B and P single doped Si-NW, while only one ab-initio study has investigated B and P co-doping [165]. For this reason, we have recently performed a systematic analysis of the effect of B and P co-doping in Si-NW, focusing not only on the structural properties but also on how doping influences the electronic and optical properties. Here we aim to cover the main outcomes of this work and illustrate specific results only for one single-doped and co-doped H-passivated Si-NW (with a linear cross section of about 1 nm) grown in the [110] direction. In particular we have considered different position for the impurities in the Si-NW, moreover we have varied the unit cell in our

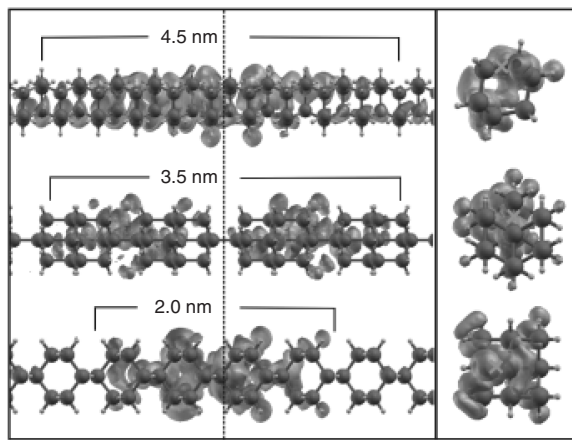


**Figure 27** Geometrical structures of the 0.4 nm Ge wires in the [110] (top), [111] and [100] (bottom) directions shown from the side (left) and from the top (right). Large spheres represent Ge atoms; small spheres are H atoms used to saturate the dangling bonds. The grey isosurface gives the probability distribution  $|\psi_{\text{exc}}(r_r, r_h)|^2$  of finding the electron when the hole is fixed in a given position (the e–h localization length  $L$  is reported for each wire). The hole positions lie on the dashed line in the left panel and are represented by the crosses in the right panel.

calculations. Augmenting the unit cell corresponds to an increase of the overall number of atoms within the cell and thus to a decrease in the dopant concentration. Figure 28 shows how the formation energy for the B and P co-doped Si-NW changes as a function of the position of the dopants within the nanowire. In the figure the inset shows the single Si-NC unit cell used in this case. We note that the minimum is reached when the P atom moves to a surface position. Moreover in the corresponding case (not shown in the figure) where the P impurity is located in a subsurface position and the B atom is in a surface site the FE becomes negative. Indeed it is worthwhile noting that in all cases of single-doped Si-NW the FE shows a high positive value (1.13 eV and 0.66 eV for the single B and P doped nanowire respectively), thus confirming the stabilizing role of compensated doping. Concerning the electronic properties, the band structure show a direct energy gap behavior at  $\Gamma$ , whose values depends on the impurity position. For the positions labelled 1, 2 and 3 in Figure 28 these values are 0.63 eV, 0.08 eV and 0.97 eV respectively.

If we concentrate on the dependence of the doped Si-NW properties on the dopant concentration, we note first that on augmenting the number of atoms in the cell (thus lowering the dopant concentration) the formation energy lowers. For the smallest unit cell (28 atoms in total) the FE shows a value of 0.41 eV, while using a two-times (56 atoms), three-times (84 atoms) and four-times (112 atoms) larger unit cell brings this value to -0.15 eV, -0.60 eV and -0.64 eV respectively. This demonstrates that a lowering of the impurity concentration results in an increase in the stability for the nanowire. The

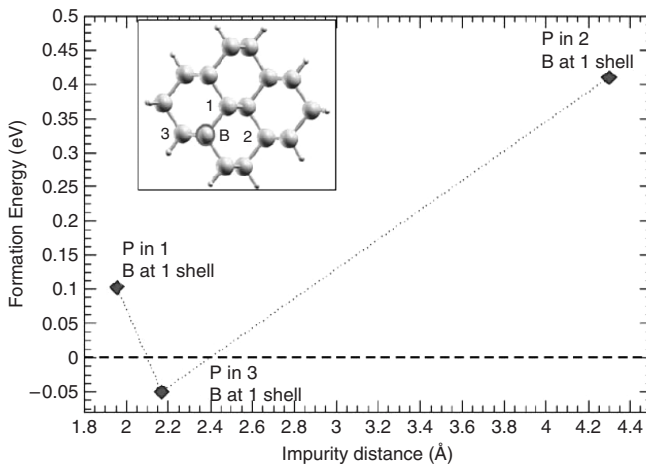


**Figure 28** Formation Energy for the co-doped Si-NW (shown in the inset) as function of the related position between the two dopants. The B (impurity) is frozen in a subsurface site, while the P atom occupies different substitutional sites labelled 1, 2, and 3. The lines are guides for the eyes.

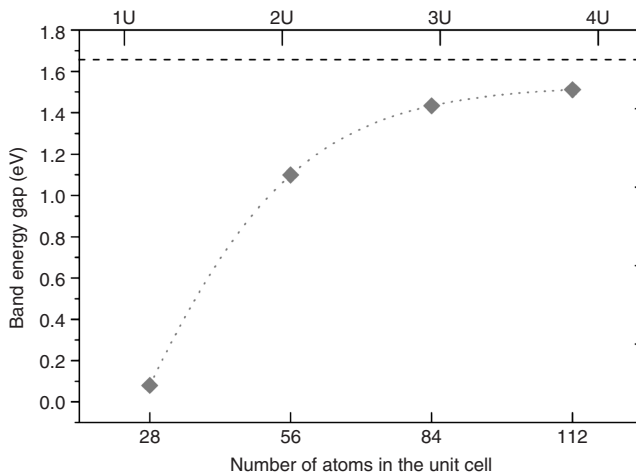


**Figure 29** DFT-GGA direct band-gap calculated at the  $\Gamma$  point for the co-doped Si-NW with respect to the number of atoms in the unit cell. A larger number corresponds to a decrease in impurity concentration. The dotted line is a guide for the eyes. The dashed line corresponds to the band-gap for the undoped Si-NW.

impurity concentration also plays a role regarding the electronic properties. From Figure 29 we see that the direct band-gap increases as the impurity concentration lowers, asymptotically approaching the value of the band-gap

of the undoped Si-NW. This is another indication of how doping can modify the electronic and optical properties of Si nanostructures.

## 5. TWO-DIMENSIONAL SYSTEMS

In this section we will analyze the structural, electronic and, in particular, the optical properties of Si and Ge based nanofilms [166] and of Si superlattices [167] and multiple quantum wells [168] where  $\text{CaF}_2$  and  $\text{SiO}_2$  are the barrier mediums. The quantum confinement effect and the role of symmetry will be considered by changing the slab thickness and orientation and also the role of interface O vacancies will be discussed.

### 5.1. Si and Ge nanofilms

In this section a careful comparison of the electronic and optical properties of Ge quantum films with those of Si quantum films is presented. The Si and Ge free-standing quantum films considered here are constructed keeping the same lattice periodicity and the same interatomic distance as in the bulk material. Their surfaces are oriented along the (100), (110) and (111) directions. For each orientation two effective thicknesses ( $\sim 0.65$  and  $1.05$  nm) have been chosen for the analysis. H atoms are used to terminate dangling bonds at the surface. The Si–H and Ge–H bond lengths have been taken to be 0.1481 and 0.1525 nm, respectively, corresponding to those in  $\text{SiH}_4$  and  $\text{GeH}_4$  molecules. The calculations of the electronic and optical properties are done within density functional theory using the linearized augmented plane wave (LAPW) method that is implemented into the WIEN97 code [169]. For details of the calculation the reader is referred to Ref. [166]. The real  $\epsilon_1$  and imaginary  $\epsilon_2$  part of the dielectric function together with the optical absorption coefficient  $\alpha$  has then been evaluated as described in Section 2.1.1.

The band structures of Si and Ge nanosize films (1 nm thick) calculated along high-symmetry directions of the 2D Brillouin Zone (BZ) are shown in Figure 30 for all the considered orientations. First of all the valence band dispersion is found to be very similar for both Si and Ge films of the same orientation. It is also important to point out the absence of surface/interface states in the band gap energy region in all cases due to the full H passivation of surface dangling bonds. Looking at the different surface symmetry, an interesting feature for the (100)-oriented films is that the band gap appears to be direct at the  $\Gamma$  point, in this case, for both Si and Ge systems. A quite different character for the band gap is observed for the semiconductor (110) films. In the case of Si the gap is still direct at the BZ center, whereas for Ge the band gap is now indirect as the conduction band minimum lies on the  $\Gamma\text{-}X_1$  axis. Similarities in the conduction band dispersion can be seen for the (111) slabs, even if the band gap behavior is quite different. For the Si film the folding of the bulk energy bands has resulted in the appearance of an indirect band gap along the  $\Gamma\text{-}M$  line. It should be noted that the  $\Gamma\text{-}M$  direction of the

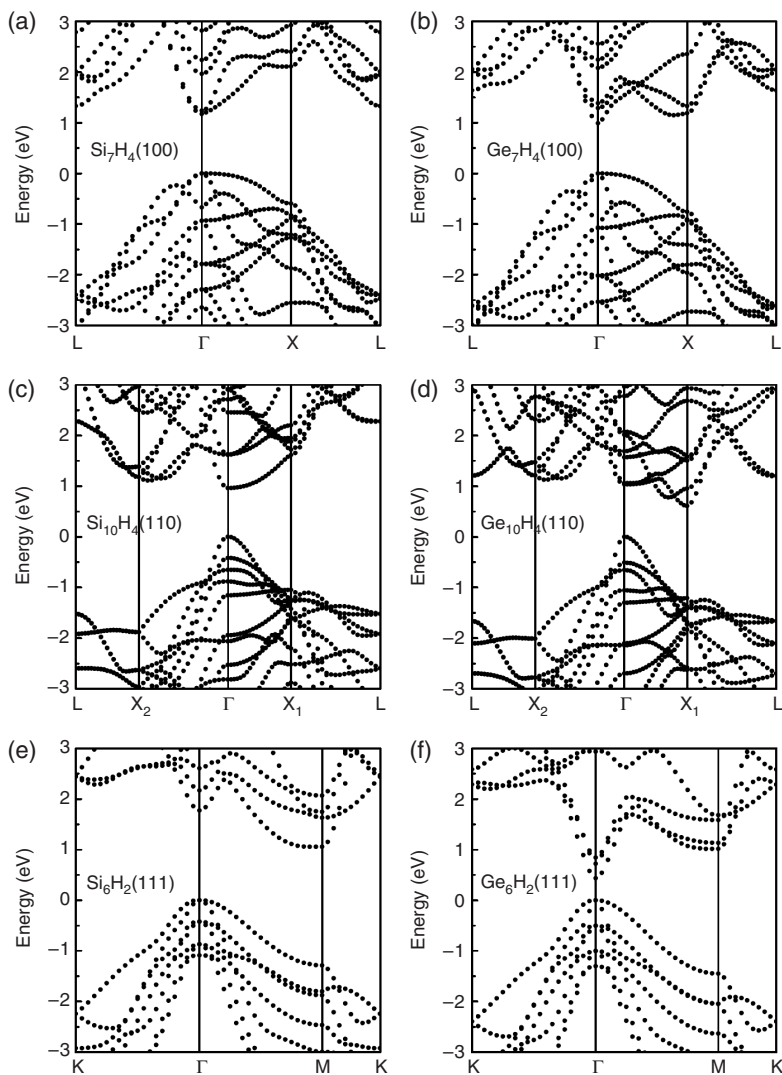


**Figure 30** Electronic band structures of  $\text{Si}_m\text{H}_n$  and  $\text{Ge}_m\text{H}_n$  quantum films of about 1.0 nm thickness for different orientations ( $m$  and  $n$  refer to the number of Si(Ge) and H layers in the considered film): (a)  $\text{Si}_7\text{H}_4$  (1 0 0); (b)  $\text{Ge}_7\text{H}_4$  (1 0 0); (c)  $\text{Si}_{10}\text{H}_4$  (1 1 0); (d)  $\text{Ge}_{10}\text{H}_4$  (1 1 0); (e)  $\text{Si}_6\text{H}_2$  (1 1 1); (f)  $\text{Ge}_6\text{H}_2$  (1 1 1).

2D hexagonal BZ corresponds to the  $\Gamma$ -X direction of the three-dimensional face-centered cubic BZ where the bulk Si conduction band minimum occurs. For Ge films, instead, there is a well resolved conduction band minimum at the  $\Gamma$  point, thus indicating direct band gap character.

The different behavior (direct versus indirect band gap) of Si and Ge with respect to the film orientation can be explained in term of confinement effects on the conduction band minima (CBM) of the two semiconductors. Whereas the six equivalent ellipsoidal CBM of bulk Si occur in the (100) directions about 80% of the way to the zone boundary, in bulk Ge there are eight symmetry-related ellipsoids with long axes along the (111) directions centered on the midpoints of the hexagonal zone faces. Also the different confinement energy shifts with respect to the orientation of the layer can be interpreted in terms of the different highly anisotropic behavior of the effective masses for bulk Ge and Si [170,171].

Looking then at the optical properties one can see if the appearance of a direct band gap is sufficient to originate strong optical transitions at the band gap minimum. The calculated imaginary part of the dielectric function  $\epsilon_2$ , as a function of photon energy, is presented in Figure 31 for all the considered Si and Ge films. In general terms, the spectral structures of  $\epsilon_2$  of both Si and Ge films has a major peak around 4 eV. This peak corresponds to the  $E_2$  spectral feature occurring at the dielectric function of the bulk materials [172]. For both systems a reduction of the peak intensity is observed when the thickness of the film is decreased, thus reflecting a quantum confinement effect. However, for (100) and (110) surface oriented films this peak reduction is followed by its shift to higher energies, whereas for [111] films it moves to lower photon energies. An interesting comparison between optical properties of Si and Ge films can be made in the low-energy region. Taking into account the LDA underestimation of the band gap, this is the optical region of interest. Here new structures are present that are absent in the case of bulk Si and Ge. For all the structures there is a blue-shift of the  $\epsilon_2$  onset owing to the reduction in the effective-film thickness. Moreover, all the Ge films in the three directions considered have a visible shoulder at the low-energy region (about 1.01.2 eV). Since  $\epsilon_2$  is directly related to the absorption coefficient, the shoulder in the  $\epsilon_2$  curve indicates that there is a strong absorption around this characteristic energy. Moreover, since for the (100)- and (111)-oriented structures the band gap is direct, there is also the possibility of strong PL intensities in these cases. However, this intense feature does not appear for Si films though the energy band structures of (100)- and (110)-oriented structures possess a direct gap.

A deeper insight is gained by analyzing the strength of the optical transitions in the films studied. Looking at the squared optical matrix elements for significant direct transitions between the valence and conduction bands, it is found that for both (100) and (110) Ge films they are orders of magnitude higher than for analogous Si films, moreover for the Ge(100) film those related to the band gap, that is direct, are only one order of magnitude less than the corresponding in bulk GaAs. This property can be useful for optoelectronic applications of Ge quantum films. The first direct transitions in (111) Ge films is practically forbidden; only the second transitions show an appreciable weight. For all Si films the calculated squared optical matrix

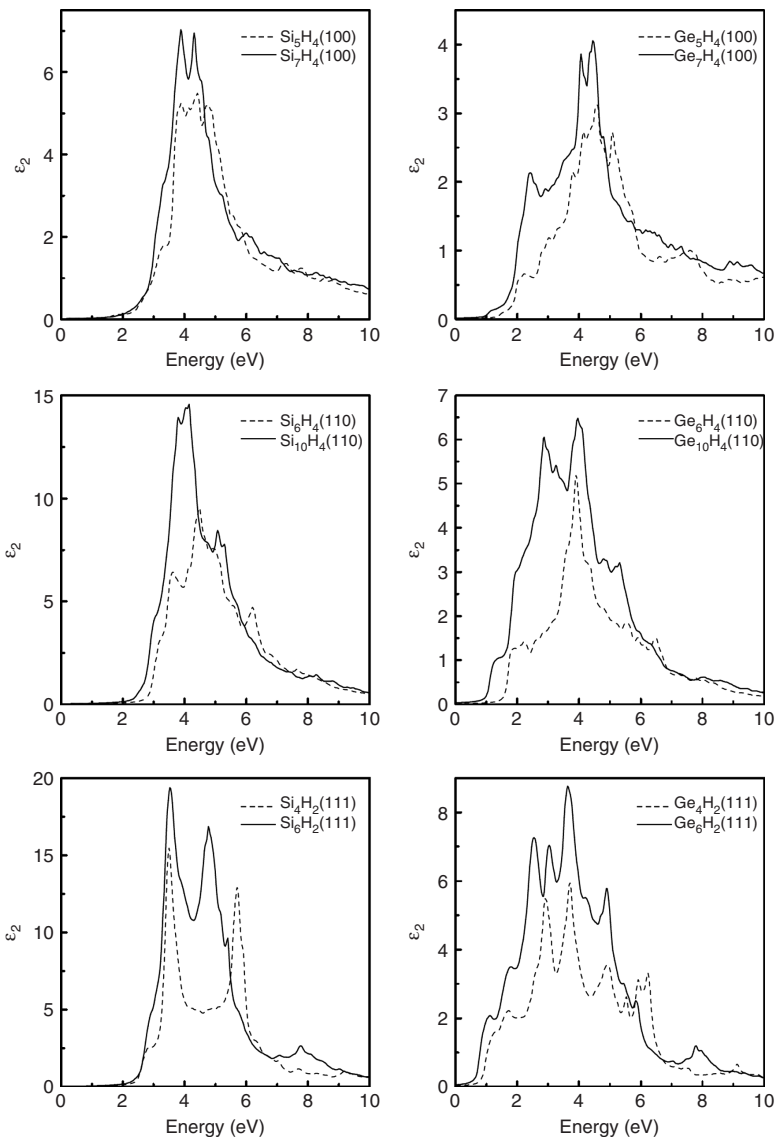


**Figure 31** Calculated imaginary part of the dielectric function of Si and Ge quantum films for different orientations and thicknesses. The curves are convolved with Lorentzian broadening of 0.1 eV.

elements are small, only Si(111) films (showing an indirect gap) have an important contribution at high energies close to the direct gap of bulk Si. It is also worthwhile remarking that the squared optical matrix elements related

to the second lowest conduction band for (110) and (111) Ge films have the same order of magnitude as the one for GaAs bulk.

The different behavior between the Si and Ge quantum film is related to the different character of the CBM. The CBM are obtained through the folding of the bulk energy bands on the film surface; whereas in Si the CBM mainly retain the original indirect character of the absolute conduction band minimum along the (100) direction, in the case of Ge, especially for the (100) orientation, there is an important mixing between direct and indirect character, owing to the fact that the conduction band minimum at  $\Gamma$  in bulk Ge is only few meV higher than the absolute conduction band minimum along the (111) direction.

The effect of quantum confinement is also pronouncedly seen in the real parts of the dielectric function. The characteristics versus photon energy behavior for all considered Si and Ge quantum films are presented in Figure 32. One can observe the reduction of the maximum value of  $\epsilon_1$  as well as its value at zero energy (static dielectric constant) when going to the thinner films. The calculated values of the static dielectric constant ( $\epsilon_1(0)$ ) for the films considered are considerably smaller than that of bulk material. Moreover, for the same film thickness  $\epsilon_1(0)$  appears to be higher for the Si structures as compared to the Ge ones, despite the fact that for bulk the Ge value is higher than the Si one. Even if, as stated above, the data shown for the dielectric functions are those relative to the supercell calculation, for films of similar width, at least, semi-quantitative comparison is possible, since the ratio between the volume occupied by the isolated layer and the supercell volume is almost constant in these cases.

## 5.2. Si/CaF<sub>2</sub> multi-quantum-wells

The lattice-matched system CaF<sub>2</sub>/Si/CaF<sub>2</sub> is the prototype of a well-controlled and ordered Si-based system with a known microscopic structure. The self-consistent electronic structures of these systems have been calculated by means of the Linear Muffin-Tin Orbitals method in the Atomic Sphere Approximation (LMTO-ASA), which has proven to describe correctly the Si/CaF<sub>2</sub> interface properties [173]. Exchange and correlation effects are included within the density-functional theory in the local density approximation. These calculations for ultrathin Si(111) layers embedded in CaF<sub>2</sub> have shown that quantum confinement causes a band-gap opening which depends on the Si layer thickness, while Si-Ca hybridization effects at the interface lead to dipole-allowed optical transitions all over the Brillouin zone [173]. This section is devoted to the description of the first principles optical properties of Si/CaF<sub>2</sub> multi-quantum wells (MQWs) [167]. In order to overcome the lack of periodicity perpendicular to the interface, for MQW we use supercells formed by a variable number of Si double layers (DL's), separated by CaF<sub>2</sub> layers. The number of CaF<sub>2</sub> layers in the calculations has been chosen large enough to make the central CaF<sub>2</sub> layer exhibits bulk-like properties.

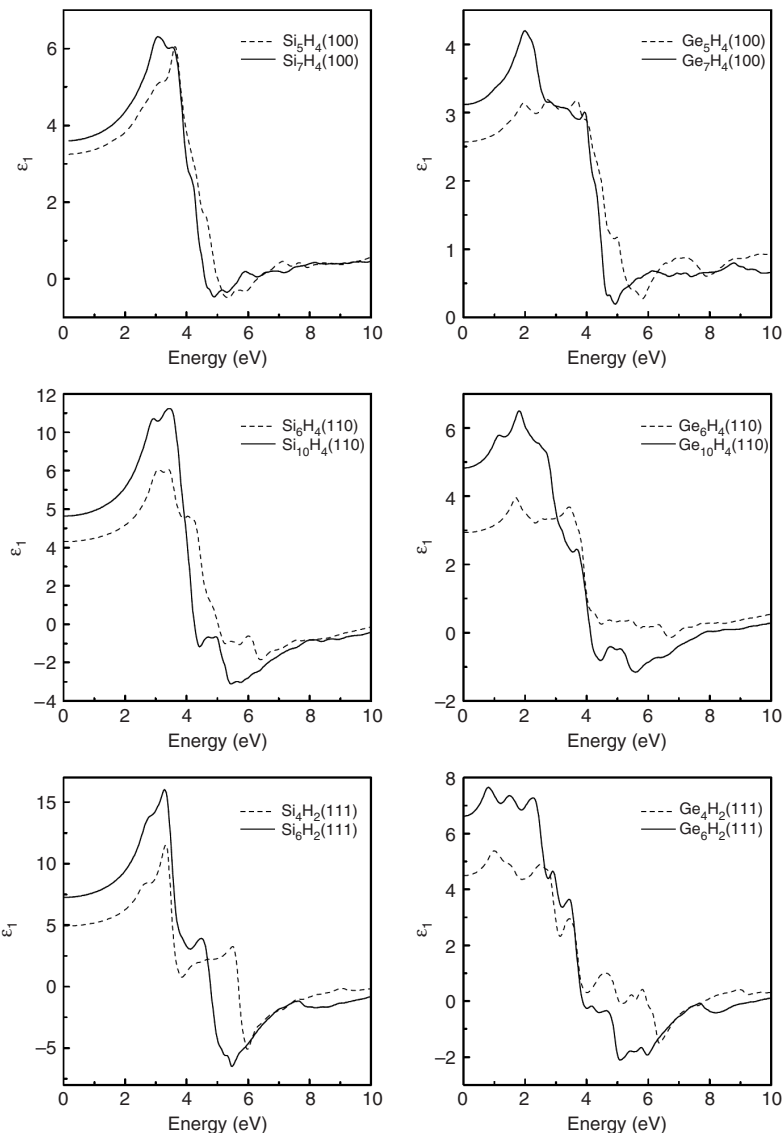


**Figure 32** Calculated real part of the dielectric function of Si and Ge quantum films for different orientations and thicknesses. The curves are convolved with Lorentzian broadening of 0.1 eV.

Throughout, we have used the lattice constant of  $\text{CaF}_2$  (only 0.6% greater than in bulk Si) except for the interfacial Si–Ca distance, which is taken to be 3.15 Å, as found [174,175] experimentally. Our structural model follows the experimental outcomes [174,175] with the first monolayer of  $\text{CaF}_2$  losing

half of its fluorine atoms leading to the Ca–Si bond at the interface. The interface Ca atoms occupy the  $T_4$  sites; the triangular filled sites on top of the second layer Si atoms, while the F atoms are located on the  $H_3$  sites, the triangular hollow sites on top of the fourth-layer Si atoms. For further details on the structural model used, the reader is referred to Refs. [167,173]. The thickness of the Si wells embedded in  $\text{CaF}_2$  ranges from 0.55 to 2.44 nm. The first value corresponds to the case of a single DL of Si embedded in  $\text{CaF}_2$ , the second to seven DL's of Si. The optical properties for bulk Si and for the Si slabs embedded in a  $\text{CaF}_2$  matrix, as a function of the Si layer thickness, have been computed by evaluating the real ( $\epsilon_1$ ) and imaginary ( $\epsilon_2$ ) part of the dielectric function, as described in Section 2.1.1. The comparison between bulk and slab results gives the possibility to explain features entirely due to the confinement effect. In Figure 33, we show the dependence of our calculated  $\epsilon_2$  on the thickness of the Si slab embedded in  $\text{CaF}_2$ . For comparison, we also report our  $\epsilon_2$  result for bulk Si (solid line). For ease of discussion, three main regions have been identified, according to the different portions of  $\epsilon_2$ , and have been indicated with labels from I to III. Region III between  $\sim 10$  and  $\sim 14$  eV is mainly related to the  $\text{CaF}_2$  contribution to the  $\epsilon_2$  of the MQWs. We note that the features in this region gain weight with respect to region II (between  $\sim 3$  and  $\sim 6$  eV) on reducing the thickness of the Si slab; clearly this is due to the increase in weight of the  $\text{CaF}_2$  side with respect to Si in the MQWs. In fact, region II is directly related to the crystalline Si contribution to the  $\epsilon_2$  of the MQWs; this is the region to be compared directly to the Si bulk result. The main characteristic of region II is the reduction of the maximum value for  $\epsilon_2$ . This reduction exactly follows the lowering in thickness of the Si slab, and it is due to the confinement effect. In particular we note that the  $E_1$  spectral feature at  $\sim 3$  eV in bulk Si is weakened and shifts to the blue as a consequence of quantum confinement effect, whereas the  $E_2$  peak shows a red-shift. A different behavior with respect to the influence of quantum confinement of the critical points of the band structure of Si has been demonstrated in the case of extremely thin layers of porous Si [176].

More important for our discussion is the low-energy region I (between  $\sim 1$  eV and  $\sim 2.5$  eV). Here features appear which are completely absent in the case of bulk Si. If we take into account the  $\sim 0.5$  eV LDA underestimation of the Si energy gap, this is the optical region of interest. Experiments on Si/ $\text{CaF}_2$  MQWs [44–46] show PL and absorption gaps even in the energy region between  $\sim 1.5$  and  $\sim 2.5$  eV, in agreement with our results. Moreover, in Figure 34 we show a blowup of the low energy part of  $\epsilon_2$  in the 1–2 eV range. A blue-shift, consistent with quantum confinement, of the onset of  $\epsilon_2$  for decreasing Si thickness is clearly evident here and also through the energy gap values reported in Table 10. The only exception is the system with one DL of Si, for which the bonding Si–Ca interface state emerges from the valence band. Second, the features of  $\epsilon_2$  in this region are very smooth for the larger Si slab (seven DL's), while their weight increases with confinement.

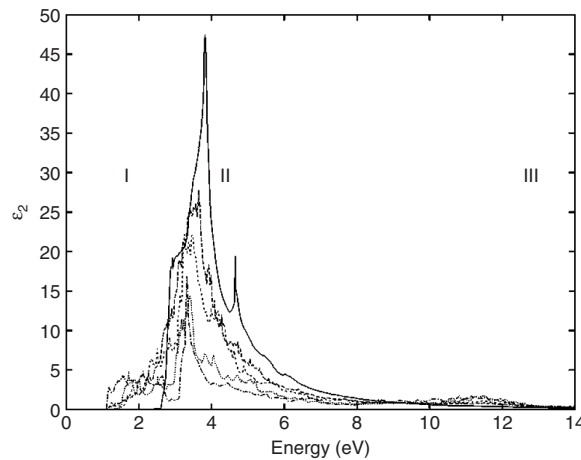


**Figure 33** Calculated imaginary part of the dielectric function  $\epsilon_2$  for Si/CaF<sub>2</sub> MQWs. Large dashed line: seven Si DL's; small dashed line: four Si DL's; dotted line: two Si DL's; dash-dotted line: one Si DL. The values are compared with that of bulk Si: solid line.

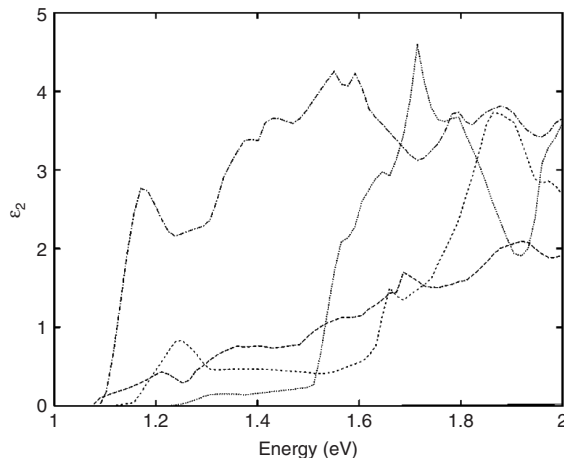


**Figure 34** Same as in Figure 33, in the 1–2 eV energy range.

**Table 10** Calculated energy gaps, energies and oscillator strengths for significant direct transitions at  $\Gamma$  for the different considered MQWs. The values are compared with that of bulk Si

Lattice	Si bulk	1 DL	2 DL	4 DL	7 DL
Size (nm)		0.55	0.87	1.49	2.44
Gap (eV)	0.56	0.76	1.24	0.63	0.56
$\Delta E_{cv}$ (eV)	2.59	2.13	1.81	1.73	1.44
$f_{cv}$	2.53	0.72	0.66	0.42	0.004

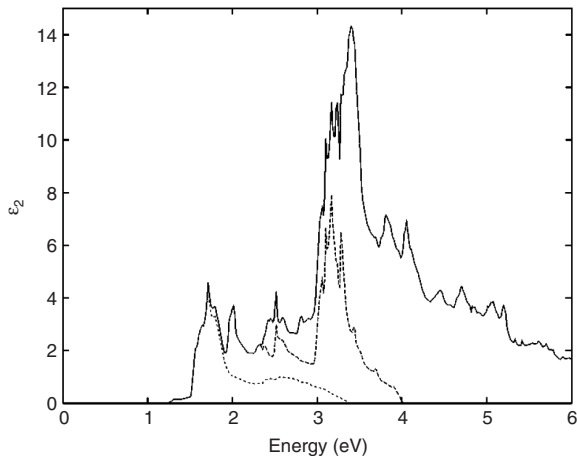


**Figure 35** The most important interband contributions to the imaginary part of the dielectric function of the 2-DL Si/CaF<sub>2</sub> MQWs. Solid line: total  $\epsilon_2$ ; short dashed line: contribution from the transition between the last occupied state and the first unoccupied one; long dashed line: the same considering the last two occupied states and the first two empty states.

In order to explain the transitions which play an important role in the low-energy region, in Figure 35 we show (again for the two-DL Si case) the total  $\epsilon_2$  (solid line), together with the contributions due to the transitions from the last valence band to the first conduction band (short dashed line), and from the last two valence bands to the first two conduction bands (long dashed line). From the figure, the predominant role played by the band edges is evident, in particular for the interface states in the optical region; we remember that for very thin Si slabs the last occupied and first unoccupied states are mostly related to interface states.

The origin of the peaks is related to the presence of significant matrix elements between particular states which are located at, or just below, the top of the valence band and at, or just above, the bottom of the conduction band. The top valence states are mainly *p* Si-derived states, whereas the bottom conduction ones are mainly *p* Si- and *s* and *d* Ca-derived states. The calculated oscillator strengths for the transitions between these states are listed and compared in Table 10. It is worthwhile noting that the oscillator strengths for the matrix elements between these states increase very rapidly as the thickness of the slabs decreases, and that, for layers with thickness less than 2 nm, they are of the same order of magnitude as the direct transition at  $\Gamma$  in bulk Si and only one order of magnitude smaller than those for GaAs. The reason for the rapid increase of the dipole strength with decreasing slab thickness is due to the different localization of the states involved in the transition. The intensity of the oscillator strength for a transition between two states depends not only on the localization in the reciprocal *k* space but also

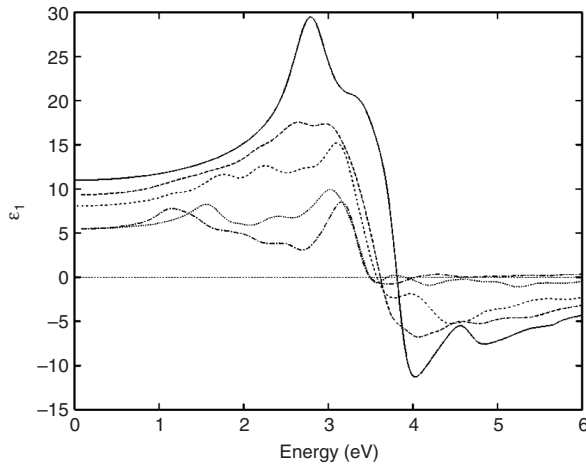


**Figure 36** Real part of the dielectric function  $\epsilon_1$  for Si/CaF<sub>2</sub> MQW's. Large dashed line: seven Si DL's; small dashed line: four Si DL's; dotted line: two Si DL's; dash-dotted line: one Si DL. The values are compared with that of bulk Si: solid line. Results are convolved with a Gaussian broadening of 0.1 eV.

on the localization in real space, i.e., in which layers these states are localized. For very thin slabs these states are both strongly localized at the interface, whereas for the seven-DL slab case they are spread out over the entire Si slab. Thus the optical transition matrix element which indicates the probability of the transition decrease as the number of Si layers is made larger.

The lineshape of the real part of the dielectric function for each considered MQW is shown in Figure 36 in comparison with the one of bulk Si. A strong reduction of the maximum value of  $\epsilon_1$  in going from bulk Si to quantum wells is clear; moreover, we observe that the high-energy shoulder becomes more important with respect to the main peak in the MQW case. Concerning the calculated values of the static dielectric constants  $\epsilon_1(0)$ , on going from bulk Si to the smaller slab these values reduces from 10.53 (bulk Si) to 9.26 (7DL), 7.98 (4DL), 5.32 (2DL), 5.32 (1DL). We see that all the values are considerably smaller in MQW's than in bulk Si, reflecting quantum confinement effects. The decrease in the static dielectric constant of Si quantum slabs is consistent with the calculated results for Si quantum dots [177] and for Si quantum wires [155]. From the experimental point of view, a similar large reduction of  $\epsilon_1(0)$  (from 11.4 to  $\sim 3$ ) has been observed in porous Si [178]. Moreover it has recently been observed for Si quantum slabs embedded in SiO<sub>2</sub> [52]. The importance of the reduction of the dielectric constant, in order to use Si for optoelectronic purposes, has been pointed out and discussed [179]. Another interesting implication of this reduction is that the exciton recombination energy in the ultrathin Si slabs could be significantly increased. In the case of Si quantum dots, Wang and Zunger found that for quantum dots whose radius

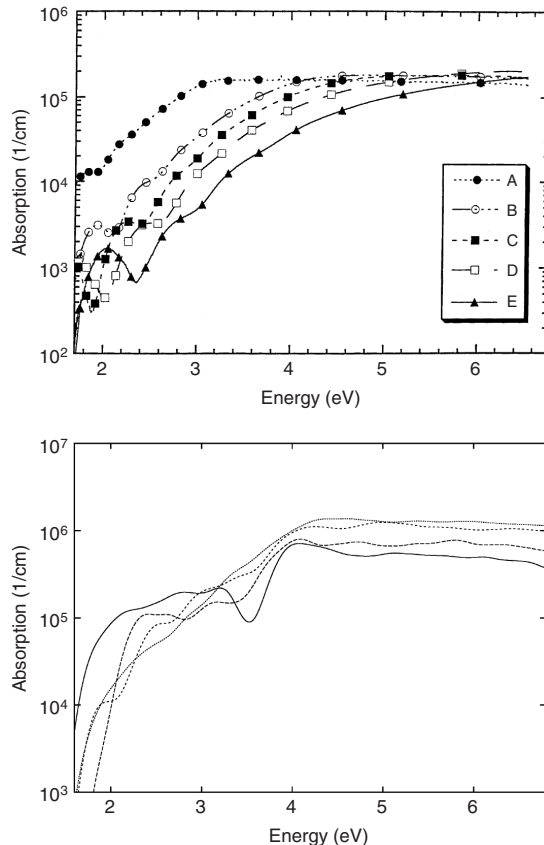


**Figure 37** Log to the base ten of the absorption coefficient ( $\text{cm}^{-1}$ ). Top panel: experimental results from Ref. [46]; Si thickness (A) 5.0 nm, (B) 2.0 nm, (C) 1.6 nm, (D) 1.5 nm, (E) 1.0 nm. Bottom panel: theoretical results; large dashed line: 7 Si DL's, small dashed line: 4 Si DL's, dotted line: 2 Si DL's, dash-dotted line: 1 Si DL.

is less than 2 nm the electron–hole pair is confined by the physical dimension of the dot, not by the Coulomb attraction [177].

We have also calculated the absorption coefficient  $\alpha$  (see Figure 37 bottom panel) that can be compared with optical absorption measurements performed on Si/CaF<sub>2</sub> MQW's synthesized by molecular beam epitaxy [44,46] (see Figure 37 top panel). A striking resemblance between the two results is evident. In both results we observe a blue-shift of the onset and moreover a decrease of the optical absorption with decreasing Si layer thickness. The discrepancy in the absolute value of  $\alpha(\omega)$  is a consequence of the use of the repeated slab scheme in the calculations.

### 5.3. Si/SiO<sub>2</sub> superlattices

Silicon/silicon dioxide (Si/SiO<sub>2</sub>) interfaces today play a crucial role in semiconductor technology and could tomorrow play the same crucial role in the field of photonic applications. Through the conventional thermal oxidation process, flat Si/SiO<sub>2</sub> interfaces with very few interface states can easily be obtained. Why the Si/SiO<sub>2</sub> lattice has few interface states is an open question. Actually, the large lattice mismatch of this interface would induce defects in the structure breaking the Si–Si and Si–O–Si bonds in many places and all these defects should create a large number of interface states: this is inconsistent with the experimental evidence. For this reason some mechanisms have to act to passivate the interface states and a lot of hypotheses have been made on the passivation mechanism and on how it works. In the light of these considerations well-characterized Si/SiO<sub>2</sub> nanostructures with variable Si thickness are desirable in order to better understand the role played by the nature of the interface and by the dimensionality on the electronic and optical properties. In particular we are interested in the optical properties of Si/SiO<sub>2</sub> quantum wells and superlattices (SLs) with variable Si layer thickness that we have studied using a first principle method within the LMTO-ASA scheme [168]. We performed our theoretical investigation considering one of the most promising passivation mechanisms, the presence of an extra O atom double bonded to the Si at the interface, proposed by Kageshima and Shiraishi [180–184] and supported by other theoretical models [18,185] and experimental findings [47,186,187]. In order to overcome the lack of periodicity perpendicular to the interface, we use, for SLs calculations, supercells formed by a variable number of Si elementary cells, separated by SiO<sub>2</sub> layers. The elementary Si cell is constituted of five Si layers for a thickness of 0.543 nm, while the SiO<sub>2</sub> thickness of 0.768 nm is the same for all the considered SLs and is large enough to make the central SiO<sub>2</sub> layer exhibit bulk-like properties. We used a  $\beta$ -cristobalite structure for the SiO<sub>2</sub> layer, that has a diamond like symmetry as Si, and leads to a simple model for the interface. The lattice parameter for the  $\beta$ -cristobalite is approximately  $\sqrt{2}$  times that for Si, so we obtain a perfect match using a lattice constant of  $\sqrt{2} \times 0.543\text{ nm} = 0.768\text{ nm}$  for SiO<sub>2</sub>, as Batra [188] and Tit and Dharma-Wardana [189] did, and applying the  $\beta$ -cristobalite structure along the diagonal of the (001) surface unit cell of the Si layer. Using this interface model, as many bonds as possible are formed between Si and SiO<sub>2</sub>, but a Si atom at the interface remains unsaturated. For this reason we introduce a double bonded extra O atom (the black atoms in Figure 38) positioned at a distance of 0.1446 nm from the Si surface in accordance with the suggested passivating mechanism [180]: the model used and the atomic arrangement across the interface are shown in Figure 38. Experiments show that the interface is rather abrupt and with very few interface states (this implies a density bulge which has also been

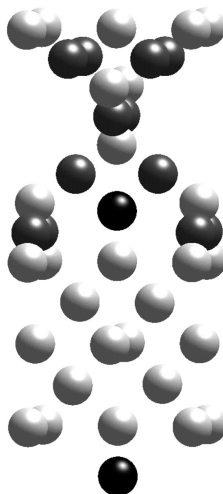


**Figure 38** The Si/SiO<sub>2</sub> SL elementary cell with one unit of Si:Si atoms are pale grey and O atoms are dark grey. The  $\beta$ -cristobalite is matched to the Si by rotating the former about the [0 0 1] axis by  $\pi/4$ . An extra O atom (black) is added to saturate the interface bonds.

observed [190]) and it is also known that the Si/SiO<sub>2</sub> interface contains all the suboxide charge states Si<sup>+</sup>, Si<sup>2+</sup> and Si<sup>3+</sup>. The model that we use produces a density bulge at the interface and also contains the suboxide-charge states Si<sup>+</sup> and Si<sup>2+</sup>, but not the Si<sup>3+</sup>, as is also the case for the energy optimized model due to Pasquarello et al. [191] and Kageshima and Shiraishi [180].

To analyze the role played by the dimensionality we considered three different Si<sub>[n]</sub>-SiO<sub>2</sub> wells with  $n$  (the number of elementary Si cells) equal to 1, 2 and 3: the thickness of the wells, taken as the distance between the Si atoms at the two interfaces along the growth direction, is 0.543, 1.086 and 1.629 nm, respectively. To understand the role played by O related defects at the interface of the well we considered two systems, the first fully passivated through the double bonded extra O atom (the black atoms in Figure 38) added to saturate the Si dangling bonds, and the second with an O vacancy at the interface produced removing the same extra O atom.

Concerning the role of dimensionality we observed, in the three fully passivated cases, that the material is a semiconductor, as the band structure of the Si<sub>[1]</sub>-SiO<sub>2</sub> SL in Figure 39(a) shows, and that there is an opening of the gap as the thickness of the Si layer decreases. The band structure shows a gap which is slightly indirect for the presence of a state at the top of the valence band (mostly related to the Si atoms in the inner Si layer), that is partially due to the interaction between the interface Si and its double-bonded O atom. If we remove this extra O, leaving the two dangling bonds of the interface Si unsaturated, we find that the material is still a semiconductor with a new

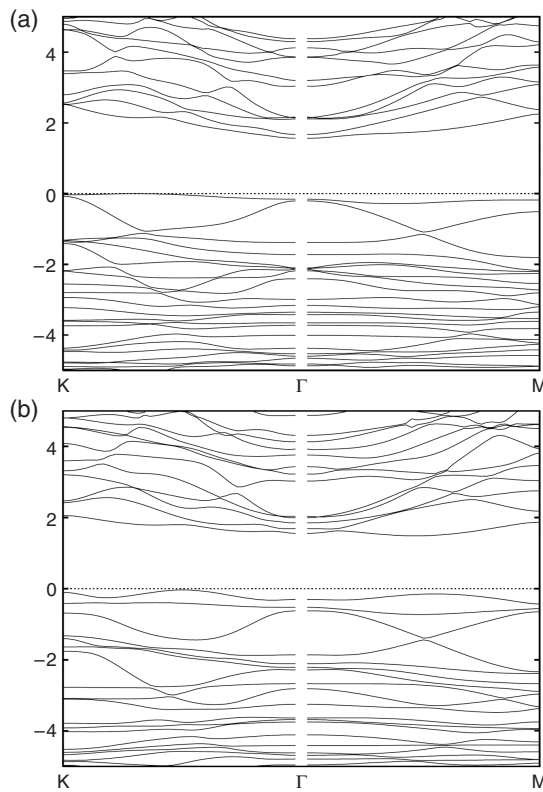


**Figure 39** Band structure of the (a) fully saturated and (b) partially saturated  $\text{Si}_{[1]}-\text{SiO}_2(0\ 0\ 1)$  SL projected along the two symmetry directions of the 2D Brillouin zone of the  $(0\ 0\ 1)$  surface. K and M represent, respectively, the k-points in the corner and in the middle of the side of the 2D Brillouin zone. A self-energy correction of 0.8 eV has been added to the conduction states. Energies (in eV) are referred to the valence band maximum.

state, a dangling bond interface state, at the top of the valence band that reduces the band gap by 0.12 eV (Figure 39(b)). If we then consider the band structure for the  $\text{Si}_{[2]}-\text{SiO}_2$  and  $\text{Si}_{[3]}-\text{SiO}_2$  SLs with the O vacancy at the interface, we found that, as for the fully saturated lattices, the material is an indirect semiconductor with a progressive gap opening observed as the thickness of the Si layer is reduced and that the interface state, found for the partially passivated  $\text{Si}_{[1]}-\text{SiO}_2$  SL, is now inside the valence band: the interesting fact is that the energy separation between this interface state and the bottom of the conduction band is almost unaffected by the Si layer thickness. The results obtained for the optical properties directly reflect the electronic ones. Actually, if we look at the imaginary part of the dielectric function for the fully saturated lattice with a single Si elementary cell we find new interesting optical features in the visible range completely absent in bulk Si.

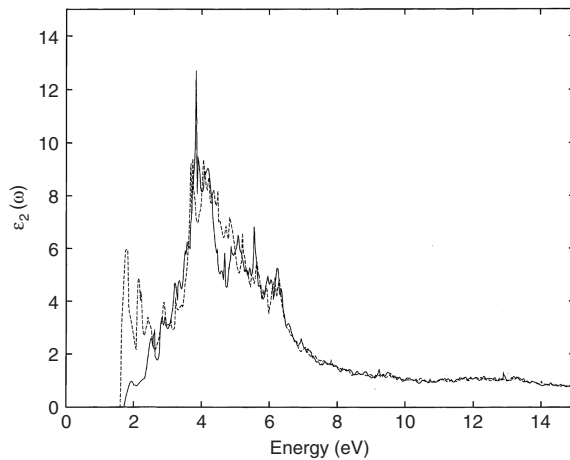


**Figure 40** The imaginary part of the dielectric function,  $\epsilon_2$ , for the  $\text{Si}_{[1]}-\text{SiO}_2(0\ 0\ 1)$  fully passivated system (—) compared with the  $\epsilon_2$  of the  $\text{Si}_{[1]}-\text{SiO}_2(0\ 0\ 1)$  system with an O vacancy at the interface (---). A shift of 0.8 eV higher in energy has been applied in order to overcome the LDA underestimation of the gap.

If we then introduce the interface defect (the O vacancy) in the SL, comparing the  $\epsilon_2$  for the fully saturated and partially saturated lattice (Figure 40), we observe a new intense asymmetric peak at the low energy edge. The same asymmetric peak can be observed for the  $\text{Si}_{[2]}-\text{SiO}_2$  and  $\text{Si}_{[3]}-\text{SiO}_2$  SLs with the O vacancy at the interface. In Figure 40 the imaginary part of the dielectric function is shifted higher in energy by 0.8 eV, in order to overcome the LDA underestimation of the gap, having in this way a better comparison with the experimental data. The value of this self-energy correction is appropriate for our Si confined systems as previous studies [151,192] have shown. Our results can be discussed and compared with experimental data as a function of the Si layer thickness. A lot of experimental work has been done on the optical properties of  $\text{Si}/\text{SiO}_2$  quantum wells and SLs [15,47–50], nevertheless the situation is still not clear. Anyway, our results are in really good agreement with the experimental data of Kanemitsu and Okamoto [51]. They have studied the luminescence properties of crystalline-Si/ $\text{SiO}_2$  single quantum wells. In thin well samples they observed efficient PL in the visible spectral region. In this asymmetric PL spectra they were able to fit two Gaussian bands: a weak band that shifts to higher energy (from  $\sim 1.5$  to  $\sim 1.9$  eV) with decreasing Si layer thickness (from 1.7 to 0.6 nm), and a strong band, at  $\sim 1.65$  eV, almost independent of the well thickness. Kanemitsu and Okamoto [51] attributed the weak band to quantum confinement effects and the strong one to radiative recombination in the interface region; moreover, from the presence of TO phonon related structures, both in the resonant PL spectrum and in the PL polarization spectrum of the quantum confined

related band, they speculated about an indirect optical-transition nature for the size quantized states of the two-dimensional (2D) Si wells.

Our task here is to clarify the experimental status for the Si/SiO<sub>2</sub> quantum wells and SLs through the comparison between theory and experiments. We evaluated the imaginary part of the dielectric function that is directly related to the dipole matrix elements; from these we can obtain information directly on absorption, and indirectly on the relevant radiative PL processes, considering the simplest radiative recombination mechanism in which an electron excited from the valence to the conduction band through the absorption of an energy  $E$  can directly recombine through the emission of the same energy. Actually, in our calculated  $\epsilon_2$  for the partially saturated SL (long-dashed line in Figure 40), we observed that the first asymmetric peak can be fitted by two Gaussian bands as Kanemitsu and Okamoto [51] did in their PL spectra: the first band, more intense, located at  $\sim 1.7$  eV, is related to the interface state and the second one, weaker and located at  $\sim 1.9$  eV, is due to the Si bulk-like states. Increasing the Si layer thickness these two Gaussian bands remain recognizable in the  $\epsilon_2$  behavior, but their position changes. Repeating the fitting of these peaks with the Gaussian bands for each lattice and plotting them together we are able to see if and how these states are affected by dimensionality.

In Figure 41 the Gaussian bands are shown labelled with a I for the interface band and with a Q for the bulk-like band for the lattices with 3 (Figure 41(a)), 2 (Figure 41(b)) and 1 (Figure 41(c)) Si cells. A shift to higher energies (from  $\sim 1.4$  to  $\sim 1.9$  eV) is evident for peak Q when the thickness of the Si layer decreases: this is typically a quantum confinement effect. The energy peak positions related to the quantum confinement states are also confirmed by the corresponding results for the fully saturated systems. The peak I, instead, is almost unaffected by the dimensionality of the Si slab and remain positioned at around 1.7 eV. The comparison between our outcomes in Figure 41 and Kanemitsu and Okamoto's [51] results in Figure 41 (right panel) fully confirms their interpretation on the nature of the PL in these materials. Not only the energy positions of the quantum confined and interface related peaks are in good agreement, but also the relative intensity of the two bands, with respect to each other, agrees.

## 6. CONCLUSIONS

In the last decade there has been considerable and reasonably satisfactory progress in the understanding of the theoretical aspects of the structural, electronic and optical properties of Si nanostructures. Here we have presented the outcomes of our theoretical study of the properties of Si nanosystems, considering Si nanodots, Si nanowires and Si nanoslabs. We have demonstrated, by first-principle calculations, also beyond the single particle approach, that the structural, electronic, and optical properties of the

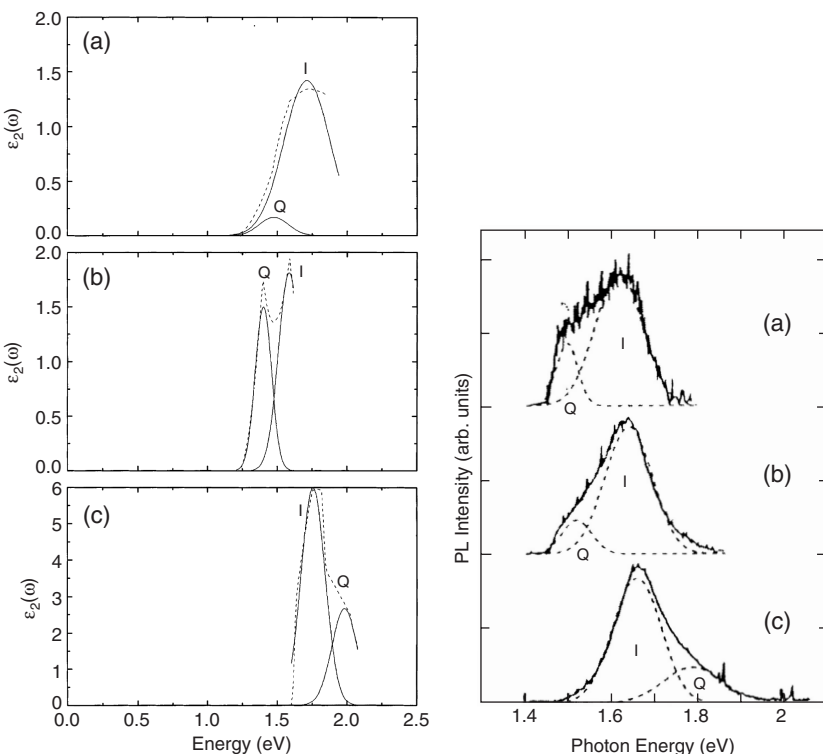


**Figure 41** Left panel: calculated  $\epsilon_2$  first asymmetric peak (---) and its Gaussian fit (—) for the (a)  $\text{Si}_{[3]}-\text{SiO}_2$ , (b)  $\text{Si}_{[2]}-\text{SiO}_2$  and (c)  $\text{Si}_{[1]}-\text{SiO}_2$  superlattices. The letter I indicates the interface Gaussian band while the letter Q indicates the bulk-like Gaussian band. Right panel: PL spectra of c-Si/SiO<sub>2</sub> single quantum wells under 488 nm laser excitation at 2 K: (a) 1.7 nm, (b) 1.3 nm and (c) 0.6 nm thickness. The asymmetric PL spectra can be fitted by two Gaussian bands, the weak Q band and the strong I band [51].

nanosystems strongly depend not only on the quantum confinement effects, but also on the different passivation regimes and on the nature of doping.

In the case of nanodots, we considered both undoped and doped Si-based nanocrystals, whose dimensions are up to the nanometer range. Particular attention has been paid to the outcomes related to the role of surface termination and to the nanocrystal's excited states. In particular we have found that the presence of an electron–hole pair in the nanocrystals causes a strong deformation of the structures with respect to their ground-state configuration, and this is more evident for smaller systems, that a significant contribution to the Stokes shift arises from relaxation after excitation of the nanocrystal, and that considering the HOMO–LUMO gaps of the ground and excited state as the proper absorption and emission energies is more in error as the cluster gets smaller. Regarding the surface termination effects, we have discussed the role of O at the interface, and we have found that the full inclusion of

the excitonic effects in the calculation of the emission spectra suggest that the Si–O–Si bridge bond is responsible for the strong PL peak experimentally observed in oxidized Si nanocrystals. In relation to the doping we have demonstrated that Si nanocrystals can be more easily simultaneously doped than single-doped, and that by co-doping it is possible to engineer the PL properties of the Si nanocrystals. Moreover, the case of multiple doping has been evaluated and discussed. Concerning the Si nanocrystals embedded in a SiO<sub>2</sub> matrix, in comparison with experiments we have elucidated the important role played by the interface region. Indeed a model for the screening in Si nanoparticles has been presented and discussed.

For Ge and Si nanowires we showed the crucial role played by the electron–hole interaction. We highlighted the effect of the different geometrical structures of nanowires of different orientation on the optical spectra: in some cases the wire is made of connected clusters, while in other cases it resembles a nanotube. Very large excitonic effects, different in the two cases, have been calculated that clearly depend on the orientation and symmetry of the nanowires. It emerged that Ge nanowires show strong optical absorption at lower frequencies than Si nanowires, with the main peak occurring in the visible range. These outcomes, in comparison with the experimental data, helped in understanding the role of self-energy correction and electron–hole interaction on the electronic and optical properties of Si nanowires. In addition, the dependence of the optical anisotropy on the crystalline packing pointed out the structural difference between isolated nanowires and porous Si. Finally, the doping properties of Si nanowires have been calculated and the role of the impurity concentration outlined and discussed.

Concerning the Si nanoslabs, we considered Si nanofilms terminated by H and Si quantum wells covered by CaF<sub>2</sub> and SiO<sub>2</sub>. For the nanofilms, zone folding due to the confinement effect has been found to result in a direct band gap for both [100] Si and Ge nanostructures. For the [110] orientation, only Si films have a direct transition at the Brillouin Zone center. In the case of [111]-oriented Si and Ge films, one may speak of indirect and direct band gap semiconductors, respectively. For the optical properties, it has been shown that for Si films a noticeable increase in  $\epsilon_2$  is observed only at high energies close to the corresponding direct band gap of bulk Si. This is due to the fact that the direct gap appearing in the Si films still retains its original indirect character. Only Ge films possess a characteristic strong shoulder on the absorption. Because of the quantum confinement effect the calculated static dielectric constants for all the considered films are considerably lower than those of bulk material. For the Si quantum wells covered by CaF<sub>2</sub> we have shown that the optoelectronic spectrum is affected both by confinement and by hybridization effects. The major outcome in this case is that for Si well dimensions less than 2 nm, interesting transitions appear in the optical region, with oscillator strengths which show a dramatic increase as the slab width decreases. Moreover, here the static dielectric constants for the thin slabs are

also considerably smaller than that for bulk Si. In the case of Si/SiO<sub>2</sub> superlattices we considered both fully passivated interfaces and the presence of an O vacancy at the interface. Here our results showed the key role played both by the quantum confined states and interface states in the experimentally observed visible luminescence in Si/SiO<sub>2</sub> confined systems.

## ACKNOWLEDGMENTS

We would like to acknowledge all the people that have been involved in our efforts, in particular C. Arcangeli, M. Amato, F. Arnaud D'Avitaya, F. Bassani, F. Bechstedt, F. Bernardini, O. Bisi, V. E. Borisenko, M. Bruno, G. Cantale, N. Daldosso, L. Dal Negro, R. Del Sole, A. Fasolino, A. Filonov, M. Gatti, R. Guerra, F. Iori, A. N. Kholod, E. Luppi, M. Luppi, R. Magri, A. Marini, I. Marri, D. Ninno, G. Onida, V. Olevano, M. Palummo, L. Pavesi, O. Pulci, L. Ramos, F. Trani and L. Vervoort. All the calculations have been performed at CINECA-Bologna (we acknowledge the "Iniziativa calcolo parallelo" of CNR-INFM) and CICAIA-Modena advanced computing facilities. Financial support through PRIN2007 and CNR Project Italia-Turchia is also acknowledged.

## REFERENCES

- [1] S. Ossicini, L. Pavesi, F. Priolo, Light Emitting Silicon for Microphotonics, in: Springer Tracts on Modern Physics, vol. 194, Springer-Verlag, Berlin, 2003.
- [2] L. Pavesi, E. Buzaneva, Frontiers of Nano-Optoelectronics Systems, in: NATO Science Series II. Mathematics, Physics and Chemistry, vol. 6, Kluwer Academic Publishers, Dordrecht, 2000.
- [3] L.T. Canham, *Appl. Phys. Lett.* 57 (1990) 1046.
- [4] D. Bensahel, L.T. Canham, S. Ossicini (Eds.), Optical Properties of Low Dimensional Silicon Structures, Kluwer, Dordrecht, Amsterdam, 1993.
- [5] B. Hamilton, *Semicond. Sci. Technol.* 10 (1995) 1187.
- [6] Y. Kanemitsu, *Phys. Rep.* 263 (1995) 1.
- [7] G.S. John, V.A. Singh, *Phys. Rep.* 263 (1995) 93–151.
- [8] L.T. Canham (Ed.), Properties of Porous Silicon, INSPEC: The Institution of Electrical Engineers, London, 1997.
- [9] A.G. Cullis, L.T. Canham, P.D.J. Calcott, *J. Appl. Phys.* 82 (1997) 909.
- [10] O. Bisi, S. Ossicini, L. Pavesi, *Surf. Sci. Reports* 38 (2000) 5.
- [11] Y. Takahashi, T. Furuta, Y. Ono, T. Tsushima, M. Tabe, *Jpn. J. Appl. Phys.* 34 (1995) 950.
- [12] D.J. Lockwood, Z.H. Lu, J.-M. Baribeau, *Phys. Rev. Lett.* 76 (1996) 539.
- [13] S.V. Novikov, J. Sinkkonen, O. Kilpela, S.V. Gastev, *J. Vac. Sci. Technol. B* 15 (1997) 1471.
- [14] Y. Kanemitsu, S. Okamoto, *Phys. Rev. B* 56 (1997) R15561.
- [15] V. Mulloni, R. Chierchia, C. Mazzoleni, G. Pucker, L. Pavesi, P. Bellutti, *Phil. Mag. B* 80 (2000) 705–718.
- [16] B. Gelloz, A. Kojima, N. Koshida, *Appl. Phys. Lett.* 87 (2005) 031107.
- [17] R.J. Baierle, M.J. Caldas, E. Molinari, S. Ossicini, *Solid State Commun.* 102 (1997) 545.
- [18] M.V. Wolkin, J. Jorne, P.M. Fauchet, G. Allan, C. Delerue, *Phys. Rev. Lett.* 82 (1999) 197.
- [19] A. Puzder, A.J. Williamson, J.C. Grossman, G. Galli, *Phys. Rev. Lett.* 88 (2002) 097401.
- [20] M. Luppi, S. Ossicini, *Phys. Rev. B* 71 (2005) 035040.
- [21] M. Luppi, S. Ossicini, *Phys. Stat. Sol. (a)* 197 (2003) 251.

- [22] M. Luppi, S. Ossicini, *J. Appl. Phys.* 94 (2003) 2130.
- [23] I. Vasiliev, J.R. Chelikowsky, R.M. Martin, *Phys. Rev. B* 65 (2002) 121302(R).
- [24] L. Pavesi, L. Dal Negro, C. Mazzoleni, G. Franzò, F. Priolo, *Nature* 408 (2000) 440.
- [25] L. Dal Negro, M. Cazzanelli, L. Pavesi, S. Ossicini, D. Pacifici, G. Franzò, F. Priolo, F. Iacona, *Appl. Phys. Lett.* 82 (2003) 4636.
- [26] J. Ruan, P.M. Fauchet, L. Dal Negro, M. Cazzanelli, L. Pavesi, *Appl. Phys. Lett.* 83 (2003) 5479.
- [27] M. Cazzanelli, D. Kovalev, L. Dal Negro, Z. Gaburro, L. Pavesi, *Phys. Rev. Lett.* 93 (2004) 207042.
- [28] S. Ossicini, C. Arcangeli, O. Bisi, E. Degoli, M. Luppi, R. Magri, L. Dal Negro, L. Pavesi, in: L. Dal Negro, S. Gaponenko, L. Pavesi (Eds.), *Towards the First Silicon Laser*, in: Nato Science Series, vol. 93, Kluwer Academic Publishers, Dordrecht, 2003, p. 271.
- [29] G. Allan, C. Delerue, M. Lannoo, *Phys. Rev. Lett.* 76 (1996) 2961.
- [30] C. Delerue, G. Allan, M. Lannoo, *J. Lum.* 80 (1999) 65.
- [31] C. Delerue, G. Allan, M. Lannoo, *Phys. Rev. B* 64 (2001) 193402.
- [32] M. Fujii, Y. Yamaguchi, Y. Takase, K. Ninomiya, S. Hayashi, *Appl. Phys. Lett.* 87 (2005) 211919.
- [33] M. Fujii, K. Toshikyo, Y. Takase, Y. Yamaguchi, S. Hayashi, *J. Appl. Phys.* 94 (2003) 1990.
- [34] M. Fujii, Y. Yamaguchi, Y. Takase, K. Ninomiya, S. Hayashi, *Appl. Phys. Lett.* 85 (2004) 1158.
- [35] A.M. Morales, C.M. Lieber, *Science* 279 (1998) 208.
- [36] J.D. Holmes, K.P. Johnston, R.C. Doty, B.A. Korgel, *Science* 287 (2000) 1471.
- [37] D.D.D. Ma, C.S. Lee, F.C.K. Au, S.Y. Tong, S.T. Lee, *Science* 299 (2003) 1874.
- [38] M. Kawamura, N. Paul, V. Cherepanov, B. Voigtländer, *Phys. Rev. Lett.* 91 (2003) 096102.
- [39] J.C. She, S.Z. Deng, N.S. Xu, R.H. Yao, J. Chen, *Appl. Phys. Lett.* 88 (2006) 013112.
- [40] Y. Cui, C.M. Lieber, *Science* 291 (2001) 851.
- [41] J. Hahm, C. Lieber, *Nano Lett.* 4 (2004) 51.
- [42] X.T. Zhou, J.Q. Hu, C.P. Li, D.D.D. Ma, C.S. Lee, S.T. Lee, *Chem. Phys. Lett.* 369 (2003) 220.
- [43] Y. Wu, R. Fan, P. Yang, *Nano Lett.* 2 (2002) 83.
- [44] F. Arnaud D'Avitaya, L. Vervoort, S. Ossicini, A. Fasolino, F. Bernardini, *Europhys. Lett.* 31 (1995) 25.
- [45] F. Bassani, L. Vervoort, I. Mihalcescu, J.C. Vial, F. Arnaud D'Avitaya, *J. Appl. Phys.* 79 (1996) 4066.
- [46] F. Bassani, I. Mihalcescu, J.C. Vial, F. Arnaud D'Avitaya, *Appl. Surf. Sci.* 117/118 (1997) 670.
- [47] Y. Takahashi, T. Furuta, Y. Ono, T. Tsushima, M. Tabe, *Jpn. J. Appl. Phys.* 34 (1995) 950.
- [48] D.J. Lockwood, Z.H. Lu, J.-M. Baribeau, *Phys. Rev. Lett.* 76 (1996) 539.
- [49] S.V. Novikov, J. Sinkkonen, O. Kilpela, S.V. Gastev, *J. Vac. Sci. Technol. B* 15 (1997) 1471.
- [50] K.S. Min, K.V. Shcheglov, C.M. Yang, H.A. Atwater, M.L. Brongersma, A. Polman, *Appl. Phys. Lett.* 69 (1996) 2033.
- [51] Y. Kanemitsu, S. Okamoto, *Phys. Rev. B* 56 (1997) R15561.
- [52] H.G. Yoo, P.M. Fauchet, *Phys. Rev. B* 77 (2008) 115355.
- [53] O. Pulci, M. Marsili, E. Luppi, C. Hogan, V. Garbuio, F. Sottile, R. Magri, R. Del Sole, *Phys. Stat. Sol. (b)* 242 (13) (2005) 2737–2750.
- [54] M. Palummo, M. Bruno, O. Pulci, E. Luppi, E. Degoli, S. Ossicini, R. Del Sole, *Surf. Sci.* 601 (13) (2007) 2696.
- [55] P. Hohenberg, W. Kohn, *Phys. Rev. B* 136 (1964) 864.
- [56] W. Kohn, L.J. Sham, *Phys. Rev. A* 140 (1965) 1113.
- [57] D.M. Ceperley, B.J. Alder, *Phys. Rev. Lett.* 45 (1980) 566; J.P. Perdew, A. Zunger, *Phys. Rev. B* 23 (1981) 5048.
- [58] F. Bassani, G. Pastori Parravicini, *Electronic States and Optical Transitions in Solids*, Pergamon Press, New York, 1975.
- [59] M. Alouani, L. Brey, N.E. Christensen, *Phys. Rev. B* 37 (1988) 1167.
- [60] L. Fetter, J.D. Walecka, *Quantum Theory of Many Body Systems*, McGraw-Hill, New York, 1981.

- [61] L. Hedin, Phys. Rev. A 139 (1965) 796;  
R.D. Mattuck, *A Guide to Feynman Diagrams in the Many Body Problem*, McGraw-Hill, New York, 1976.
- [62] L. Hedin, B.J. Lundquist, in: H. Ehrenreich, F. Seitz, D. Turnbull (Eds.), *Solid State Phys.*, vol. 23, Academic Press, New York, 1969, p. 1.
- [63] F. Aryasetiawan, O. Gunnarsson, Rep. Prog. Phys. 61 (1998) 237;  
W.G. Aulbur Johsson, J.W. Wilkins, Solid State Phys. 54 (2000) 1–218.
- [64] S.L. Adler, Phys. Rev. 126 (1962) 413;  
N. Wiser, Phys. Rev. 129 (1963) 62.
- [65] T. Takagahara, K. Takeda, Phys. Rev. B 46 (1992) 15578.
- [66] J. Lockwood, Solid State Commun. 92 (1994) 101.
- [67] First-principles computation of material properties: The ABINIT software project (URL <http://www.abinit.org/>);  
X. Gonze, J.-M. Beuken, R. Caracas, F. Detraux, M. Fuchs, G.-M. Rignanese, L. Sindic, M. Zerah, Verstraete Jollet, G. Torrent, F. Roy, M. Mikami, A. Ghosez, M. Raty, Ph. Allan, Comp. Mat. Science 25 (2002) 478.
- [68] E. Degoli, G. Cantele, E. Luppi, R. Magri, D. Ninno, O. Bisi, S. Ossicini, Phys. Rev. B 69 (2004) 155411.
- [69] J.P. Wicoxon, G.A. Samara, P.N. Provencio, Phys. Rev. B 60 (1999) 2704.
- [70] G. Belomoin, J. Therrien, M.H. Nayfeh, Appl. Phys. Lett. 77 (2000) 779.
- [71] C. Delerue, M. Lannoo, G. Allan, Phys. Rev. Lett. 84 (2000) 2457.
- [72] J.C. Grossman, M. Rohlfing, L. Mitas, S.G. Louie, M.L. Cohen, Phys. Rev. Lett. 86 (2001) 472.
- [73] G. Onida, W. Andreoni, Chem. Phys. Lett. 243 (1995) 183.
- [74] The absorption gap value for the Si<sub>29</sub>H<sub>36</sub> cluster cited by Franceschetti is 4.3 eV but it is estimated by adding the local-spin density band-gap error of bulk Si (0.7 eV)..
- [75] A. Puzder, A.J. Williamson, J.C. Grossman, G. Galli, J. Am. Chem. Soc. 125 (2003) 2786.
- [76] A. Franceschetti, S.T. Pantelides, Phys. Rev. B 68 (2003) 033313.
- [77] U. Itoh, Y. Toyoshima, H. Onuki, N. Washida, T. Ibuki, J. Chem. Phys. 85 (1986) 4867.
- [78] M. Rohlfing, S.G. Louie, Phys. Rev. Lett. 80 (1998) 3320.
- [79] M. Hirao, in: L. Brus, M. Hirose, R.W. Collins, F. Koch, C.C. Tsai (Eds.), *Microcristalline and Nanocrystalline Semiconductors*, in: Mater. Res. Soc. Symp. Proc., vol. 358, Material Research Society, Pittsburgh, 1995.
- [80] O. Lehtonen, D. Sundholm, Phys. Rev. B 72 (2005) 085424.
- [81] G. Belomoin, J. Therrien, A. Smith, S. Rao, R. Twesten, S. Chaieb, M.H. Nayfeh, L. Wagner, L. Mitas, Appl. Phys. Lett. 80 (2002) 841.
- [82] Y. Kanemitsu, S. Okamoto, Phys. Rev. B 58 (1998) 9652.
- [83] E. Luppi, E. Degoli, G. Cantele, S. Ossicini, R. Magri, D. Ninno, O. Bisi, O. Pulci, G. Onida, M. Gatti, A. Incze, R. Del Sole, Opt. Mater. 27 (2005) 1008.
- [84] M. Bockstedte, A. Kley, J. Neugebauer, M. Scheffler, Comput. Phys. Commun. 107 (1997) 187.
- [85] Cambridge Serial Total Energy Package, Version 4.2.1, 1 October 2000.
- [86] V. Milman, B. Winkler, J.A. White, C.J. Pickard, M.C. Payne, E.V. Akhmatskaya, R.H. Nobes, Int. J. Quantum Chem. 77 (2000) 895.
- [87] Cerius<sup>2</sup> Users Guide and Materials Studio 2.1.5 Users Guide for CASTEP, MSI and Accelrys Inc., 2000–2002.
- [88] L. Kleinman, D.M. Bylander, Phys. Rev. Lett. 48 (1982) 1425.
- [89] N. Troullier, J.L. Martins, Phys. Rev. B 43 (1991) 1993.
- [90] D. Vanderbilt, Phys. Rev. B 41 (1990) R7892.
- [91] R. Sammynaiken, S.J. Naftel, T.K. Shamb, K.W. Cheah, B. Averboukh, R. Huber, Y.R. Shen, G.G. Qin, Z.C. Ma, W.H. Zhong, J. Appl. Phys. 92 (2002) 3000.
- [92] E. Luppi, F. Iori, R. Magri, O. Pulci, R. Del Sole, S. Ossicini, E. Degoli, V. Olevano, Phys. Rev. B 75 (2007) 033303.
- [93] M. Gatti, G. Onida, Phys. Rev. B 72 (2005) 045442.

- [94] The Si<sub>10</sub>H<sub>14</sub>->O cluster we considered here corresponds to the Si<sub>10</sub>H<sub>14</sub>O-sym of [93], where O make a bridge between “second neighbors” Si atoms. We have obtained similar results have for the Si<sub>10</sub>H<sub>14</sub>O-asym case, where O is in between two “first neighbors” Si atoms..
- [95] S. Baroni, A. Dal Corso, S. de Gironcoli, P. Giannozzi, C. Cavazzoni, G. Ballabio, S. Scandolo, G. Chiarotti, P. Focher, A. Pasquarello, K. Laasonen, A. Trave, R. Car, N. Marzari, A. Kokalj, The DFT calculations for oxidized clusters have been performed using the ESPRESSO package. <http://www.pwscf.org/>.
- [96] Z. Ma, X. Liao, G. Kong, J. Chu, Appl. Phys. Lett. 75 (1999) 1857.
- [97] H. Kageshima, K. Shiraishi, in: M. Scheffler, R. Zimmermann (Eds.), Proc. 23rd Int. Conf. Phys. Semicon., World Scientific, Singapore, 1996, p. 903.
- [98] N. Daldosso, M. Luppi, S. Ossicini, E. Degoli, R. Magri, G. Dalba, P. Fornasini, R. Grisenti, F. Rocca, L. Pavesi, S. Boninelli, F. Priolo, C. Spinella, F. Iacona, Phys. Rev. B 68 (2003) 085327.
- [99] T. Takagahara, K. Takeda, Phys. Rev. B 46 (1992) 15578.
- [100] E. Lioudakis, A. Othonos, G.C. Hadjisavvas, P.C. Kelires, A.G. Nassiopoulou, Physica E 38 (2007) 128.
- [101] G. Hadjisavvas, P.C. Kelires, Physica E 38 (2007) 99.
- [102] The numerical values differences with respect to the previously published paper, [20] are due to the different computational code used.
- [103] G. Cantele, E. Degoli, E. Luppi, R. Magri, D. Ninno, G. Iadonisi, S. Ossicini, Phys. Rev. B 72 (2005) 113303.
- [104] S. Ossicini, E. Degoli, F. Iori, E. Luppi, R. Magri, G. Cantele, F. Trani, D. Ninno, Appl. Phys. Lett. 87 (2005) 173120.
- [105] S. Ossicini, F. Iori, E. Degoli, E. Luppi, R. Magri, R. Poli, G. Cantele, F. Trani, D. Ninno, J. Select. Topics in Quantum Electr. 12 (2006) 1585.
- [106] F. Iori, E. Degoli, E. Luppi, R. Magri, I. Marri, G. Cantele, D. Ninno, F. Trani, S. Ossicini, J. Lumin. 121 (2006) 335.
- [107] F. Iori, S. Ossicini, E. Degoli, E. Luppi, R. Poli, R. Magri, G. Cantele, F. Trani, D. Ninno, Phys. Stat. Sol. (a) 204 (2007) 1312.
- [108] R. Magri, E. Degoli, F. Iori, E. Luppi, O. Pulci, S. Ossicini, G. Cantele, F. Trani, D. Ninno, J. Comp. Meth. Sci. Eng. 7 (2007) 219.
- [109] F. Iori, E. Degoli, R. Magri, I. Marri, G. Cantele, D. Ninno, F. Trani, O. Pulci, S. Ossicini, Phys. Rev. B 76 (2007) 085302.
- [110] S. Ossicini, E. Degoli, F. Iori, O. Pulci, G. Cantele, R. Magri, O. Bisi, F. Trani, D. Ninno, Surf. Sci. 601 (2007) 2724.
- [111] S. Ossicini, O. Bisi, E. Degoli, I. Marri, F. Iori, E. Luppi, R. Magri, R. Poli, G. Cantele, D. Ninno, F. Trani, M. Marsili, O. Pulci, M. Gatti, K. Gaal-Nagy, A. Incze, G. Onida, V. Olevano, J. Nanosci. Nanotechnol. 8 (2008) 479.
- [112] D. Vanderbilt, Phys. Rev. B 41 (1990) R7892.
- [113] L.E. Ramos, E. Degoli, G. Cantele, S. Ossicini, D. Ninno, J. Furthmüller, F. Bechstedt, J. Phys.: Cond. Matt. 19 (2007) 466211.
- [114] L.C. Ciacci, M.C. Payne, Phys. Rev. Lett. 95 (2005) 196101.
- [115] E. Garrone, F. Geobaldo, P. Rivolo, G. Amato, L. Boarino, M. Chiesa, E. Giannello, R. Gobetto, P. Ugliengo, A. Vitale, Adv. Mater. 17 (2005) 528.
- [116] V. Olevano, Exc Code, <http://www.bethe-salpeter.org>.
- [117] D.V. Melnikov, J.R. Chelikowsky, Phys. Rev. Lett. 92 (2004) 046802.
- [118] P.Y. Yu, M. Cardona, Fundamentals of Semiconductors, Springer, Berlin, 2001.
- [119] C.D. Spataru, S. Ismail-Beigi, L.X. Benedict, S.G. Louie, Phys. Rev. Lett. 92 (2004) 077402.
- [120] E. Chang, G. Bussi, A. Ruini, E. Molinari, Phys. Rev. Lett. 92 (2004) 196401.
- [121] M. Bruno, M. Palummo, A. Marini, R. Del Sole, V. Olevano, A.N. Kholod, S. Ossicini, Phys. Rev. B 72 (2005) 153310.
- [122] M. Bruno, M. Palummo, A. Marini, R. Del Sole, S. Ossicini, Phys. Rev. Lett. 98 (2007) 036807.

- [123] F. Trani, D. Ninno, G. Cantele, G. Iadonisi, K. Hameeuw, E. Degoli, S. Ossicini, Phys. Rev. B 73 (2006) 245430.
- [124] D. Ninno, F. Trani, G. Cantele, G. Iadonisi, K.J. Hameeuw, E. Degoli, S. Ossicini, Europhys. Lett. 74 (2006) 519.
- [125] C. Delerue, M. Lannoo, G. Allan, Phys. Rev. B 68 (2003) 115411.
- [126] R. Resta, Phys. Rev. B 16 (1977) 2717.
- [127] S. Öğüt, R. Burdick, Y. Saad, J.R. Chelikowsky, Phys. Rev. Lett. 90 (2003) 127401.
- [128] Y. Cui, Z. Zhong, D. Wang, W.U. Wang, C.M. Lieber, Nanoletters 3 (2003) 149.
- [129] Y. Cui, C.M. Lieber, Science 291 (2001) 851.
- [130] Y. Huang, X. Duan, Y. Cui, C.M. Lieber, Nanoletters 2 (2001) 101.
- [131] X. Duan, Y. Huang, Y. Cui, J. Wang, C.M. Lieber, Nature 409 (2001) 066.
- [132] X. Duan, Y. Huang, C.M. Lieber, Nano Letters 2 (2002) 487.
- [133] Y. Cui, L.J. Lauhon, M.S. Gudiksen, J. Wang, C.M. Lieber, Appl. Phys. Lett. 78 (2001) 02214.
- [134] Y. Cui, Q. Wei, H. Park, C.M. Lieber, Science 293 (2001) 1289.
- [135] M.H. Huang, S. Mao, H. Feick, H. Yan, Y. Wu, H. Kind, E. Weber, P. Russo, P. Yang, Science 292 (2001) 1897.
- [136] X. Duan, Y. Huang, R. Agarwal, C.M. Lieber, Nano Lett. 421 (2003) 241.
- [137] L.J. Lauhon, M.S. Gudiksen, D. Wang, C.M. Lieber, Nature 420 (2002) 57.
- [138] Y. Wu, Y. Cui, L. Huynh, C.J. Barrelet, D.C. Bell, C.M. Lieber, Nano Lett. 4 (2004) 433.
- [139] M. Menon, D. Srivastava, I. Ponomareva, L.A. Chernozatonskii, Phys. Rev. B 70 (2004) 125313.
- [140] A.M. Morales, C.M. Lieber, Science 279 (1998) 208.
- [141] J.D. Holmes, K.P. Johnston, R.C. Doty, B.A. Korgel, Science 287 (2000) 1471.
- [142] X. Duan, J. Wang, C.M. Lieber, Appl. Phys. Lett. 76 (2000) 01116.
- [143] D. Katz, T. Wizansky, O. Millo, E. Rothenberg, T. Mokari, U. Banin, Phys. Rev. Lett. 89 (2002) 86801.
- [144] Y.F. Zhang, Y.H. Tang, N. Wang, C.S. Lee, I. Bello, S.T. Lee, Phys. Rev. B 61 (2000) 4518.
- [145] D. Wang, Q. Wang, A. Javey, R. Tu, H. Dai, Appl. Phys. Lett. 83 (2003) 2432.
- [146] A. Alguno, N. Usami, T. Ujihara, K. Fujiwara, G. Sazaki, K. Nakajima, Appl. Phys. Lett. 83 (2003) 1258.
- [147] A.K. Singh, V. Kumar, Y. Kawazoe, Phys. Rev. B 69 (2004) 233406.
- [148] M.P. Halsall, H. Omi, T. Ogino, Appl. Phys. Lett. 81 (2002) 2448.
- [149] X. Zhao, C.M. Wei, L. Yang, M.Y. Chou, Phys. Rev. Lett. 92 (2004) 236805.
- [150] M. Bruno, M. Palummo, S. Ossicini, R. Del Sole, Surf. Sci. 601 (2007) 2707.
- [151] M.S. Hybertsen, M. Needels, Phys. Rev. B 48 (1993) 4608.
- [152] A.J. Read, R.J. Needs, K.J. Nash, L.T. Canham, P.D.J. Calcott, A. Qteish, Phys. Rev. Lett. 69 (1992) 01232.
- [153] F. Buda, J. Kohano, M. Parrinello, Phys. Rev. Lett. 69 (1992) 01272.
- [154] A.N. Kholod, V.L. Shaposhnikov, N. Sobolev, V.E. Borisenko, F.A. D'Avitaya, S. Ossicini, Phys. Rev. B 70 (2004) 035317.
- [155] S. Ossicini, C.M. Bertoni, M. Biagini, A. Lugli, G. Roma, O. Bisi, Thin Solid Films 297 (1997) 154.
- [156] S. Ossicini, Phys. Stat. Sol. (a) 170 (1998) 377.
- [157] R. Kagimura, R.W. Nunes, H. Chacham, Phys. Rev. Lett. 95 (2005) 115502.
- [158] R. Rurali, N. Lorente, Phys. Rev. Lett. 94 (2005) 026805.
- [159] T. Ogawa, T. Takagahara, Phys. Rev. B 44 (1991) 8138.
- [160] Y. Zheng, C. Rivas, T. Lake, K. Alam, T.B. Boykin, G. Klimeck, IEEE Trans. Electr. Dev. 52 (2005) 1097.
- [161] Y.M. Niquet, A. Lherbier, N.H. Quang, M.V. Fernandez-Serra, X. Blase, C. Delerue, Phys. Rev. B 73 (2006) 165319.
- [162] Q. Zhang, S.C. Bayliss, J. Appl. Phys. 79 (1996) 1351.
- [163] H.C. Weisssker, J. Furthmuller, F. Bechstedt, Phys. Rev. B 69 (2004) 115310.
- [164] M.V. Fernández-Serra, Ch. Adessi, X. Blase, Nano Lett. 6 (2006) 2674.
- [165] H. Peelaers, B. Partoens, F.M. Peeters, Nano Lett. 6 (2006) 2781.
- [166] A.N. Kholod, S. Ossicini, V.N. Borisenko, F. Arnaud d'Avitaya, Surf. Sci. 527 (2003) 30.

- [167] E. Degoli, S. Ossicini, Phys. Rev. B 57 (1998) 14776.
- [168] E. Degoli, S. Ossicini, Surf. Sci. 470 (2000) 32.
- [169] P. Blaha, K. Schwarz, J. Luitz, WIEN97, Vienna University of Technology, Vienna, 1997 (improved and updated Unix version of the original copyrighted WIEN-code, which was published by P. Blaha, K. Schwarz, P. Sorantin, S.B. Trickey, in Comput. Phys. Commun. 59, 399 (1990)).
- [170] A.N. Kholod, A. Saúl, J. Fuhr, V.E. Borisenko, F. Arnaud d'Avitaya, Phys. Rev. B 62 (2000) 12949.
- [171] M.L. Cohen, J.R. Chelikowsky, Electronic Structure and Optical Properties of Semiconductors, Springer-Verlag, Berlin, 1989.
- [172] P.N. Saeta, A.C. Gallagher, Phys. Rev. B 55 (1997) 4563.
- [173] S. Ossicini, A. Fasolino, F. Bernardini, Phys. Rev. Lett. 72 (1994) 1044.
- [174] R.M. Tromp, M.C. Reuter, Phys. Rev. Lett. 61 (1988) 1756.
- [175] J. Zegenhagen, J.R. Patel, Phys. Rev. B 41 (1990) 5315.
- [176] M. Ben-Chorin, B. Averboukh, D. Kovalev, G. Polisski, F. Koch, Phys. Rev. Lett. 77 (1996) 763.
- [177] L. Wang Wang, A. Zunger, Phys. Rev. Lett. 73 (1994) 1039.
- [178] N. Koshida, H. Koyama, Y. Suda, Y. Yamamoto, M. Araki, T. Saito, K. Sato, N. Sata, S. Shin, Appl. Phys. Lett. 63 (1993) 2774.
- [179] L. Pavesi, R. Guardini, C. Mazzoleni, Solid State Commun. 97 (1996) 1051.
- [180] H. Kageshima, K. Shiraishi, in: M. Scheffler, R. Zimmermann (Eds.), Proc. 23rd Int. Conf. Phys. Semicon., World Scientific, Singapore, 1996, p. 903.
- [181] H. Kageshima, K. Shiraishi, Surf. Sci. 380 (1997) 61–65.
- [182] H. Kageshima, K. Shiraishi, Surf. Sci. 407 (1998) 133–139.
- [183] H. Kageshima, K. Shiraishi, Phys. Rev. Lett. 81 (1998) 5936.
- [184] H. Kageshima, K. Shiraishi, Surf. Sci. 438 (1999) 102–106.
- [185] T. Uchiyama, M. Tsukada, Phys. Rev. B 53 (1996) 7917.
- [186] Y. Kanemitsu, T. Ogawa, K. Shiraishi, K. Takeda, Phys. Rev. B 48 (1993) 4883.
- [187] Y. Kanemitsu, Phys. Rep. 263 (1995) 1.
- [188] I. Batra, in: S.T. Pantelides (Ed.), The Physics of SiO<sub>2</sub> and its Interfaces, vol. 333, Pergamon Press, NY, 1978.
- [189] N. Tit, M.W.C. Dharma-Wardana, Sol. State Comm. 106 (1998) 121.
- [190] S.D. Kosowsky, P.S. Pershan, K.S. Kirsch, J. Bevk, M.L. Green, D. Brasen, L.C. Feldman, P.K. Roy, Appl. Phys. Lett. 70 (1997) 3119.
- [191] A. Pasquarello, M.S. Hybertsen, R. Car, Appl. Phys. Lett. 68 (1996) 625.
- [192] C.G. Van de Walle, J.E. Northrup, Phys. Rev. Lett. 70 (1993) 1156.